

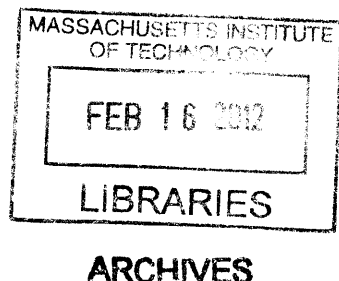
Optimal Planning and Control for Hazard Avoidance of Front-Wheel  
Steered Ground Vehicles

by

Steven C. Peters

Bachelor of Science, Mechanical Engineering  
University of California, Davis 2004

Master of Science, Mechanical Engineering  
Massachusetts Institute of Technology, 2006



ARCHIVES

Submitted to the Department of Mechanical Engineering  
in partial fulfillment of the requirements for the degree of  
Doctor of Philosophy in Mechanical Engineering

at the

Massachusetts Institute of Technology

February 2012

© 2012 Massachusetts Institute of Technology  
All rights reserved

Signature of Author.....

Department of Mechanical Engineering  
January 20, 2012

Certified by.....

Karl Iagnemma  
Principal Research Scientist  
Thesis Supervisor

Accepted by.....

Professor David Hardt  
Chairman, Committee on Graduate Studies

Optimal Planning and Control for Hazard Avoidance of Front-Steered Ground Vehicles

by

Steven C. Peters

Submitted to the Department of Mechanical Engineering  
On January 20, 2012, in Partial Fulfillment of the  
Requirements for the Degree of  
Master of Science in Mechanical Engineering

**ABSTRACT**

Hazard avoidance is an important capability for safe operation of robotic vehicles at high speed. It is also an important consideration for passenger vehicle safety, as thousands are killed each year in passenger vehicle accidents caused by driver error. Even when hazard locations are known, high-speed hazard avoidance presents challenges in real-time motion planning and control of nonlinear and potentially unstable vehicle dynamics.

This thesis presents methods for planning and control of optimal hazard avoidance maneuvers for a bicycle model with front-wheel steering and wheel slip. The planning problem is posed as an optimization problem in which constrained dynamic quantities, such as friction circle utilization, are minimized, while ensuring a minimum clearance from hazards. These optimal trajectories can be computed numerically, though real-time computation requires simple models and constraints.

To simplify the computation of optimal avoidance trajectories, analytical solutions to the optimal planning problem are presented for a point mass subject to an acceleration magnitude constraint, which is analogous to a tire friction circle constraint. The optimal point mass solutions are extended to a nonlinear bicycle model by defining a flatness-based trajectory tracking controller using tire force control. This controller decouples the bicycle dynamics into a point mass at the front center of oscillation with an additional degree of freedom related to the vehicle yaw dynamics. Structure is identified in the yaw dynamics and is exploited to characterize stability limits. Simulation results verify the stability properties of the yaw dynamics.

These results were applied to a semi-autonomous driver assistance system and demonstrated experimentally on a full-sized passenger vehicle. Efficient computation of point mass avoidance maneuvers was used as a cost-to-go for real-time numerical optimization of trajectories for a bicycle model. The experimental system switches control authority between the driver and an automatic avoidance controller so that the driver retains control authority in benign situations, and the automatic controller avoids hazards automatically in hazardous situations.

Thesis Supervisor: Karl Iagnemma, Principal Research Scientist

## **ACKNOWLEDGEMENTS**

---

I would like to thank my advisor Karl Iagnemma and professors Steve Dubowsky, Emilio Frazzoli, and Jon How for their guidance and feedback as members of my thesis committee. Special thanks to Tom Pilutti, Eric Tseng, Mitch McConnell, Roger Trombley, Matt Rupp, and the other engineers at Ford who helped us to conduct experiments in Dearborn. It's been great working with Sterling and all the other members of the Robotic Mobility Group and FSRL over my time here at MIT. I would also like to thank my family and friends for supporting me in my thesis adventure. I am now PhSteve.

This research was supported by Ford Motor Company and the US Army Research Office under award W911NF-11-1-0046.

## **TABLE OF CONTENTS**

---

Abstract.....	1
Acknowledgements.....	2
Table of Contents.....	3
Chapter 1: Introduction.....	5
1.1    Importance of high-speed hazard avoidance.....	5
1.2    Brief review of sensing for hazard avoidance.....	6
1.3    Review of motion planning for hazard avoidance.....	8
1.3.1    Model-agnostic planning methods.....	8
1.3.2    Model-specific planning methods.....	10
1.3.3    Motion planning summary.....	13
1.4    Review of control for hazard avoidance.....	13
1.4.1    Tire modeling for vehicle control .....	14
1.4.2    Differential flatness in ground vehicle control .....	17
1.4.3    Vehicle control summary .....	18
1.5    Contributions of this thesis .....	19
Chapter 2: Optimal Avoidance Problem.....	21
2.1    General form of optimal avoidance planning problem.....	21
2.2    Nonlinear bicycle model .....	22
2.3    Example optimal avoidance trajectory for nonlinear bicycle .....	29
2.4    Conclusion .....	32
Chapter 3: Point Mass Optimal Avoidance .....	33
3.1    Introduction.....	33
3.2    Point mass with acceleration circle constraint.....	33
3.3    Geometric avoidance maneuvers for a single hazard .....	34
3.4    Optimal avoidance maneuvers for a single hazard .....	38
3.4.1    Optimal non-passing maneuver .....	39
3.4.2    Optimal passing maneuver.....	45
3.4.3    Discussion .....	53
3.5 Conclusions.....	55
Chapter 4: Control of Nonlinear Bicycle .....	56
4.1    Flatness of nonlinear bicycle model .....	56
4.2    Analysis of Yaw Dynamics .....	59
4.2.1    Structure of yaw dynamics.....	60
4.2.2    Stability of unforced yaw dynamics .....	65
4.2.3    Stability of yaw dynamics during turning .....	75
4.2.4    Stability of yaw dynamics during time-varying maneuvers .....	98
4.2.5    Summary .....	101
4.3    Discussion .....	101
4.4    Conclusion .....	103
Chapter 5: Vehicle Control for Safety Application .....	104
5.1    Introduction.....	104
5.2    Semi-autonomous system description.....	105

5.2.1	Sensing and hazard geometry assumptions and definition .....	105
5.2.2	Optimal trajectory planning and control.....	106
5.2.3	MPC Implementation details .....	108
5.2.4	Cost-based control authority switching .....	110
5.3	Simulation and Experimental Results.....	111
5.3.1	Experimental setup.....	111
5.3.2	Stopping maneuver .....	112
5.3.3	Passing turn.....	115
5.3.4	Non-passing turn.....	118
5.4	Discussion .....	119
5.5	Conclusion .....	120
<b>Chapter 6:</b>	<b>Conclusions .....</b>	<b>121</b>
6.1	Summary .....	121
6.2	Future work.....	122
<b>References.....</b>		<b>124</b>
<b>Appendix A:</b>	<b>Cost-to-go for Nonlinear MPC.....</b>	<b>129</b>
A.1	Straight-line stopping.....	129
A.2	Constant radius non-passing turn.....	131
A.3	Constant radius passing turn .....	133

# 1

## **CHAPTER 1: INTRODUCTION**

### ***1.1 Importance of high-speed hazard avoidance***

Autonomous navigation of robotic vehicles at high speeds has received substantial research attention in recent years, as highlighted by the DARPA Grand Challenge and Urban Challenge competitions [14, 15]. Applications of high speed robotic vehicles include exploration, military reconnaissance, and material transport. In these scenarios, increasing vehicle speed and maneuverability may increase the likelihood of avoiding hostile situations and improve task efficiency. The danger of collisions with hazards is increased at high speed, however, since collision severity increases with vehicle speed.

Hazard avoidance capability can be incorporated into robot vehicle navigation systems through the integration of appropriate sensing, motion planning, and control systems. Sensing of the environment is necessary to identify the position and motion characteristics of hazards as well as properties of the driving surface. With this information, a motion plan can be constructed that avoids hazards and is feasible for the vehicle dynamics for the given surface conditions. The motion plan should be implemented by a controller that has guarantees on its trajectory tracking capability to ensure that the motion plan is followed safely.

Motion planning and control for high-speed hazard avoidance is challenging for several reasons. The first challenge is caused by constraints on trajectory feasibility arising from the vehicle dynamics and physical limits such as actuator or friction force constraints. These constraints increase the difficulty of the motion planning task. Another challenge is posed by the presence of presence of unstable equilibrium points in the vehicle yaw dynamics depending on the vehicle speed, steering angle, and tire properties [53]. Motion planning and control must be designed to avoid these regions of instability in the dynamics. Finally, algorithm computation time must be short at high speed to allow a timely response to changes in the environment.

The development of hazard avoidance systems for robotic vehicles has distinct applications to passenger vehicles. While passenger vehicle safety has improved over the past 40 years thanks to developments such as seat belts, air bags, optimized crush zones, and stability control systems, more than 30,000 people are killed and millions injured in motor vehicle accidents in the United States each year [24, 23, 51]. It has been found that driver error is a significant factor in accident causation, as the primary cause of 60% of motor vehicle accidents and a contributing factor in 95% of accidents [20]. Similar planning and control methods used for hazard avoidance in robotic vehicles may be incorporated into driver warning or driver assistance systems to mitigate the impact of driver error.

The following sections contain a review of previous work in sensing, motion planning, and vehicle control for high-speed hazard avoidance.

## **1.2 Brief review of sensing for hazard avoidance**

A critical task for hazard avoidance systems is identification of the location and motion of hazards in the environment. This task requires identifying the shape or bounding box of a hazard as well as tracking its position and velocity given by  $X_i$ ,  $Y_i$ ,  $\dot{X}_i$ , and  $\dot{Y}_i$  as shown in the left subfigure of Fig. 1.1. A sample of the state of the art in perception and sensing at low speed (under 15 m/s) can arguably be seen in the robot cars that competed in the DARPA Grand Challenges. These robots utilized cameras, RADAR, and LIDAR to identify other cars and hazards in the environment [14, 15]. A photograph of the MIT vehicle with its sensors is given in the right subfigure of Fig. 1.1. While there were a limited number of minor collisions in the most recent competition, the successful avoidance of collisions throughout the majority of the competition indicates that hazard sensing systems have reached a mature state for vehicle applications [25].

Hazard sensing has been demonstrated at speeds above 15 m/s, notably in commercially available adaptive cruise control systems. These systems utilize RADAR to measure the relative distance and speed of other vehicles to control following distance [2]. The RADAR sensors in these systems have longer range for high-speed use, though they only look for a hazards directly in front of the vehicle.

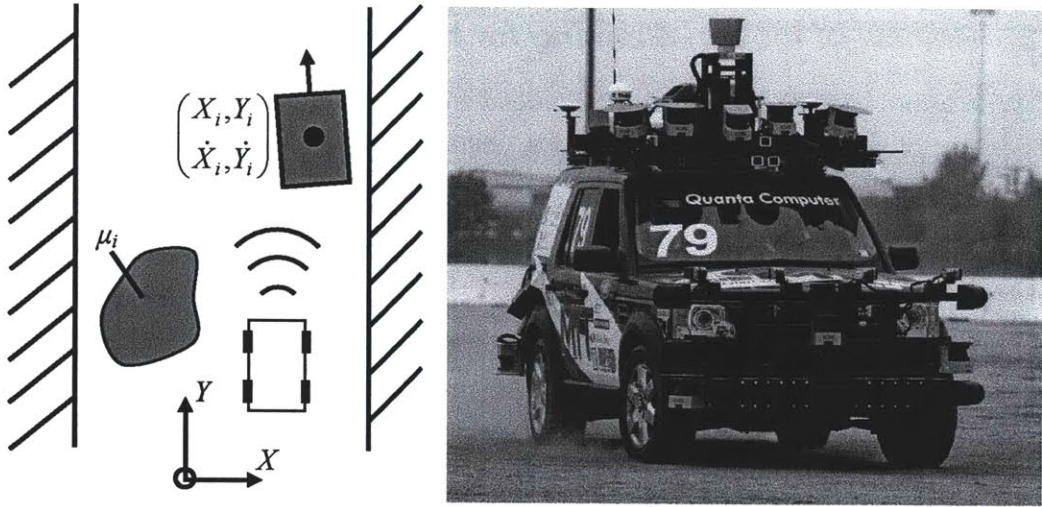


Fig. 1.1: An illustration of the quantities to be identified by hazard sensing systems is given in the left subfigure, and a photograph of Talos, the MIT robot vehicle from the DARPA Urban Challenge is shown in the right subfigure. Talos is equipped with cameras, laser scanners, and RADAR sensors (image by Jason Dorfman of MIT/CSAIL).

Another important task for hazard avoidance systems is the identification of surface friction and traction properties. These surface properties impact the operating envelope of the vehicle and the range of feasible avoidance maneuvers. These properties can be estimated directly using on-board sensors using a variety of methods [30, 77]. Recent research has indicated that these on-board measurements can be combined with measurements of the appearance of the surface and used to estimate upcoming surface properties [31, 11].

As described above, there has been significant research effort expended towards sensing and perception for robotic vehicles, including identifying hazard locations and surface conditions. This remains an active area of research, but it is not the focus of this thesis. As such, it is assumed that a perfect sensing and perception system is available that provides the following:

- Geometric description of drivable surface regions
- Shape/bounding box and location of hazards
- Surface friction coefficient on different surface patches

The duration of this thesis considers the problem of motion planning and control with perfect sensing. The effect of imperfect sensing will be considered in future work.

### **1.3 Review of motion planning for hazard avoidance**

With information about hazard location and surface conditions given by the sensing system, a motion planner computes a feasible hazard-free trajectory through the environment to a desired endpoint. In addition to the basic geometric planning problem (known as the Piano Mover's Problem [58]), the motion planner faces challenges of dynamic trajectory feasibility and computational complexity and, if desired, optimality. Examples of optimality criteria include path length, travel time, clearance from obstacles, and fuel consumption.

Two categories of planning methods are discussed in this section: model-agnostic methods and model-specific methods. Model-agnostic planning methods are general methods suitable for many types of vehicle models, while model-specific planning methods are designed for a specific vehicle model. Though more narrow in scope, model-specific methods may exploit knowledge of the vehicle model to simplify the planning task.

#### **1.3.1 Model-agnostic planning methods**

The simplest form of model-agnostic planning is to solve the geometric Piano Mover's Problem, assuming that all continuous paths are feasible. A common approach to the geometric planning problem is to represent the free space in the environment with a graph and use a graph search algorithm to compute a motion plan. The cellular decomposition method partitions environmental free space into cells and creates a graph based on cell connectivity [44]. The roadmap method chooses a series of points in the environment and defines a graph based on lines or paths connecting these points [44]. For example, a visibility graph is a roadmap created from the corner nodes of obstacles and can be used to find minimum distance piecewise linear paths using graph search algorithms such as Dijkstra's algorithm or A\* [44, 43]. Another type of roadmap is the Voronoi decomposition, which generates path of maximum clearance from obstacles [69]. Probabilistic methods can also be used to generate roadmaps, such as randomly exploring randomized trees (RRT), which generate piecewise-linear collision-free paths with probabilistic completeness guarantees and reduced computational overhead [44]. Though the RRT does not have any optimality guarantees, a recent variation known as RRT\* was

developed that adds an asymptotic optimality guarantee without significantly changing the computational requirements [37]. A disadvantage of geometric planning methods is that the planned paths are not guaranteed to be dynamically feasible.

Another approach to model-agnostic motion planning is the use of potential field methods, which have long been used by defining an artificial potential field with a minimum value at the desired end position and searching for a path to the minimum using methods such as gradient descent [38, 68]. Assigning large potential values to obstacles or untraversable regions of the environment serves to repulse the motion plan from such regions. The major challenge for this method is ensuring that no local minima of the potential field prevent travel to the desired position. Navigation functions can be constructed that have no local minima [60], though they are difficult to construct and modify in real-time.

To ensure dynamic feasibility of planned trajectories, kinodynamic planning methods discretize and search over the space of feasible inputs or feasible trajectories rather than searching over the environmental free space. These methods use a simulated vehicle model to determine whether the resulting trajectories successfully avoid hazards. For example, the RRT method can utilize a randomization of input commands to a vehicle model to generate dynamically feasible trajectories [45] or by randomly selecting from a library of maneuver primitives with corresponding feedback control laws [27]. Another approach uses a reachability analysis to identify the set of states for which dynamically feasible avoidance trajectories do not exist, termed Inevitable Collision States [26]. The analysis was combined with an RRT motion planner to identify feasible trajectories. These methods can also benefit from the asymptotic optimality guarantee arising from the RRT\* method [37]. It should be noted that the computational complexity of these methods scales with the complexity of the simulated vehicle model.

Motion planning via discretization and search over inputs to a vehicle model can also be accomplished with numerical trajectory optimization. While there are numerous approaches to numerical trajectory optimization [9], the most relevant methods are computationally efficient enough to be used for real-time motion planning. Receding-horizon optimal control, for example can generate dynamically feasible optimal avoidance trajectories for linear or nonlinear vehicle models by repeatedly solving a

numerical optimization problem. Minimum-time collision-free trajectories were found for an aerial vehicle with turning rate constraints and rectangular no-fly zones using mixed-integer linear programming [59]. An approximate cost-to-go was also used to account for uncertainty beyond a limited detection horizon. Another approach computes minimum-distance collision-free paths for a "Dubins-like" car with nonlinear dynamics with nonlinear programming [18]. The avoidance of circular obstacles was ensured with nonlinear constraints. The computational burden was reduced through a branch-and-bound optimization. Nonlinear programming can also be applied to motion planning by combining cellular decomposition and graph search with a predictive controller [39]. The map of the environment is partitioned into a set of connected convex regions and searched for a set of regions that connects the start and end points. A path is then parameterized as a spline, optimized within the set of convex regions, and tracked with receding horizon control. An advantage of planning with receding horizon optimization is that it can compute optimal trajectories for a wide range of models. The challenge of numerical trajectory optimization is the computational overhead, which depends on the model complexity and duration of model prediction.

Many model-agnostic planning methods are capable of planning feasible avoidance trajectories, with varying levels of optimality guarantees and computational requirements. A common challenge of these methods is the computational demand, which scales with the complexity of the model used for prediction.

### 1.3.2 Model-specific planning methods

Several motion planning methods have been proposed for specific vehicle models and avoidance trajectories. Though narrower in scope than model-agnostic methods, the use of model-specific information can be used to reduce the computational demands of the planning task. A trajectory of particular interest is the lane change maneuver, which involves a lateral displacement of distance  $D_1$  over a longitudinal distance  $D_2$ , as illustrated in the left subfigure of Fig. 1.2. The specific models of interest include the vehicle with tire friction circle constraints and vehicle point mass models.

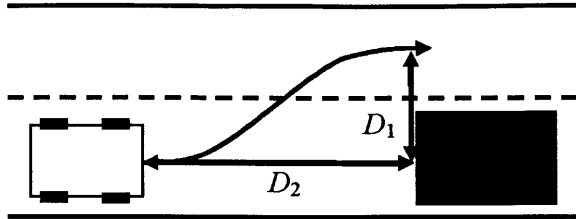


Fig. 1.2: Lane change maneuver.

The tire friction circle constraint refers to the coupling of longitudinal and lateral tire forces through a constraint on tire friction force magnitude, as illustrated in Fig. 1.3. This constraint is recognized by the professional racing community as having a significant effect during high-speed cornering [49]. For a tire with longitudinal force  $F_{xi}$ , lateral force  $F_{yi}$ , normal force  $F_{zi}$ , and surface friction coefficient  $\mu_i$ , the friction circle constraint is given as

$$\sqrt{F_{xi}^2 + F_{yi}^2} \leq \mu_i F_{zi} \quad (1.1)$$

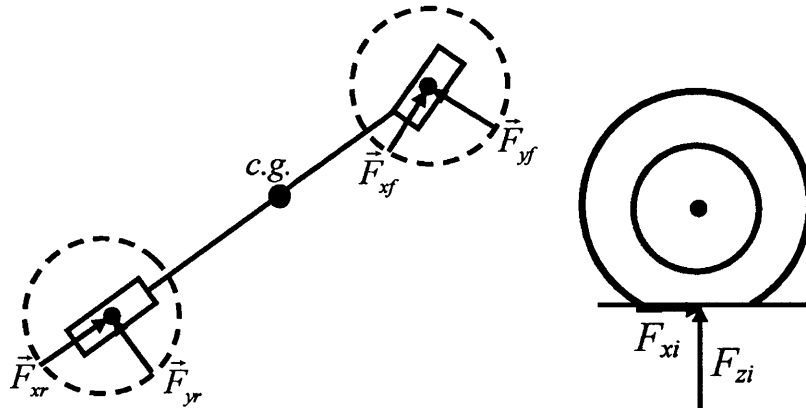


Fig. 1.3: Top view of bicycle model with tire friction circle constraints in the left subfigure and side view of tire in the right subfigure.

The optimal lane change planning problem for a vehicle with tire friction circle constraints has been considered by several researchers. The problem is posed as minimizing the longitudinal distance  $D_2$  required to change lanes a lateral distance  $D_1$  to avoid a hazard, as shown in Fig. 1.1, while satisfying friction circle constraints at each wheel. Hattori, et al. used second order cone programming to determine the optimal forces and moment on a rigid body for the lane change subject to the friction circle constraint [32]. Steering and braking commands for a higher-order model were then

computed with a second optimization step to track the desired trajectory. An alternative approach by Shiller, et al. used both numerical trajectory optimization on a high order model and analytical optimal control result for a point mass model [65]. For the point mass model, the friction circle constraint was approximated as a "friction square" and a bang-bang control law was found.

Kanarachos considered a dual of the optimal lane change planning problem by fixing the desired endpoint and minimizing the system inputs required to execute the lane change maneuver [35]. Pontryagin's Minimum Principle was used to derive a bang-bang control law for a nonlinear vehicle model with steering actuator dynamics. The approach differs from the problem considered by Shiller and Hattori in that it minimizes steering actuator commands rather than tire friction forces. Additionally, the approach does not consider the effect of braking, which was shown to be significant by both Hattori and Shiller.

Several planning methods for point mass vehicle models have been proposed. One such technique is based on the "trajectory space," a compact representation of the limits on speed and curvature imposed by stability limits and traversal of rough terrain [67]. Hazards are mapped from a cellular decomposition of the environment onto parts of the trajectory space that are inadmissible. A computationally efficient algorithm for finding a feasible trajectory was proposed, though without claims of optimality. Another method uses a point mass approximation of the vehicle dynamics to determine whether avoidance is still feasible [19]. The acceleration of simple stopping and turning maneuvers is compared to an acceleration threshold to determine feasibility. The method is computationally efficient, though ignores many vehicle dynamic effects.

Approximation of the vehicle dynamics as a point mass was used by Velenis and Tsotras to simplify optimization of the velocity profile of a trajectory along a pre-specified path [74]. The point mass simplification allowed the friction circle constraint to be mapped to a constraint on acceleration magnitude. The approach was also extended to optimization of velocity profiles for a half-car bicycle model, though the mapping of friction circle constraints to acceleration constraints is a function of vehicle state and thus more complex.

Optimal control analyses have also been presented for a point mass with bounded acceleration magnitude and controllable acceleration direction. Several example problems are considered by Bryson and Ho in their optimal control textbook, such as minimum-time orbit injection, interception, and rendezvous problems [13]. This analysis has been applied to controlling the thrust of rockets and other types of launch vehicles [13, 12], though not to ground vehicles.

Several model-specific planning methods have been proposed for planning optimal lane change maneuvers for vehicles with friction circle constraints, though analytical results are limited to reduced point mass or "friction square" models. Point mass models with bounded acceleration magnitude have been considered as approximations of the vehicle with friction circle constraints.

### **1.3.3 Motion planning summary**

A motion planning method suitable for high-speed hazard avoidance of robotic vehicles must consider high-speed vehicle dynamics, especially the friction circle constraint, with low computational demands and ideally with optimality guarantees. Several model-agnostic methods use a predictive model to ensure trajectory feasibility, though the computational complexity scales with model complexity. There are several model-specific planning techniques for vehicles with tire friction circle constraints, though they rely on trajectory optimization or model simplifications. The development of analytical solutions to the model-specific planning problem for a vehicle with tire friction circle constraints could enhance the use of model-agnostic planning methods.

## **1.4 Review of control for hazard avoidance**

Once a feasible motion plan for hazard avoidance has been generated, it should be executed by a control system with trajectory tracking guarantees. An important factor in high-performance control systems is accurate consideration of the vehicle dynamics. Two critical dynamic effects for ground vehicles are the modeling of wheel slip and the friction circle effect [49]. This section discusses previous approaches to considering these dynamic effects for trajectory tracking control of ground vehicles.

As discussed in the previous section, model complexity impacts the computational demands of motion planners that employ predictive models. This section also discusses

an approach to reducing model complexity based on differential flatness, which can reduce the kinodynamic planning problem to a geometric planning problem, while maintaining model fidelity.

### 1.4.1 Tire modeling for vehicle control

This section presents previous approaches to modeling tire slip and tire friction forces for vehicle control. Tire slip can be quantified by the relative motion between the tire contact patch and the ground [49]. Lateral slip is typically indicated by the slip angle  $\alpha$  shown in Fig. 1.4. Longitudinal slip is typically indicated by the non-dimensional value given below as  $\kappa$ , using the wheel rolling radius  $R$ , angular speed  $\omega$ , and longitudinal axle speed  $V_x$  from Fig. 1.4.

$$\kappa = 1 - \frac{R\omega}{V_x} \quad (1.2)$$

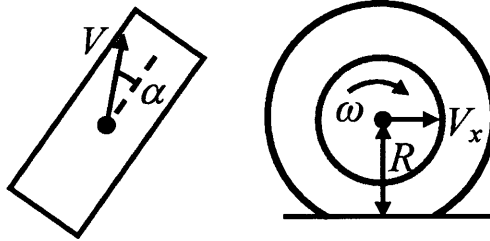


Fig. 1.4: Top view of tire with speed  $V$  and slip angle  $\alpha$  in the left subfigure and side view of tire with longitudinal axle speed  $V_x$ , angular velocity  $\omega$ , and rolling radius  $R$  in the right subfigure.

One approach to modeling tire slip and tire friction forces is to assume that no slip occurs. With this assumption, the tire friction forces can be regarded as non-holonomic constraints that maintain  $\kappa = 0$  and  $\sin \alpha = 0$  at each tire. Numerous path tracking controllers have been developed for mobile robots operating in a plane with this approach [36, 76, 22]. In particular, the pure pursuit algorithm has been applied successfully in a number of robotic vehicles, including Stanley, the winner of the 2005 DARPA Grand Challenge built by Stanford University [52, 71]. This algorithm involves computing circular arcs between the current vehicle position and a "look-ahead" point in front of the vehicle on the desired path. With the assumption of no tire slip, the steering angle is

computed based on the curvature of the circular arc. There is a speed-dependent minimum look-ahead distance required for stability of this controller.

Though the no-slip assumption may be convenient for deriving controllers analytically, it is not appropriate for all situations since wheel slip does occur in practice [49]. For example, if the magnitude of the constraint forces required by the non-holonomic constraints exceed the available friction force at a tire, then the constraints cannot be satisfied, and slip will occur. Additionally, slip can be observed in pneumatic tires as a result of tire compliance when non-zero friction forces are applied, even when the tire force magnitude is far less than the maximum available friction force [54, 63].

To account for tire compliance and friction force saturation, tire friction forces are typically modeled as nonlinear functions of slip [49, 6, 54]. When at least one slip value is small, the longitudinal force  $F_{xi}$  and lateral force  $F_{yi}$  can be modeled as uncoupled functions of slip as  $F_{xi}(\kappa)$  and  $F_{yi}(\alpha)$ . The typical shape of these uncoupled functions is illustrated in Fig. 1.5 and involves a linear region at small slip, saturation due to the friction limit, and possibly a drop-off as slip increases. At large slip values the tire friction forces are coupled as  $F_{xi}(\kappa, \alpha)$  and  $F_{yi}(\kappa, \alpha)$ . The friction circle effect is embodied in the coupling of these models. A widely used model for the coupled friction forces is the Magic Tire formula given by Pacejka [6, 54].

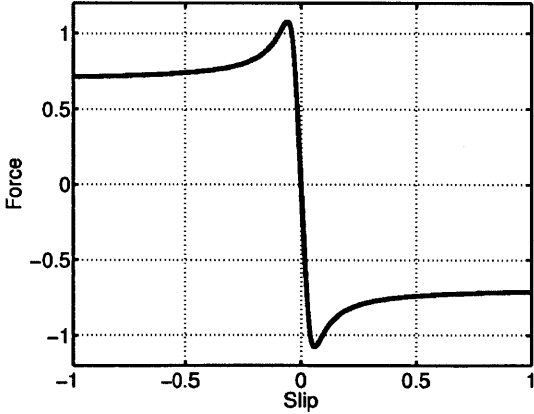


Fig. 1.5: Example relation between tire force and slip.

When tire slip is sufficiently small, the decoupled friction forces are approximately linear. Numerous vehicle control algorithms have been proposed that utilize a linear tire force model for path tracking [55, 3, 56, 41], lane-keeping [61], and stability control [17].

The linear model enables use of the many tools of linear control theory, though the model's suitability is limited to situations with relatively small amounts of vehicle slip.

The linear lane-keeping controller in [61] and the linear path-tracking controller for an autonomous race car in [41] utilize concepts of look-ahead distance similar to the pure pursuit controller. These controllers have also been extended to consider a nonlinear model of decoupled lateral tire forces  $F_{yi}(\alpha)$  [70].

Nonlinear tire models with coupled slip can be incorporated into vehicle controllers using numerical optimization methods. A coupled tire friction force model was used in a controller for rollover prevention by posing a force allocation scheme as a convex second-order cone program and solving it numerically [33]. The coupled tire model is given as

$$F_{yi}(\alpha, F_{xi}) = f_{yi}(\alpha) \sqrt{1 - (F_{xi} / \mu F_{zi})^2} \quad (1.3)$$

where  $f_{yi}(\alpha)$  is a decoupled lateral force model,  $\mu$  is the surface friction coefficient, and the term  $\sqrt{1 - (F_{xi} / \mu F_{zi})^2}$  represents the friction circle effect. This is a simplified form of the coupled nonlinear tire model that can be used for control.

The coupled nonlinear tire model from [6] was used with nonlinear model predictive control (MPC) to generate a path-tracking controller for an automobile operating near the tire friction limits [21]. The controller was demonstrated experimentally with double lane change maneuvers at speeds up to 21 m/s on icy roads. A linear affine model was used to approximate the rear lateral tire forces in a linear MPC controller for maintaining the vehicle in its operating envelope [7]. The front lateral tire force was treated as an input to this vehicle control scheme as low-level tire force control was available from the actuators on this vehicle.

A controller for stabilizing the vehicle speed, sideslip angle, and yaw rate to an equilibrium drifting maneuver at high slip was given in [72]. The controller was designed for the coupled nonlinear tire model from [6] and employed front-wheel steering and rear wheel torque in a sliding surface control scheme. This controller explicitly considers a nonlinear tire friction model, operates at high sideslip, and is computationally efficient. Its main limitation is that it only stabilizes equilibrium drifting maneuvers and cannot track arbitrary trajectories.

The effect of tire slip and tire friction is important when vehicles are operated near the limits of friction. Tire friction forces are typically modeled as coupled nonlinear functions of the lateral slip angle and longitudinal slip. For small slip, the friction forces are approximately linear, and linear control theory can be applied for vehicle control. For larger values of slip, a nonlinear tire model should be employed. Several types of nonlinear models have been used with numerical optimization, though the complexity of the tire models should be balanced with the computational demands of real-time numerical optimization, particularly for low-power microcontrollers.

#### 1.4.2 Differential flatness in ground vehicle control

Some recent research in trajectory tracking control has focused on systems with a property known as differential flatness. A nonlinear system  $\dot{\mathbf{x}} = f(\mathbf{x}, \mathbf{u})$  is differentially flat if an output  $\mathbf{y}$  can be found such that the states  $\mathbf{x}$  and inputs  $\mathbf{u}$  can be expressed in terms of  $\mathbf{y}$  and a finite number of its derivatives [22]. A benefit of flat systems is that the differential constraints given by  $\dot{\mathbf{x}} = f(\mathbf{x}, \mathbf{u})$  are mapped into smoothness constraints on the outputs  $\mathbf{y}$ . This simplifies the kinodynamic planning problem to a geometric planning problem of finding a smooth trajectory.

An example of a flat system is the front-wheel steered bicycle driving in a plane without wheel slip. This model is a flat system whose flat output is the position of the rear wheel [22]. The flatness of the bicycle driving without slip has been applied in vehicle tracking control applications [62], though its no-slip assumption restricts its suitability for limit handling maneuvers involving significant amounts of slip.

Another example of a flat output is the position of the center of oscillation (or center of percussion) of certain types of rigid body systems, including a vertical take-off and landing aircraft [47, 50]. States related to the center of oscillation have also been identified as flat outputs for a bicycle model with tire forces acting at the front and rear wheels, as described below.

Though not identified as the center of oscillation, Ackermann noted that the lateral acceleration of a point near the front wheels is decoupled from the rear lateral tire force [1]. This decoupling was exploited to design a front-wheel steering controller for the body-fixed acceleration of that point at the front of the vehicle. Since the vehicle yaw

dynamics were decoupled from the front steering, a control law for rear-wheel steering was used to control the yaw dynamics. Recent work conducted concurrently with this thesis has applied force control at the front wheels to control the path of the front center of percussion [42].

It was later noted by Fuchshumer that both the point identified by Ackermann at the front of the vehicle and a similar point at the rear of the vehicle are centers of oscillation. The body-fixed velocity components at the rear center of oscillation were identified as flat outputs and a corresponding flatness-based controller was defined [28]. The position of the rear center of oscillation was chosen as the reference point in a trajectory tracking controller by Setlur [64]. Other flat outputs have been considered under the assumption of constant speed and linear tire force models [75, 5].

In summary, differential flatness is a system property that can simplify the motion planning problem by mapping differential state constraints to smoothness constraints on the trajectories of flat outputs. States related to the front and rear centers of oscillation have been previously considered as flat outputs for the nonlinear bicycle model. For a vehicle with front-wheel steering but no rear-wheel steering, the acceleration of the front center of oscillation has the advantage of being coupled to controllable tire friction forces at the front wheel and decoupled from the uncontrollable rear lateral friction force. The position of the front center of oscillation thus represents a promising choice of flat output for a flatness-based trajectory tracking controller.

### 1.4.3 Vehicle control summary

Two important factors in the development of trajectory tracking controllers for ground vehicles are the modeling of wheel slip and tire friction forces and the presence of differentially flat outputs in the system dynamics. Modeling tire friction forces as coupled nonlinear functions of slip captures dynamic effects such as friction force saturation and the friction circle effect. Several controllers based on numerical optimization have incorporated nonlinear tire models, though model complexity increases the computational demand of techniques based on numerical optimization. The presence of differentially flat outputs in a system model can simplify the planning task by reducing kinodynamic planning to a geometric planning problem. The position of the front center

of oscillation of the nonlinear bicycle is a promising flat output for a trajectory tracking controller.

### ***1.5 Contributions of this thesis***

High-speed hazard avoidance systems require integration of sensing, motion planning, and control subsystems. This thesis presents contributions in the areas of planning and control for hazard avoidance, assuming that the location of hazards and properties of the driving surface are known. An outline of the thesis and its contributions are presented below.

Chapter Two poses the optimal hazard avoidance planning problem considered in this thesis. The problem is based on minimization of constrained vehicle dynamic states, such as friction circle utilization. A nonlinear bicycle model is presented, and the optimal planning problem is solved numerically for this model to demonstrate properties of the corresponding optimal trajectories.

Chapter Three presents analytical solutions to the optimal hazard avoidance planning problem for a point mass with bounded acceleration magnitude. The constraint on acceleration magnitude is analogous to the friction circle constraint, which is a fundamental constraint on high-speed vehicle dynamics [49]. The method is based on analytical optimal control and can be applied in a computationally efficient manner. These results present a closer connection to high-speed vehicle dynamics than previous analytical optimal control results for the point mass approximation of ground vehicles, which utilized a "friction square" constraint [65].

Chapter Four presents a flatness-based trajectory tracking controller for a bicycle model with nonlinear tire forces. The position of the front center of oscillation is used as a flat output, and feedback control of the tire friction forces is used to control the acceleration of the flat output. This decouples the bicycle dynamics into a point mass with two degrees of freedom and an additional degree of freedom related to the yaw dynamics. A Lyapunov stability analysis of the yaw dynamics is presented for steady maneuvers. The friction circle constraint at the front wheels of the bicycle is shown to be equivalent to an acceleration circle constraint. This insight allows the optimal avoidance trajectories for the point mass to be applied to a nonlinear bicycle model. It should be

noted that recent research conducted concurrently with this work has considered a path tracking controller for the front center of oscillation based on feedback control of tire friction forces [42], though the connection to differential flatness and nonlinear stability analysis presented in this work are novel.

In Chapter Five, the planning and control contributions are demonstrated in a hazard avoidance system. The system plans optimal hazard avoidance trajectories that minimize acceleration magnitude. When the acceleration required for avoidance exceeds a threshold, active steering and braking are employed to automatically avoid the hazards. The system is demonstrated experimentally to verify the performance and computational efficiency of the algorithms.

In Chapter Six, conclusions are presented along with suggestions for future work.

# 2

## **CHAPTER 2: OPTIMAL AVOIDANCE PROBLEM**

### ***2.1 General form of optimal avoidance planning problem***

A general form of the optimal motion planning problem is presented below. The problem considers a vehicle with nonlinear dynamics subject to two types of nonlinear constraints. One set of constraints arises from requiring a minimum clearance from hazards, while the other constraints correspond to the nonlinear operating envelope on vehicle states. The planning problem is posed as finding a trajectory that satisfies the minimum clearance constraints while minimizing a function related to the operating envelope that represents aggressiveness.

A vehicle with states  $\mathbf{x}$ , inputs  $\mathbf{u}$ , and nonlinear dynamics  $\dot{\mathbf{x}} = f(\mathbf{x}, \mathbf{u})$  is considered. The vehicle is subject to input magnitude constraints and nonlinear operating envelope constraints that may arise from friction force limits or rollover stability limits. These constraints can be expressed generally as  $|g_i(\mathbf{x}, \mathbf{u})| \leq 1$ ,  $i \in \{1 \dots N_g\}$ . The clearance between the vehicle and the nearest hazard should be computed and is given by  $r(\mathbf{x})$ . A candidate trajectory with states  $\mathbf{x}(t)$  and inputs  $\mathbf{u}(t)$  for  $t \in [0, T]$  is a dynamically feasible hazard avoidance trajectory if it satisfies the constraints listed above, as well as the clearance constraint  $r(\mathbf{x}(t)) \geq r_0 > 0$  for  $t \in [0, T]$ , where  $r_0$  is the minimum required clearance.

It may be noted that feasible hazard avoidance trajectories may not exist from all initial vehicle states. For example, vehicles have a minimum stopping distance that depends on the surface conditions and the vehicle speed. If the hazard is closer than the minimum stopping distance, it cannot be avoided by stopping. This is related to the concept of inevitable collision states [26].

Since the operating envelope constraints  $|g_i(\mathbf{x}, \mathbf{u})| \leq 1$  limit the space of feasible trajectories, an optimal planning problem is posed that minimizes these constrained

quantities  $|g_i(\mathbf{x}, \mathbf{u})|$ , while maintaining at least a minimum hazard clearance  $r_0$ . The problem statement is given below:

$$\mathbf{u}^* = \arg \min_{\mathbf{u}} \max_{i,t} |g_i(\mathbf{x}(t), \mathbf{u}(t))| \quad (2.1)$$

$$\dot{\mathbf{x}} = f(\mathbf{x}, \mathbf{u}) \quad (2.2)$$

$$r(\mathbf{x}(t)) \geq r_0 \quad (2.3)$$

This optimization minimizes the peak value of any constrained quantity at any time during the trajectory. Since the constrained quantities  $|g_i(\mathbf{x}, \mathbf{u})|$  are minimized, the constraints are omitted from the problem statement. An advantage of minimizing the peak value of  $|g_i(\mathbf{x}, \mathbf{u})|$  over all  $i$  and  $t$  is that the dynamic feasibility of the resulting trajectory can be easily verified by testing whether the objective is less than 1. A disadvantage of this definition of the objective is that it treats all envelope constraints  $|g_i(\mathbf{x}, \mathbf{u})|$  equally. Additionally, there may be multiple trajectories that have the same peak value of the envelope constraints, which implies non-unique optimal trajectories.

To address these disadvantages, a variant of the trajectory optimization problem is posed by subjecting a subset of the constrained quantities with indices  $i \in A$  to the minimization with the other quantities  $i \notin A$  remaining constrained. The quantities in  $A$  can be chosen based on the relative danger of nearness to each envelope constraint. The variant of the problem is posed as follows:

$$\mathbf{u}^* = \arg \min_{\mathbf{u}} \max_{i \in A, t} |g_i(\mathbf{x}(t), \mathbf{u}(t))| \quad (2.4)$$

$$\dot{\mathbf{x}} = f(\mathbf{x}, \mathbf{u}) \quad (2.5)$$

$$r(\mathbf{x}(t)) \geq r_0 \quad (2.6)$$

$$|g_i(\mathbf{x}(t), \mathbf{u}(t))| \leq 1, i \notin A \quad (2.7)$$

The following sections present and discuss the optimal trajectories computed using this method for a nonlinear bicycle made subject to friction circle constraints.

## 2.2 Nonlinear bicycle model

A nonlinear bicycle model is presented here and illustrated in Fig. 2.1 using the notation from [47]. A fixed inertial frame is given by  $(\vec{i}, \vec{j}, \vec{k})$ . The vehicle is modeled as a rigid body in the plane formed by vectors  $\vec{i}, \vec{j}$ . A body-fixed frame is given as

$(\vec{i}_b, \vec{j}_b, \vec{k}_b)$  with  $\vec{k}_b = \vec{k}$  and the yaw angle  $\psi$ . The vehicle center of gravity (c.g.) is located at point  $c$  and has position  $\vec{r}_c$ , velocity  $\vec{v}_c$ , and acceleration  $\vec{a}_c$  as shown below. The state vector  $\mathbf{x}$  is given as well.

$$\vec{r}_c = X_c \vec{i} + Y_c \vec{j} \quad (2.8)$$

$$\vec{v}_c = \dot{X}_c \vec{i} + \dot{Y}_c \vec{j} \quad (2.9)$$

$$\vec{a}_c = \ddot{X}_c \vec{i} + \ddot{Y}_c \vec{j} \quad (2.10)$$

$$\mathbf{x} = [X_c \ Y_c \ \psi \ \dot{X}_c \ \dot{Y}_c \ \dot{\psi}]^T \quad (2.11)$$

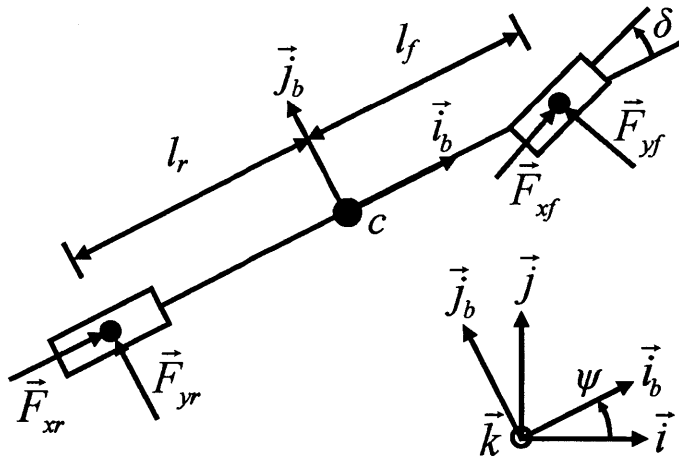


Fig. 2.1: Nonlinear bicycle model with front-wheel steering and tire friction forces.

The forces acting on the vehicle are lateral and longitudinal tire friction forces at the front and rear wheels as shown below, where  $\delta$  is the front steering angle.

$$\vec{F}_{xf} = F_{xf} (\vec{i}_b \cos \delta + \vec{j}_b \sin \delta) \quad (2.12)$$

$$\vec{F}_{yf} = F_{yf} (-\vec{i}_b \sin \delta + \vec{j}_b \cos \delta) \quad (2.13)$$

$$\vec{F}_{xr} = F_{xr} \vec{i}_b \quad (2.14)$$

$$\vec{F}_{yr} = F_{yr} \vec{j}_b \quad (2.15)$$

The vehicle dynamics are written in the vehicle-fixed frame as:

$$m \vec{a}_c = \vec{F}_{xf} + \vec{F}_{yf} + \vec{F}_{xr} + \vec{F}_{yr} \quad (2.16)$$

$$m \vec{a}_c = (F_{xf} \cos \delta - F_{yf} \sin \delta + F_{xr}) \vec{i}_b + (F_{xf} \sin \delta + F_{yf} \cos \delta + F_{yr}) \vec{j}_b \quad (2.17)$$

$$I_{zz} \ddot{\psi} \vec{k} = l_f \vec{i}_b \times (\vec{F}_{xf} + \vec{F}_{yf}) - l_r \vec{i}_b \times (\vec{F}_{xr} + \vec{F}_{yr}) \quad (2.18)$$

where  $m$  is the vehicle mass,  $I_{zz}$  is the yaw moment of inertia, and the parameters  $l_f$  and  $l_r$  specify the location of the tire-ground contact points relative to  $c$ .

The dynamics are expanded and projected into the fixed frame as shown below.

$$m\ddot{X}_c = F_{xf} \cos(\psi + \delta) - F_{yf} \sin(\psi + \delta) + F_{xr} \cos \psi - F_{yr} \sin \psi \quad (2.19)$$

$$m\ddot{Y}_c = F_{xf} \sin(\psi + \delta) + F_{yf} \cos(\psi + \delta) + F_{xr} \sin \psi + F_{yr} \cos \psi \quad (2.20)$$

$$I_{zz}\ddot{\psi} = l_f(F_{xf} \sin \delta + F_{yf} \cos \delta) - l_r F_{yr} \quad (2.21)$$

Tire friction forces are modeled as the product of the normal force  $F_{zi}$  and a function of the slip between the tire contact patch and the road surface [54]. The lateral tire slip angles at the front and rear are given by  $\alpha_f$  and  $\alpha_r$  and are computed as shown below.

$$\alpha_f(\mathbf{x}, \delta) = \tan^{-1} \left( \frac{\vec{v}_c \cdot \vec{j}_b + l_f \dot{\psi}}{\vec{v}_c \cdot \vec{i}_b} \right) - \delta \quad (2.22)$$

$$\alpha_r(\mathbf{x}) = \tan^{-1} \left( \frac{\vec{v}_c \cdot \vec{j}_b - l_r \dot{\psi}}{\vec{v}_c \cdot \vec{i}_b} \right) \quad (2.23)$$

An example tire with slip angle  $\alpha_i$  and speed  $v_i$  is illustrated in the left subfigure of Fig. 2.2. The longitudinal slip ratio  $\kappa_i$  is also defined below, where  $r_i$  is the tire radius and  $\omega_i$  is the wheel angular velocity about the axle, as shown in the right subfigure of Fig. 2.2.

$$\kappa_i(\mathbf{x}, \omega_i) = 1 - \frac{r_i \omega_i}{v_i \cos \alpha_i} \quad (2.24)$$

The wheel spin dynamics are given below for each tire, where  $I_i$  is moment of inertia of the wheel about the spinning axis, and  $\tau_i$  is the control torque applied to the wheel, as shown in the right subfigure of Fig. 2.2.

$$I_i \ddot{\omega}_i = \tau_i - r_i F_{xi} \quad (2.25)$$

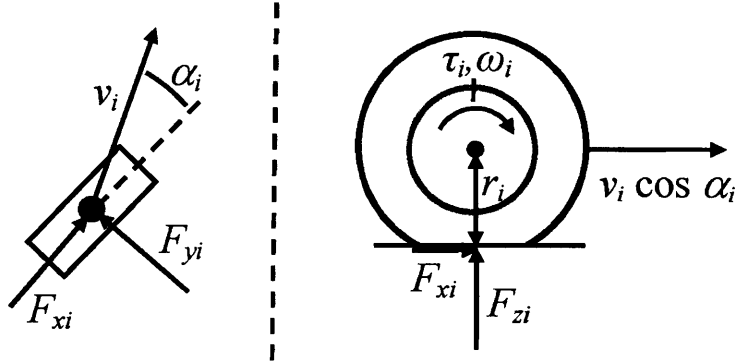


Fig. 2.2: Lateral and longitudinal tire friction forces and tire slip quantities.

Tire friction forces always oppose the direction of tire slip. This physical insight is expressed in the following inequalities:

$$F_{xi}(\kappa_i)\kappa_i < 0 \quad \forall \kappa_i \neq 0 \quad (2.26)$$

$$F_{yi}(\alpha_i)\sin \alpha_i < 0 \quad \forall \sin \alpha_i \neq 0 \quad (2.27)$$

Additionally, the friction forces are modeled such that the forces are zero when the slip is zero as follows:

$$\kappa_i = 0 \Leftrightarrow F_{xi}(\kappa_i) = 0 \quad (2.28)$$

$$\sin \alpha_i = 0 \Leftrightarrow F_{yi}(\alpha_i) = 0 \quad (2.29)$$

When the slip in one direction is small, the tire forces are approximated as functions of a single slip value only, as in the equations below.

$$F_{xi}(\kappa_i, F_{zi}) = F_{zi}f_{xi}(\kappa_i) \quad \forall |\alpha_i| \leq \tilde{\alpha}_i \quad (2.30)$$

$$F_{yi}(\alpha_i, F_{zi}) = F_{zi}f_{yi}(\alpha_i) \quad \forall |\kappa_i| \leq \tilde{\kappa}_i \quad (2.31)$$

An example of a relationship between force and slip was given in Fig. 1.5. This example relationship is linear for small values of slip and saturates at a maximum friction force value. The friction force may experience a drop-off after saturation as slip increases.

When both the lateral and longitudinal slip values are large, the tire friction forces are coupled functions of both slip values:

$$F_{xi}(\kappa_i, \alpha_i, F_{zi}) = F_{zi}f_{xi}(\kappa_i, \alpha_i) \quad (2.32)$$

$$F_{yi}(\kappa_i, \alpha_i, F_{zi}) = F_{zi}f_{yi}(\kappa_i, \alpha_i) \quad (2.33)$$

This coupling is often referred to as the friction circle effect [49] and is based on the fact that the total friction force magnitude is bounded, as shown in the equation below and illustrated in the left subfigure of Fig. 2.3. The variable  $\mu$  refers to the saturated friction coefficient between the tire and the surface.

$$\sqrt{F_{xi}^2 + F_{yi}^2} \leq \mu F_{zi} \quad (2.34)$$

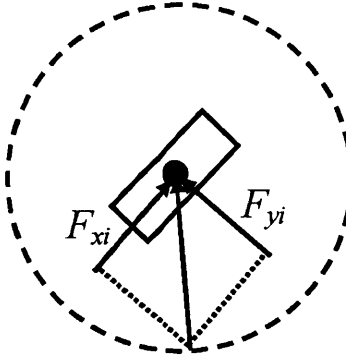


Fig. 2.3: Illustration of friction circle constraint.

To simplify the coupled tire model, it is assumed that the control torque  $\tau_i$  is used to control the longitudinal force  $F_{xi}$  to track a desired force  $F_{xi,des}$  as shown below. The force  $F_{xi}$  tracks the desired value closely when the spin acceleration  $\dot{\omega}_i$  is small. This implies that the desired force must be lower than the saturation value of the longitudinal force.

$$\tau_i = r_i F_{xi,des} \Rightarrow F_{xi}(\kappa_i, \alpha_i, F_{zi}) = F_{xi,des} - \frac{I_i \dot{\omega}_i}{r_i} \quad (2.35)$$

The input vector  $\mathbf{u}$  is given below, which consists of the steering angle  $\delta$  and the longitudinal forces  $F_{xf}$  and  $F_{xr}$ .

$$\mathbf{u} = [\delta \quad F_{xf} \quad F_{xr}]^T \quad (2.36)$$

With the longitudinal forces  $F_{xi}$  treated as an input, the lateral force  $F_{yi}$  is modeled as the product of the normal force  $F_{zi}$ , a function of lateral slip angle  $\alpha_i$ , and the friction circle coupling term shown below.

$$F_{yi}(\alpha_i, F_{xi}, F_{zi}) = F_{zi} f_{yi}(\alpha_i) \sqrt{1 - \left( \frac{F_{xi}}{\mu F_{zi}} \right)^2} \quad (2.37)$$

For this work, the function of lateral slip  $f_{yi}(\alpha_i)$  is based on Pacejka's Magic Formula, a semi-empirical tire model [54]. The formula is modified to include rotational symmetry for large angles so that  $f_{yi}(\alpha) = f_{yi}(\beta)$  if  $\sin(\alpha) = \sin(\beta)$ . The angle  $\bar{\alpha}_i$  is defined by mapping the angle  $\alpha_i$  to the interval  $[-\pi/2, \pi/2]$  as shown below. The function  $f_{yi}(\alpha_i)$  is given below as well, with parameters  $B$ ,  $C$ ,  $D$ , and  $E$ . The parameter  $B$  is the stiffness parameter and is closely related to the slope of the curve at  $\alpha_i = 0$ . The parameter  $C$  is the shape factor and determines the shape of the peak of the curve. The parameter  $D$  is the peak factor and scales the magnitude of the curve. The parameter  $E$  is the curvature factor and influences the shape of the curve for large values of  $\alpha_i$ .

$$\bar{\alpha}_i(\alpha_i) = \sin^{-1} \sin \alpha_i \quad (2.38)$$

$$f_{yi}(\alpha_i) = D_i \sin(C_i \tan^{-1}(B_i(1 - E_i)\bar{\alpha}_i(\alpha_i) + E_i \tan^{-1}(B_i \bar{\alpha}_i(\alpha_i)))) \quad (2.39)$$

Parameters for the front and rear lateral force on a low-friction road are taken from [53] and are given in Table 2.1. The functions  $f_{yf}(\alpha_f)$  and  $f_{yr}(\alpha_r)$  are plotted in Fig. 2.4 for a range of slip angles.

Table 2.1: Model Parameters

Symbol	Description	Value
$l_f$	Dist. From C.G. to front	1.2 m
$l_r$	Dist. from C.G. to rear	1.3 m
$m$	Mass	1500 kg
$I_{zz}$	Yaw moment of inertia	3000 kg m <sup>2</sup>
$B_f$	Front tire parameter	11.275 rad <sup>-1</sup>
$C_f$	Front tire parameter	1.5600
$D_f$	Front tire parameter	-0.3365
$E_f$	Front tire parameter	-1.9990
$ \alpha_{f,peak} $	Slip at peak $F_{yf}$	5.46 deg
$\mu_f$	Peak front friction	0.337
$B_r$	Rear tire parameter	18.631 rad <sup>-1</sup>
$C_r$	Rear tire parameter	1.5600
$D_r$	Rear tire parameter	-0.2477
$E_r$	Rear tire parameter	-1.7908
$ \alpha_{r,peak} $	Slip at peak $F_{yr}$	3.39 deg
$\mu_r$	Peak rear friction	0.248

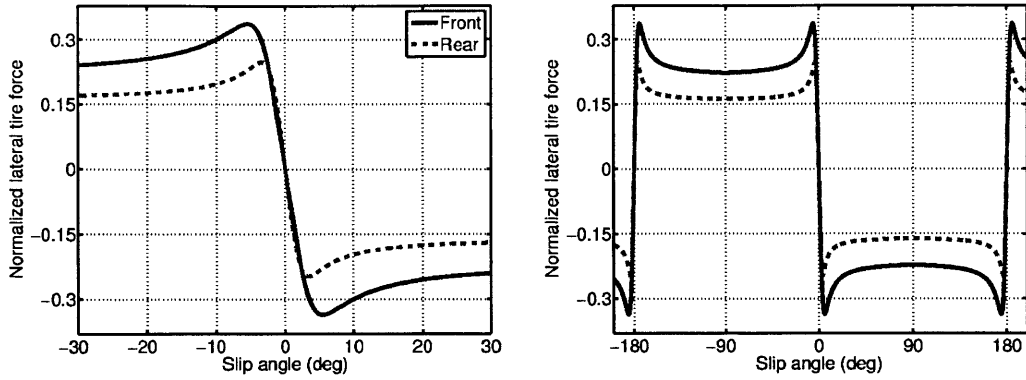


Fig. 2.4: Normalized lateral tire force functions  $f_{yy}(\alpha_f)$  and  $f_{yy}(\alpha_r)$  based on Pacejka model. The functions are plotted for two ranges of the rear slip angle to show the linearity and saturation at small slip angles and the symmetry at large slip angles.

Another important factor in tire friction force modeling is the variation of the normal force  $F_{zi}$ . When a vehicle is subject to heavy braking or acceleration, load can be shifted between the normal forces at the front and rear. This effect is often referred to as load transfer [49]. A vehicle with c.g. height  $h$  that is subject to a longitudinal acceleration  $a_x$  is illustrated in Fig. 2.5. Expressions for the normal forces  $F_{zf}$  and  $F_{zr}$  are given below, where  $g$  represents the acceleration due to gravity.

$$F_{zf} = mg \frac{l_r}{l_f + l_r} - ma_x \frac{h}{l_f + l_r} \quad (2.40)$$

$$F_{zr} = mg \frac{l_f}{l_f + l_r} + ma_x \frac{h}{l_f + l_r} \quad (2.41)$$

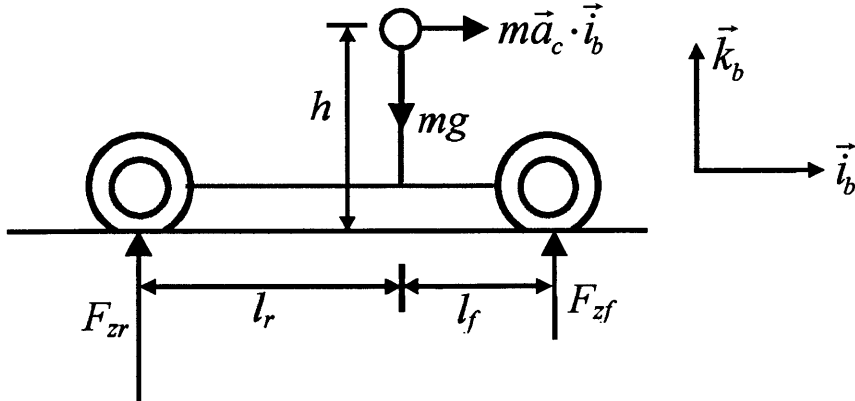


Fig. 2.5: Load transfer for nonlinear bicycle model with raised c.g.

If the maximum longitudinal acceleration is limited to  $\mu g$ , the effect of load transfer is small when  $\mu h$  is small relative to  $l_f$  and  $l_r$ . This may occur when the vehicle c.g. is low to the ground and/or the friction coefficient is low, such as a sports car on a slippery surface. For the duration of this work, it is assumed that  $\mu h$  is small relative to  $x_f$  and  $x_r$ , so that the normal forces are approximated as constant and computed as shown below.

$$F_{zf} = mg \frac{l_r}{l_f + l_r} \quad (2.42)$$

$$F_{zr} = mg \frac{l_f}{l_f + l_r} \quad (2.43)$$

The inputs are subject to the constraints given below, where  $\delta_{max}$  represents the maximum steering angle, and  $F_{xf,max}$  and  $F_{xr,max}$  represent the maximum longitudinal forces.

$$|\delta| \leq \delta_{max} \quad (2.44)$$

$$|F_{xf}| \leq F_{xf,max} \quad (2.45)$$

$$|F_{xr}| \leq F_{xr,max} \quad (2.46)$$

The friction forces at the front and rear tires are also subject to friction circle constraints given below, where  $\mu$  is the surface friction coefficient.

$$\sqrt{F_{xf}^2 + F_{yf}^2} \leq \mu F_{zf} \quad (2.47)$$

$$\sqrt{F_{xr}^2 + F_{yr}^2} \leq \mu F_{zr} \quad (2.48)$$

### 2.3 Example optimal avoidance trajectory for nonlinear bicycle

The hazard avoidance trajectory optimization problem defined in (2.4)-(2.7) is now applied to the nonlinear bicycle model presented in the previous section. The optimization problem is solved numerically to illustrate characteristics of the resulting avoidance trajectories.

For this example, the inputs  $F_{xf}$  and  $F_{xr}$  represent braking forces generated by a proportional braking system, with desired braking command  $u_{brake}$  with parameter  $0 \leq b \leq 1$  as shown below.

$$F_{xf}(\mathbf{u}) = bu_{brake} \quad (2.49)$$

$$F_{xr}(\mathbf{u}) = (1 - b)u_{brake} \quad (2.50)$$

The problem is further simplified through a reduction in the number of constraints. The nonlinear bicycle is subject to constraints on steering angle, longitudinal force, and friction force magnitude. It is necessary to choose the constraints for which the vehicle behavior should be optimized. Since the braking force actuators can typically generate a force that is larger than the force allowed by friction circle constraints, then the friction circle constraints are more restrictive and the braking force constraint may be ignored. At low speed and low slip angles, the steering angle constraints limit path curvature. At high slip angles, the steering angle constraints limit vehicle controllability, as the front friction forces saturate at high slip angles. At high speeds and small slip angles, the friction circle constraints limit maneuverability. In particular, the front friction circle constraint is important because only the front wheel has steering control. Additionally, previous studies have found the front friction constraint to be more critical to understeering (or plow out) than the rear friction constraint [21]. As such, the front friction circle constraint is chosen as the constraint to be minimized.

The problem can thus be expressed as follows:

$$\mathbf{u}^* = \arg \min_{\mathbf{u}} \max_{i \in A, t} \frac{\sqrt{F_{xj}(\mathbf{u})^2 + F_{yj}(\mathbf{x}, \mathbf{u})^2}}{\mu F_{zj}} \quad (2.51)$$

$$m\ddot{X} = (b \cos(\psi + \delta) + (1 - b) \cos \psi) u_{brake} - F_{yf}(\mathbf{x}, \mathbf{u}) \sin(\psi + \delta) - F_{yr}(\mathbf{x}, \mathbf{u}) \sin \psi \quad (2.52)$$

$$m\ddot{X} = (b \sin(\psi + \delta) + (1 - b) \sin \psi) u_{brake} + F_{yf}(\mathbf{x}, \mathbf{u}) \cos(\psi + \delta) + F_{yr}(\mathbf{x}, \mathbf{u}) \cos \psi \quad (2.53)$$

$$I_{zz}\ddot{\psi} = l_f b u_{brake} \sin \delta + l_f F_{yf}(\mathbf{x}, \mathbf{u}) \cos \delta - l_r F_{yr}(\mathbf{x}, \mathbf{u}) \quad (2.54)$$

$$r(\mathbf{x}(t)) \geq r_0 \quad (2.55)$$

$$|\delta| \leq \delta_{\max} \quad (2.56)$$

$$-u_{brake, \max} \leq u_{brake} \leq 0 \quad (2.57)$$

$$\sqrt{F_{xr}^2 + F_{yr}^2} \leq \mu F_{zr} \quad (2.58)$$

This optimization problem was solved numerically using a shooting method with a nonlinear optimization package NPSOL. NPSOL uses a sequential quadratic programming algorithm to minimize a smooth nonlinear objective function subject to linear and nonlinear constraints [29]. The solver has the capability to use gradients of the

cost and constraint functions to speed convergence. Symbolic derivatives are used in the model prediction, cost function, and constraints of the MPC controller to improve performance.

An optimal trajectory is computed for a vehicle traveling in a channel with an angled rectangular hazard, as shown in Fig. 2.6. The initial speed of the vehicle is 10 m/s. The trajectory is shown with circles superimposed over the path that indicate the required clearance from hazards. A plot of the front friction circle utilization is given in Fig. 2.7. It can be seen that the optimal trajectory maintains an approximately constant level of friction utilization and brushes past the hazard and road edge with the minimum acceptable clearance.

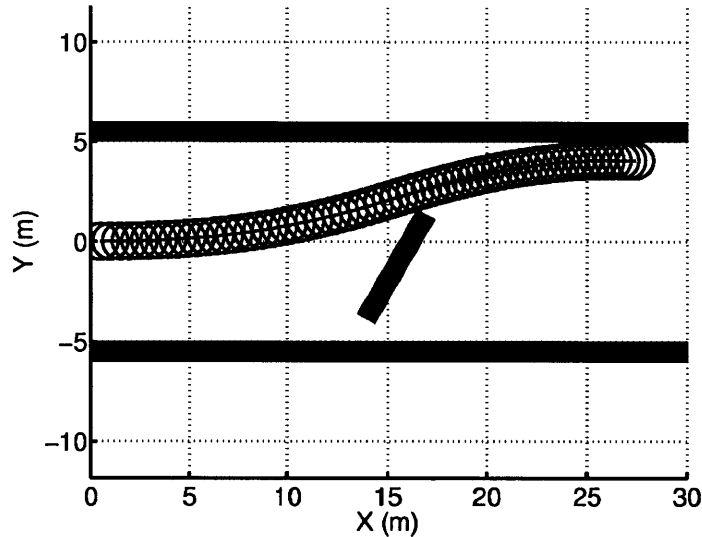


Fig. 2.6: Optimal trajectory computed numerically

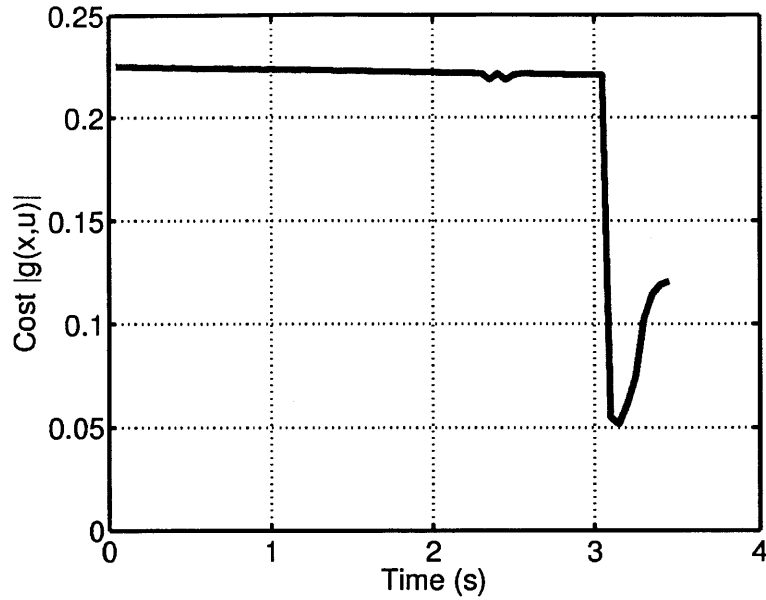


Fig. 2.7: Friction circle utilization for optimal trajectory

This example illustrates the types of avoidance trajectories that are found by this optimal planning algorithm. By including clearance from hazards in the constraints rather than in the objective to be minimized, this algorithm often computes near-miss trajectories that pass hazards with the minimum required clearance. The numerical optimization used in this example is not suitable for real-time application, requiring more than 30 seconds on a modern laptop processor to compute 3 seconds of an optimal trajectory. The following chapters will address more efficient methods for computing these types of optimal avoidance trajectories that minimize front friction circle utilization while ensuring a minimum clearance from hazards.

## 2.4 Conclusion

An optimal planning method for hazard avoidance trajectories has been presented. The method minimizes constrained quantities in the dynamics while maintaining a minimum clearance from hazards. The method has been demonstrated for a nonlinear bicycle model with a numerical optimization package. The computational time for the numerical optimization is slower than 1/10<sup>th</sup> real time, which motivates the need for more efficient methods.

# 3

## **CHAPTER 3: POINT MASS OPTIMAL AVOIDANCE**

### **3.1 Introduction**

An optimal hazard avoidance planning problem was outlined in the previous chapter. The problem was solved for a nonlinear bicycle model with friction circle constraints using numerical optimization. Since the nonlinear optimization is computationally expensive, it is desired to find efficient methods for planning optimal avoidance maneuvers. In this chapter, analytical solutions to the optimal avoidance planning problem are presented for a point mass subject to acceleration circle constraints, similar to the friction circle constraints acting on the nonlinear bicycle model. The optimal maneuvers are compared to straight-line stopping and constant radius turn maneuvers.

### **3.2 Point mass with acceleration circle constraint**

A simplified vehicle model is considered in this section, similar to the model discussed by Bryson [13]. The vehicle is modeled as a point mass  $m$  with position given by states  $[X, Y]$ , as shown in Fig. 3.1. The input to the vehicle is an acceleration of magnitude  $u_1$  applied in the direction specified by the angle  $u_2$ . The point mass dynamics are given as:

$$\begin{bmatrix} \ddot{X} \\ \ddot{Y} \end{bmatrix} = u_1 \begin{bmatrix} \sin u_2 \\ \cos u_2 \end{bmatrix} \quad (3.1)$$

The acceleration magnitude  $|u_1|$  is limited by the product of a surface friction coefficient  $\mu$  and normal force  $N$  divided by the system mass  $m$ , as shown below. This constraint is analogous to the tire friction circle constraints acting on the bicycle model.

$$|u_1| \leq \frac{\mu N}{m} = a_{\max} \quad (3.2)$$

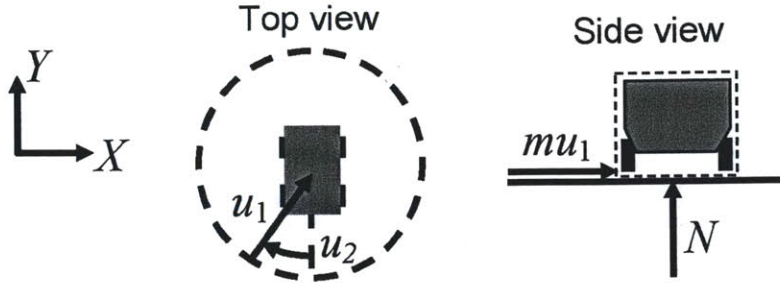


Fig. 3.1: Point mass with acceleration circle constraint.

The model is posed in state-space form with state vector  $\mathbf{x} = [X \ Y \ \dot{X} \ \dot{Y}]^T$  and input vector  $\mathbf{u} = [u_1 \ u_2]^T$  as:

$$\dot{\mathbf{x}} = f(\mathbf{x}, \mathbf{u}) = [\dot{X} \ \dot{Y} \ u_1 \sin u_2 \ u_1 \cos u_2]^T \quad (3.3)$$

The initial state and speed of the vehicle are given as  $\mathbf{x}_o$  and  $V_o$  as shown below.

$$\mathbf{x}_o = [X_o \ Y_o \ \dot{X}_o \ \dot{Y}_o]^T \quad (3.4)$$

$$V_o = \sqrt{\dot{X}_o^2 + \dot{Y}_o^2} \quad (3.5)$$

### 3.3 Geometric avoidance maneuvers for a single hazard

When hazards are located close together, they may be considered "interacting hazards", which means that avoidance maneuvers must consider them simultaneously [57]. When hazards in the environment are spaced far apart, the hazards may be considered "non-interacting" so that avoidance maneuvers can be designed for each hazard independently. This chapter considers maneuvers for avoiding a single polygonal hazard. These maneuvers can be chained together to avoid multiple hazards when the hazards are non-interacting. Three non-optimal maneuvers with simple geometry are defined and will be compared to the optimal maneuvers derived later.

The geometric maneuvers to be considered are straight-line stopping and two types of constant radius turns as shown in Fig. 3.2. A straight-line stopping maneuver involves stopping with constant deceleration over a distance  $D$ . A passing turn involves passing a hazard face to the right or left, such as the turn with radius  $R_p$ . A non-passing turn involves turning to travel parallel to a hazard face, such as the turn with radius  $R_{np}$ . The size of the vehicle is ignored here, though it will be considered later in Chapter 5.

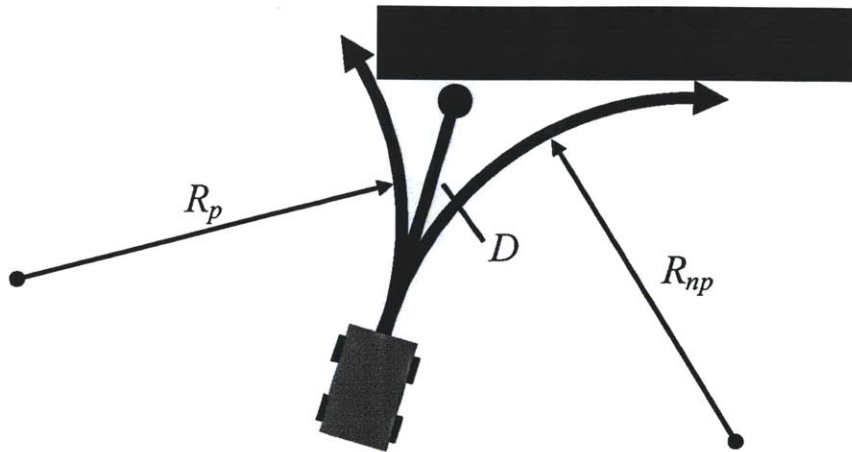


Fig. 3.2: Straight-line stopping and constant radius turn avoidance maneuvers.

The stopping distance and corresponding required acceleration  $a_s$  are computed in (3.7)-(3.8), where  $\Delta Y$  is the normal distance from the vehicle to a hazard edge and  $\theta$  is the angle between the initial vehicle velocity vector and a vector normal to the hazard edge, as shown in Fig. 3.3. The angle  $\theta$  is computed with the frame  $XY$  aligned with the hazard edge to be avoided.

$$\theta = \tan^{-1} \frac{\dot{X}_o}{\dot{Y}_o} \quad (3.6)$$

$$D = \frac{\Delta Y}{\cos \theta} \quad (3.7)$$

$$a_s = \frac{V_o^2}{2D} = \frac{V_o^2}{\Delta Y} \frac{\cos \theta}{2} \quad (3.8)$$

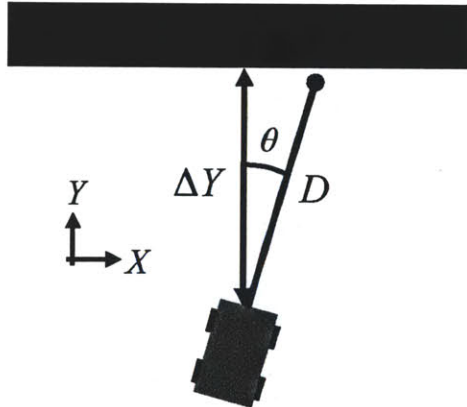


Fig. 3.3: Geometry of straight-line stopping maneuver.

The geometry and required acceleration for non-passing constant radius turns are computed below. The radius for a non-passing turn to the right is given by  $R_{np,right}$  and  $R_{np,left}$  for a turn to the left. Again,  $\Delta Y$  is the normal distance from the vehicle to the hazard edge and  $\theta$  is the angle between the vehicle velocity vector and a vector normal to the hazard edge. The geometry for non-passing turns is illustrated in Fig. 3.4.

$$R_{np,right} = \frac{\Delta Y}{1 - \sin \theta} \quad (3.9)$$

$$R_{np,left} = \frac{\Delta Y}{1 + \sin \theta} \quad (3.10)$$

$$a_{np} = \frac{V_o^2}{R_{np}} = \frac{V_o^2}{\Delta Y} (1 \pm \sin \theta) \quad (3.11)$$

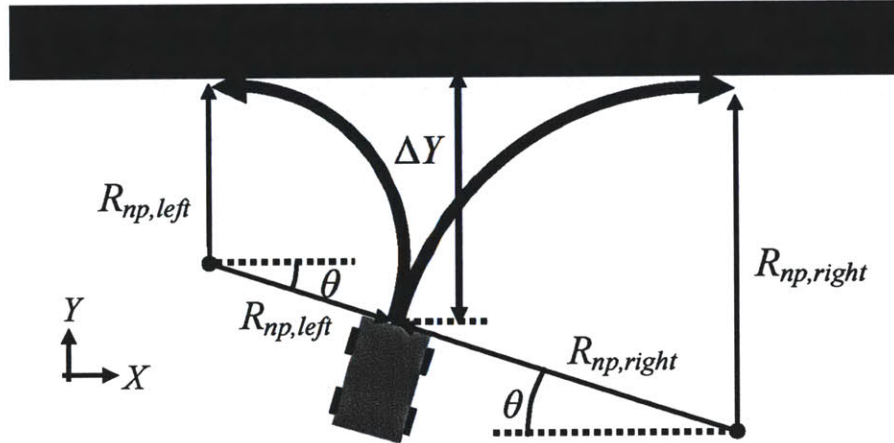


Fig. 3.4: Geometry of non-passing turns.

The geometry for passing constant radius turns is described below. Unlike non-passing turns, a single equation can be used to describe passing turns to the right or left, with radius given by  $R_p$ . Again,  $\Delta Y$  is the normal distance from the vehicle to the hazard edge and  $\theta$  is the angle between the vehicle velocity vector and a vector normal to the hazard edge. The distance along the hazard edge from the current vehicle position to the corner to be passed is given by  $\Delta X$ . The angle  $\varphi$  and distance  $\Delta D$  are defined by the angle and distance from the initial vehicle position to the corner to be passed as shown below. The passing turn geometry is illustrated in Fig. 3.5.

$$\varphi = \tan^{-1} \frac{\Delta X}{\Delta Y} \quad (3.12)$$

$$\Delta D = \sqrt{\Delta X^2 + \Delta Y^2} \quad (3.13)$$

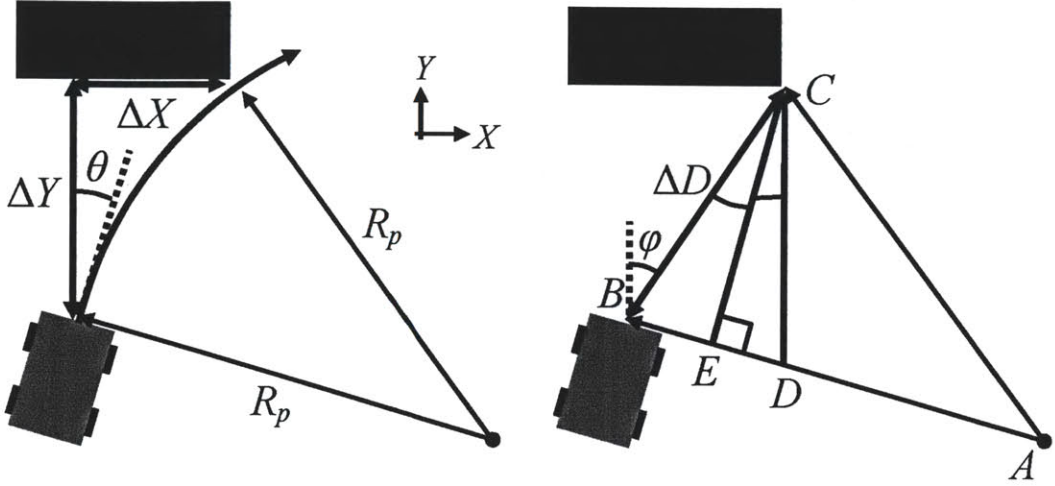


Fig. 3.5: Geometry of passing turn to the right.

The turn radius  $R_p$  is computed with the aid of the triangles illustrated in the right side of Fig. 3.5. Edge lengths  $\overline{AC}$  and  $\overline{AB}$  are both equal to the radius  $R_p$ , and edge length  $\overline{BC}$  is equal to  $\Delta D$ . Since the angles  $\angle BCE$  and  $\angle DCE$  in Fig. 3.5 are equal, it can be shown that triangle  $\triangle ABC$  is similar to triangle  $\triangle CDB$ . This similarity implies the following ratio, which is used to find an expression for the radius  $R_p$ .

$$\frac{\overline{AC}}{\overline{BC}} = \frac{\overline{BC}}{\overline{DB}} \quad (3.14)$$

$$R_p = \frac{\Delta D^2}{\overline{DB}} \quad (3.15)$$

The quantity  $\overline{DB}$  can be computed as follows:

$$\overline{DB} = 2(\Delta X \cos \theta - \Delta Y \sin \theta) \quad (3.16)$$

$$\overline{DB} = 2\Delta D \sin(\varphi - \theta) \quad (3.17)$$

A complete expression for the radius  $R_p$  and acceleration  $a_p$  is given below.

$$R_p = \frac{\Delta D}{2\sin(\varphi - \theta)} = \frac{\Delta Y}{2\sin(\varphi - \theta)\cos\varphi} \quad (3.18)$$

$$a_p = \frac{V_o^2}{\Delta Y} 2\sin(\varphi - \theta)\cos\varphi \quad (3.19)$$

It should be noted that the circular passing arc may cross the hazard edge in order to intersect the corner node, as shown in Fig. 3.6. When this occurs, a passing turn in that direction is not feasible. The feasibility can be checked by ensuring that the angle  $\varphi$  satisfies the condition given below. When passing turns are infeasible, a non-passing turn or stopping maneuver may be considered instead.

$$-\frac{\pi}{4} + \frac{\theta}{2} \leq \varphi \leq \frac{\pi}{4} + \frac{\theta}{2} \quad (3.20)$$

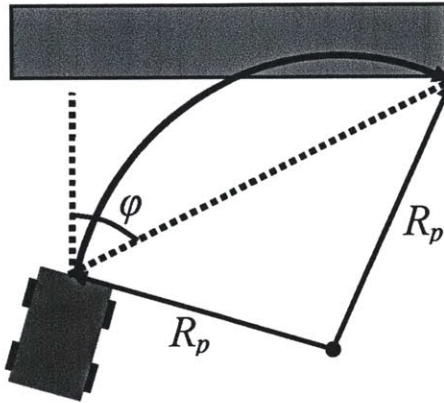


Fig. 3.6: Infeasible constant radius passing turn to the right.

### 3.4 Optimal avoidance maneuvers for a single hazard

In this section, analytical optimal control is used to derive the control laws and trajectories for two types of optimal maneuvers for a point mass with an acceleration circle constraint to avoid a single hazard.

An analog to the optimal avoidance problem for the bicycle from the previous chapter can be posed for the point mass with an acceleration circle constraint and initial state  $\mathbf{x}_0$  as shown below:

$$\mathbf{u}^* = \arg \min_{\mathbf{u}} \max_{t \in [0, T]} \frac{|u_1(t)|}{a_{\max}} \quad (3.21)$$

$$\dot{\mathbf{x}} = \begin{bmatrix} \dot{X} & \dot{Y} & u_1 \sin u_2 & u_1 \cos u_2 \end{bmatrix}^T \quad (3.22)$$

$$r(\mathbf{x}(t)) \geq 0 \quad (3.23)$$

In this form, the problem is difficult to solve analytically because the form of the function  $u_1(t)$  is unknown. An alternative optimization problem is posed that is more tractable and is proved to be equivalent to the problem above for the two maneuvers

considered in this section. Rather than fixing the hazard locations and minimizing the peak acceleration, an optimization problem is posed that fixes the peak acceleration and minimizes the initial distance from the hazard required for avoidance. Note that this optimization problem was considered by Shiller for a point mass with friction square constraint [65].

### 3.4.1 Optimal non-passing maneuver

The first optimal avoidance maneuver to be considered is the optimal non-passing maneuver. In a similar manner to the non-passing constant radius turn, the vehicle does not pass the face of the hazard. Instead, it either stops or turns to travel parallel to the hazard, as shown in Fig. 3.7. For this analysis, the inertial coordinate frame  $XY$  is aligned so that the  $Y$  axis is perpendicular to the hazard face to be avoided.

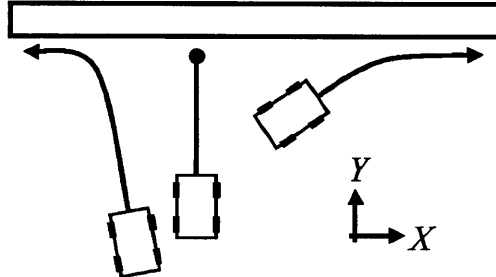


Fig. 3.7: Example non-passing turns.

If the acceleration magnitude of the non-passing turn were to be minimized, the variables  $X(T)$ ,  $\dot{X}(T)$ , and  $T$  would be free, while the variables  $Y(T)$  and  $\dot{Y}(T)$  would be fixed with  $\dot{Y}(T)=0$ . In the alternative form of the problem, the end state  $Y(T)$  is not fixed, but rather is subject to minimization as follows:

$$\mathbf{u}^* = \arg \min_{\mathbf{u}} Y(T) \quad (3.24)$$

$$\dot{\mathbf{x}} = [\dot{X} \quad \dot{Y} \quad u_1 \sin u_2 \quad u_1 \cos u_2]^T \quad (3.25)$$

$$|u_1| \leq a_{\max} \quad (3.26)$$

$$\dot{Y}(T) = 0 \quad (3.27)$$

In this form, the cost function  $J$  matches the general integral form of the cost function with  $h = Y(T)$  and  $g=0$ .

$$J = h(T, \mathbf{x}(T)) + \int_0^T g(\mathbf{x}, \mathbf{u}, t) dt \quad (3.28)$$

A Hamiltonian of the system can be written as follows, where  $p_i$  represents the  $i^{\text{th}}$  costate [40]:

$$H = p_1 \dot{X} + p_2 \dot{Y} + p_3 u_1 \sin u_2 + p_4 u_1 \cos u_2 \quad (3.29)$$

The costate dynamics are found by applying the following:

$$\dot{p}_i = -\frac{\partial H}{\partial x_i} \quad (3.30)$$

$$\frac{d}{dt} \begin{bmatrix} p_1 \\ p_2 \\ p_3 \\ p_4 \end{bmatrix} = \begin{bmatrix} 0 \\ 0 \\ -p_1 \\ -p_2 \end{bmatrix} \quad (3.31)$$

The costate dynamics are solved below with unknown constants  $c_1$ ,  $c_2$ ,  $c_3$ , and  $c_4$  and the variable  $\tau = T - t$  representing the time remaining until the end of the maneuver.

$$\begin{bmatrix} p_1 \\ p_2 \\ p_3 \\ p_4 \end{bmatrix} = \begin{bmatrix} c_1 \\ c_2 \\ c_1\tau + c_3 \\ c_2\tau + c_4 \end{bmatrix} \quad (3.32)$$

The optimal control law  $\mathbf{u}^*$  can be found by applying Pontryagin's Minimum Principle to the Hamiltonian given above.

$$\mathbf{u}^* = \arg \min_{\mathbf{u}} H \quad (3.33)$$

$$\mathbf{u}^* = \arg \min_{\mathbf{u}} u_1 (p_3 \sin u_2 + p_4 \cos u_2) \quad (3.34)$$

A bang-bang control law is found for  $u_1^*$  by minimizing  $H$  with respect to  $u_1$ .

$$u_1^* = \begin{cases} a_{\max} & p_3 \sin u_2 + p_4 \cos u_2 < 0 \\ -a_{\max} & p_3 \sin u_2 + p_4 \cos u_2 > 0 \end{cases} \quad (3.35)$$

For  $u_1 \neq 0$ , the partial derivative of  $H$  with respect to  $u_2^*$  is set to zero and yields a control law for  $u_2^*$ . Note that this is often referred to as the "bilinear tangent law" [13, 12].

$$\frac{\partial H}{\partial u_2^*} = 0 \quad (3.36)$$

$$p_3 \cos u_2^* - p_4 \sin u_2^* = 0 \quad (3.37)$$

$$\tan u_2^* = \frac{p_3}{p_4} = \frac{c_1\tau + c_3}{c_2\tau + c_4} \quad (3.38)$$

The following sign convention is proposed for the definition of  $\sin u_2^*$  and  $\cos u_2^*$ , and is used to simplify the control law for  $u_1^*$ .

$$\sin u_2^* = \frac{p_3}{\sqrt{p_3^2 + p_4^2}} \quad (3.39)$$

$$\cos u_2^* = \frac{p_4}{\sqrt{p_3^2 + p_4^2}} \quad (3.40)$$

$$p_3 \sin u_2 + p_4 \cos u_2 = \frac{p_3^2 + p_4^2}{\sqrt{p_3^2 + p_4^2}} > 0 \quad (3.41)$$

$$u_1^* = -a_{\max} \quad (3.42)$$

The following boundary conditions are applied for the free end conditions to determine the values of unknown constants in the costate dynamics.

$$p_1(T) = \frac{\partial h}{\partial X(T)} = 0 \Rightarrow c_1 = 0 \quad (3.43)$$

$$p_2(T) = \frac{\partial h}{\partial Y(T)} = 1 \Rightarrow c_2 = 1 \quad (3.44)$$

$$p_3(T) = \frac{\partial h}{\partial \dot{X}(T)} = 0 \Rightarrow c_3 = 0 \quad (3.45)$$

The free end time condition is applied as shown below to determine the value of the final unknown constant.

$$H(T) + \frac{\partial h}{\partial T} = 0 \quad (3.46)$$

$$p_4(T) \cos u_2 = 0 \Rightarrow p_4(T) = 0 \Rightarrow c_4 = 0 \quad (3.47)$$

The constants are applied to simplify the optimal control laws for  $u_2^*$  as shown below.

$$\cos u_2^* = 1 \quad (3.48)$$

The control law for an optimal non-passing maneuver consists of the maximum possible friction force ( $|u_1| = a_{\max}$ ) applied in a constant direction. The direction of the force is away from the hazard face in a perpendicular direction. With both inputs  $u_1^*$  and

$u_2^*$  constant, the optimal non-passing trajectory is found by integrating the system dynamics as shown below.

$$\dot{X}(t) = \dot{X}_o \quad (3.49)$$

$$\dot{Y}(t) = \dot{Y}_o - a_{\max} t \quad (3.50)$$

$$X(t) = X_o + \dot{X}_o t \quad (3.51)$$

$$Y(t) = Y_o + \dot{Y}_o t - \frac{1}{2} a_{\max} t^2 \quad (3.52)$$

Several optimal non-passing trajectories are illustrated in Fig. 3.8 for different initial conditions.

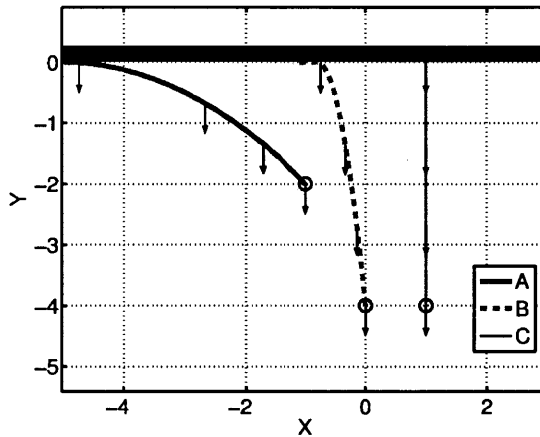


Fig. 3.8: Optimal non-passing turns. A:  $\theta = -45$  deg, B:  $\theta = -5.7$  deg, C:  $\theta = 0$ .

For these maneuvers, the direction of applied force is constant in the global frame, though it can vary with respect to the vehicle bearing. In Cases A and B in Fig. 3.8, the applied force contains components that are both parallel to and perpendicular to the vehicle velocity vector. As the maneuver progresses, the perpendicular component increases, while the parallel component decreases. Case C is a special case in which there is no perpendicular component for the entire maneuver. The angles between the force and velocity vector for the trajectories in Fig. 3.8 are shown in Fig. 3.9.

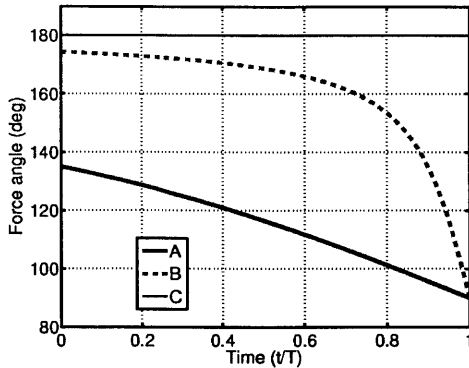


Fig. 3.9: Orientation of applied force relative to velocity vector for optimal non-passing trajectories from Fig. 3.8.

Given the end condition  $\dot{Y}(T)=0$  and the dynamics above, the end time  $T$  is computed as:

$$T = \frac{\dot{Y}_o}{a_{\max}} \quad (3.53)$$

The distances  $\Delta X = X(T) - X_o$  and  $\Delta Y = Y(T) - Y_o$  are found using the end time  $T$  and the dynamics as shown below. A proportional relationship between the ratio of these distances and the initial velocity components is shown as well.

$$\Delta X = X(T) - X_o = \frac{\dot{X}_o \dot{Y}_o}{a_{\max}} \quad (3.54)$$

$$\Delta Y = Y(T) - Y_o = \frac{\dot{Y}_o^2}{2a_{\max}} \quad (3.55)$$

$$\frac{\Delta X}{\Delta Y} = 2 \frac{\dot{X}_o}{\dot{Y}_o} \quad (3.56)$$

It can be seen that the product of the distance to the hazard  $\Delta Y$  and the maximum acceleration  $a_{\max}$  is a constant.

$$a_{\max} \Delta Y = \frac{1}{2} \dot{Y}_o^2 \quad (3.57)$$

This implies that minimizing the distance to the hazard with fixed maximum acceleration is equivalent to minimizing the acceleration magnitude with constant hazard location. Thus, the optimal avoidance problem solved in this section is equivalent to the

optimal avoidance problem posed at the beginning of Section 3.4. The minimum required acceleration  $a_{np,opt}$  for optimal non-passing is given below.

$$a_{np,opt} = \frac{V_o^2}{\Delta Y} \frac{\cos^2 \theta}{2} \quad (3.58)$$

For comparison, the accelerations of the stopping and non-passing constant radius turns are repeated below. The accelerations are normalized by the speed and distance  $\Delta Y$  and plotted in Fig. 3.10. The two possible values for the constant radius non-passing turn correspond to turns to the left or right.

$$a_p = \frac{V_o^2}{\Delta Y} 2 \sin(\varphi - \theta) \cos \varphi \quad (3.59)$$

$$a_{stop} = \frac{V_o^2}{\Delta Y} \frac{\cos \theta}{2} \quad (3.60)$$

$$a_{np,crt} = \frac{V_o^2}{\Delta Y} (1 \pm \sin \theta) \quad (3.61)$$

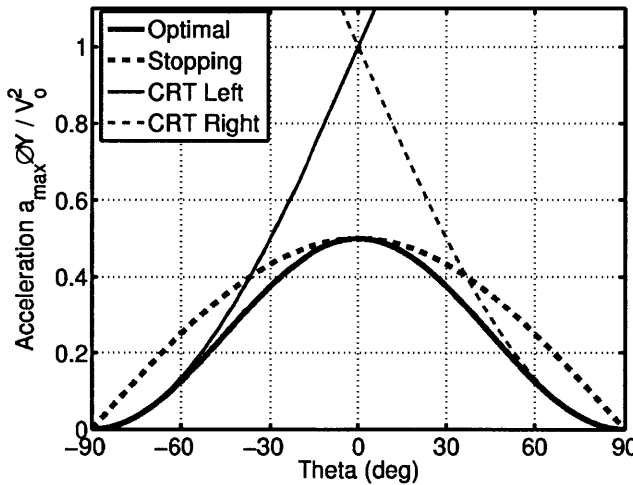


Fig. 3.10: Comparison of non-passing and stopping maneuvers.

It can be seen that the optimal non-passing maneuver requires less acceleration than straight-line stopping, except when they are equal at  $\theta=0$ . The optimal non-passing maneuver also requires less acceleration than the non-passing constant radius turns, except when  $\theta=\pm 90$  deg where the optimal maneuver and one of the constant radius turns both require zero acceleration. The optimal maneuver has its largest advantage over the

other maneuvers at  $\theta = \pm \arctan(0.75) \approx \pm 36.9$  deg, when the other maneuvers require 25% more acceleration.

### 3.4.2 Optimal passing maneuver

The optimal passing maneuver problem is posed in a manner similar to the optimal non-passing maneuver, except that the vehicle passes the edge of the hazard to either the left or right side, as in Fig. 3.11.

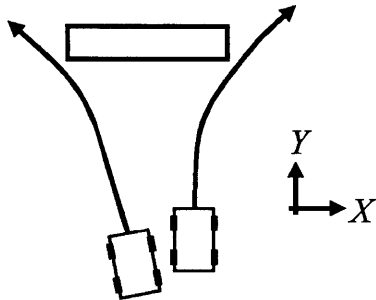


Fig. 3.11: Example passing turns.

This problem is posed by minimizing the distance from the hazard  $Y(T)$  required to reach a desired lateral offset  $X(T) = X_o + \Delta X$  (see Fig. 3.5) with no constraints on the velocity at the end time  $T$ .

$$\mathbf{u}^* = \arg \min_{\mathbf{u}} Y(T) \quad (3.62)$$

$$\dot{\mathbf{x}} = \begin{bmatrix} \dot{X} & \dot{Y} & u_1 \sin u_2 & u_1 \cos u_2 \end{bmatrix}^T \quad (3.63)$$

$$|u_1| \leq a_{\max} \quad (3.64)$$

$$X(T) = X_o + \Delta X \quad (3.65)$$

This problem has the same Hamiltonian, costate dynamics, and control laws as the non-passing maneuver, though with different boundary conditions. These shared elements are repeated below for completeness.

$$H = p_1 \dot{X} + p_2 \dot{Y} + p_3 u_1 \sin u_2 + p_4 u_1 \cos u_2 \quad (3.66)$$

$$\begin{bmatrix} p_1 \\ p_2 \\ p_3 \\ p_4 \end{bmatrix} = \begin{bmatrix} c_1 \\ c_2 \\ c_1 \tau + c_3 \\ c_2 \tau + c_4 \end{bmatrix} \quad (3.67)$$

$$u_1^* = -a_{\max} \quad (3.68)$$

$$\tan u_2^* = \frac{p_3}{p_4} = \frac{c_1\tau + c_3}{c_2\tau + c_4} \quad (3.69)$$

$$\sin u_2^* = \frac{p_3}{\sqrt{p_3^2 + p_4^2}} \quad (3.70)$$

$$\cos u_2^* = \frac{p_4}{\sqrt{p_3^2 + p_4^2}} \quad (3.71)$$

Boundary conditions are again applied to determine the values of unknown constants in the costate dynamics.

$$p_2(T) = \frac{\partial h}{\partial Y(T)} = 1 \Rightarrow c_2 = 1 \quad (3.72)$$

$$p_3(T) = \frac{\partial h}{\partial \dot{X}(T)} = 0 \Rightarrow c_3 = 0 \quad (3.73)$$

$$p_4(T) = \frac{\partial h}{\partial \dot{Y}(T)} = 0 \Rightarrow c_4 = 0 \quad (3.74)$$

The free end time condition is applied to determine the value of the final unknown constant.

$$H(T) + \frac{\partial h}{\partial T} = 0 \quad (3.75)$$

$$c_1 \dot{X}(T) + \dot{Y}(T) = 0 \quad (3.76)$$

$$c_1 = -\frac{\dot{Y}(T)}{\dot{X}(T)} \quad (3.77)$$

The control law for  $u_2^*$  is then rewritten as:

$$\tan u_2^* = -\frac{\dot{Y}(T)}{\dot{X}(T)} \quad (3.78)$$

This implies that the direction of the applied acceleration is constant in a global frame and should be perpendicular to the vehicle's velocity vector at the end time  $T$  as shown in Fig. 3.12. The optimal passing turn can thus be interpreted as an optimal non-passing turn rotated by the input angle  $u_2^*$ , also shown in Fig. 3.12. This observation will be used to simplify the computation of the angle  $u_2^*$ . Since the acceleration magnitude  $u_1^*$  and direction  $u_2^*$  are constant over the duration of the maneuver, the state trajectories can be found by integrating the dynamics as shown below.

$$\dot{X}(t) = \dot{X}_o - \sin u_2^* a_{\max} t \quad (3.79)$$

$$\dot{Y}(t) = \dot{Y}_o - \cos u_2^* a_{\max} t \quad (3.80)$$

$$X(t) = X_o + \dot{X}_o t - \frac{1}{2} \sin u_2^* a_{\max} t^2 \quad (3.81)$$

$$Y(t) = Y_o + \dot{Y}_o t - \frac{1}{2} \cos u_2^* a_{\max} t^2 \quad (3.82)$$

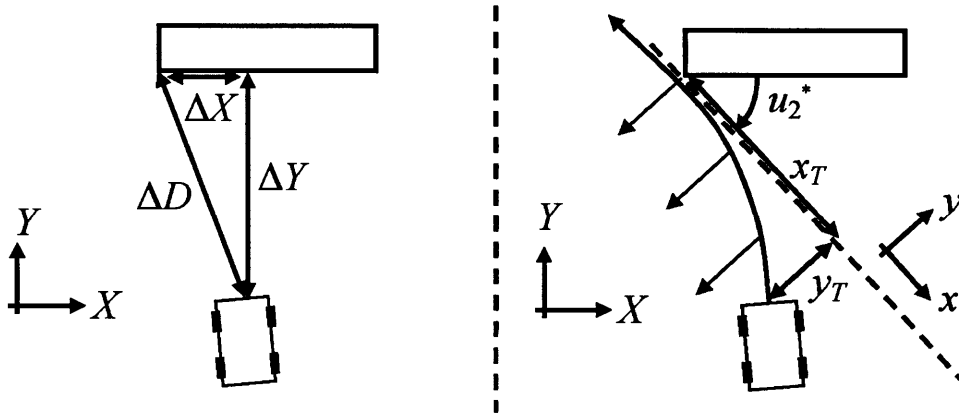


Fig. 3.12: Optimal passing turn interpreted as rotated non-passing turn.

An additional coordinate frame  $xy$  is defined that is rotated by the angle  $u_2^*$ , as shown in Fig. 3.12. The distances  $\Delta X = X(T) - X_o$  and  $\Delta Y = Y(T) - Y_o$  are expressed in frame  $xy$  as  $x_T$  and  $y_T$ , and the initial velocity components  $\dot{X}_o, \dot{Y}_o$  are expressed in frame  $xy$  as  $\dot{x}_o, \dot{y}_o$ .

$$\begin{bmatrix} x_T \\ y_T \end{bmatrix} = \begin{bmatrix} \cos u_2^* & -\sin u_2^* \\ \sin u_2^* & \cos u_2^* \end{bmatrix} \begin{bmatrix} \Delta X \\ \Delta Y \end{bmatrix} \quad (3.83)$$

$$\begin{bmatrix} \dot{x}_o \\ \dot{y}_o \end{bmatrix} = \begin{bmatrix} \cos u_2^* & -\sin u_2^* \\ \sin u_2^* & \cos u_2^* \end{bmatrix} \begin{bmatrix} \dot{X}_o \\ \dot{Y}_o \end{bmatrix} \quad (3.84)$$

The equations for the optimal non-passing maneuver can be applied to the optimal passing maneuver for the variables in frame  $xy$  to compute the ratio between distances and velocity components, the end time  $T$ , the distances  $\Delta X$  and  $\Delta Y$ , and the acceleration  $a_{\max}$ .

$$\frac{x_T}{y_T} = 2 \frac{\dot{x}_o}{\dot{y}_o} \quad (3.85)$$

$$T = \frac{\dot{y}_o}{a_{\max}} \quad (3.86)$$

$$\Delta X = \frac{\dot{y}_o}{a_{\max}} \left( \dot{X}_o - \frac{1}{2} \dot{y}_o \sin u_2^* \right) \quad (3.87)$$

$$\Delta Y = \frac{\dot{y}_o}{a_{\max}} \left( \dot{Y}_o - \frac{1}{2} \dot{y}_o \cos u_2^* \right) \quad (3.88)$$

$$a_{\max} = \frac{\dot{y}_o^2}{2y_T} \quad (3.89)$$

Similar to the optimal non-passing maneuver, the product of the acceleration  $a_{\max}$  and distance from hazard  $\Delta Y$  is a constant. Thus the optimization problem solved here is equivalent to the optimal avoidance problem posed at the beginning of Section 3.4.

If the distance  $\Delta Y$  is treated as an unknown with  $a_{\max}$  known, equations (3.84), (3.86), and (3.87) can be used to solve for the input angle  $u_2^*$  implicitly. Alternatively, if the distance  $\Delta Y$  is treated as known with  $a_{\max}$  unknown, the ratio of distances and initial velocity components in frame  $xy$  can be used to solve explicitly for the optimal input angle  $u_2^*$ , as outlined below.

First, the expressions for  $\dot{x}_o$ ,  $\dot{y}_o$ ,  $x_T$ , and  $y_T$  are simplified by using the definitions of the angles  $\theta$  and  $\varphi$  and the distance  $\Delta D$  from (3.6), (3.12), and (3.13) as shown below.

$$\begin{bmatrix} x_T \\ y_T \end{bmatrix} = \Delta D \begin{bmatrix} \sin(\varphi - u_2^*) \\ \cos(\varphi - u_2^*) \end{bmatrix} \quad (3.90)$$

$$\begin{bmatrix} \dot{x}_o \\ \dot{y}_o \end{bmatrix} = V_o \begin{bmatrix} \sin(\theta - u_2^*) \\ \cos(\theta - u_2^*) \end{bmatrix} \quad (3.91)$$

Then, the ratio between distances and velocity components in frame  $xy$  in (3.85) is re-expressed in terms of the angles  $\theta - u_2^*$  and  $\varphi - u_2^*$ . Several trigonometric identities are applied to simplify the expression.

$$\frac{x_T}{y_T} = 2 \frac{\dot{x}_o}{\dot{y}_o} \Rightarrow \tan(\varphi - u_2^*) = 2 \tan(\theta - u_2^*) \quad (3.92)$$

$$\sin(\varphi - u_2^*) \cos(\theta - u_2^*) = 2 \sin(\theta - u_2^*) \cos(\varphi - u_2^*) \quad (3.93)$$

$$\sin(\varphi - u_2^* + \theta - u_2^*) + \sin(\varphi - \theta) = 2 \sin(\varphi - u_2^* + \theta - u_2^*) - 2 \sin(\varphi - \theta) \quad (3.94)$$

$$\sin(\varphi - \theta + 2(\theta - u_2^*)) = 3 \sin(\varphi - \theta) \quad (3.95)$$

The expression in (3.95) has multiple solutions for  $u_2^*$  as shown in (3.96) and (3.97).

Note that the solution in (3.96) is discontinuous at  $\varphi - \theta = 0$ .

$$u_2^* = \theta + \frac{1}{2} (\varphi - \theta + \sin^{-1}(3 \sin(\varphi - \theta)) - \pi \operatorname{sgn}(\varphi - \theta)) \quad (3.96)$$

$$u_2^* = \theta + \frac{1}{2} (\varphi - \theta - \sin^{-1}(3 \sin(\varphi - \theta))) \quad (3.97)$$

The solutions for  $u_2^*$  in (3.96) and (3.97) are real only when the angle  $\varphi - \theta$  satisfies the constraint given below. Recall that the constant radius passing turn also has a feasibility condition, described by equation (3.20). The two solutions are plotted as  $u_2^* - \theta$  with respect to the angle  $\varphi - \theta$  in Fig. 3.13.

$$|\varphi - \theta| \leq \sin^{-1}\left(\frac{1}{3}\right) \approx 19.47 \text{ deg} \quad (3.98)$$

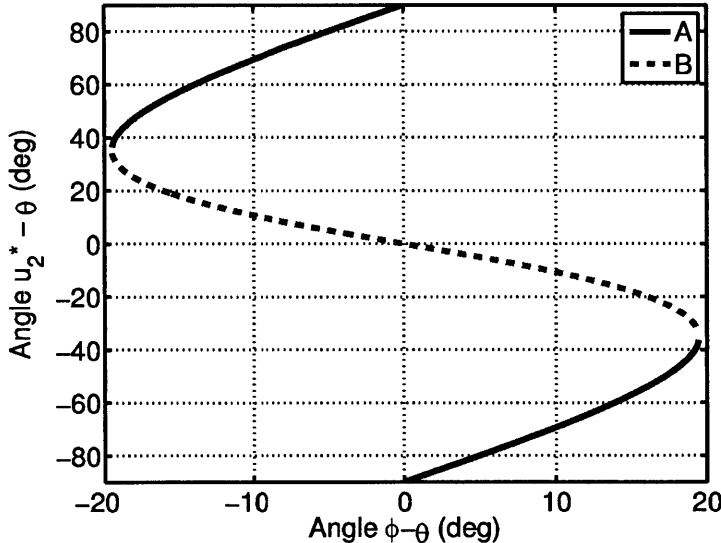


Fig. 3.13: Candidate solutions for optimal input angle  $u_2^* - \theta$  as a function of  $\varphi - \theta$ . The curve labeled "A" is given in (3.96) and the curve labeled "B" is given in (3.97).

The optimal input angle  $u_2^*$  is given by the solution of  $u_2^*$  in (3.96) or (3.97) that corresponds to the smallest value of the acceleration  $a_{\max}$ . An expression for  $a_{\max}$  in terms of  $\varphi - \theta$  and  $u_2^* - \theta$  and normalized by the speed  $V_o$  and distance  $\Delta D$  is derived from equations (3.89)-(3.91). The acceleration for each solution of  $u_2^*$  is plotted in Fig. 3.14 for the range of angles  $\varphi - \theta$  that satisfy the constraint in (3.98). For reference,

the acceleration  $a_p$  of a constant radius passing turn normalized by the speed  $V_o$  and distance  $\Delta D$  is given below and included in the plot.

$$a_{\max} = \frac{\dot{y}_o^2}{2y_T} = \frac{V_o^2}{2\Delta D} \frac{\cos^2(u_2^* - \theta)}{\cos((\varphi - \theta) + (u_2^* - \theta))} \quad (3.99)$$

$$a_p = \frac{V_o^2}{\Delta D} 2|\sin(\varphi - \theta)| \quad (3.100)$$

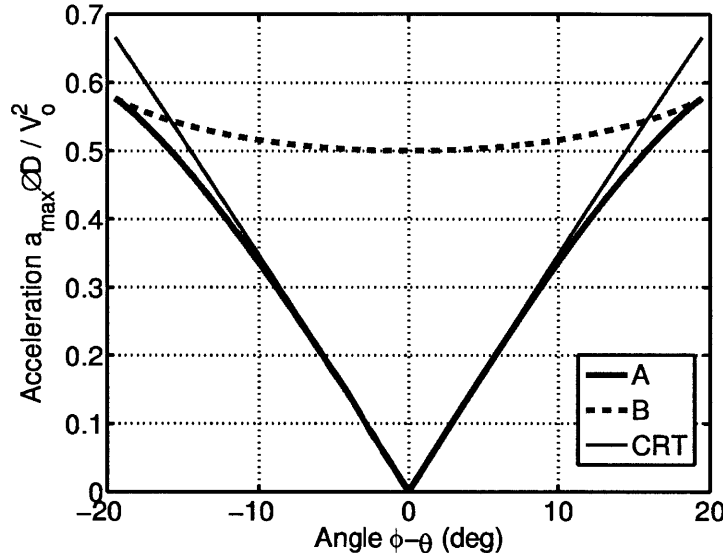


Fig. 3.14: Passing acceleration for constant radius turn (CRT) and for each candidate value of optimal angle  $u_2^*$ . The curve labeled "A" uses the solution for  $u_2^*$  from (3.96) and the curve labeled "B" uses the solution for  $u_2^*$  from (3.97).

It can be seen in Fig. 3.14 that the "A" solution of  $u_2^*$  from (3.96) requires lower acceleration than the "B" solution from (3.97). It can also be seen that the "A" solution of the optimal passing maneuver requires less acceleration than the constant radius passing turn. The advantage is most pronounced for values of the angle  $|\varphi - \theta|$  near 20 deg, with the constant radius turn requiring up to 15% more acceleration.

Three optimal passing trajectories are shown in the left subfigure of Fig. 3.15. It can be seen that the applied acceleration is perpendicular to the velocity vector at the end time  $T$  in each case. In a similar manner to the non-passing maneuver trajectories, the direction of applied force is constant in the global frame but may vary with respect to the vehicle bearing. The orientation of the applied force with respect to the vehicle bearing is shown in the right subfigure of Fig. 3.15.

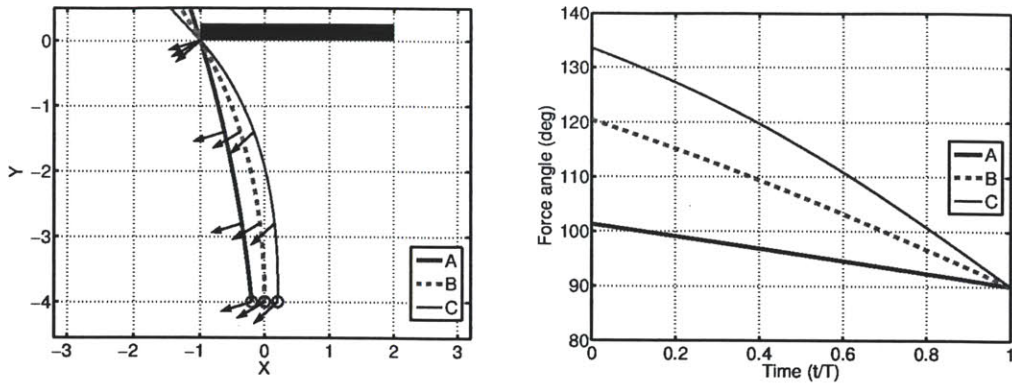


Fig. 3.15: Optimal passing trajectories and angle between acceleration and velocity vectors for three initial conditions.

$$\text{Case A: } \varphi = -11.3 \text{ deg}, \theta = -5.7 \text{ deg}, u_2^* = 73.0 \text{ deg}, a_{\max} = 0.39 \frac{V_0^2}{2\Delta Y}$$

$$\text{Case B: } \varphi = -14.0 \text{ deg}, \theta = 0.0 \text{ deg}, u_2^* = 59.6 \text{ deg}, a_{\max} = 0.94 \frac{V_0^2}{2\Delta Y}$$

$$\text{Case C: } \varphi = -16.7 \text{ deg}, \theta = 1.43 \text{ deg}, u_2^* = 47.9 \text{ deg}, a_{\max} = 1.15 \frac{V_0^2}{2\Delta Y}$$

For large values of  $\theta$  and  $\varphi$ , there is an additional feasibility constraint that is more restrictive than the constraint given in (3.98). A passing maneuver is shown in Fig. 3.16 that satisfies that constraint given in (3.98) but is not a valid avoidance maneuver because the trajectory crosses the hazard face.

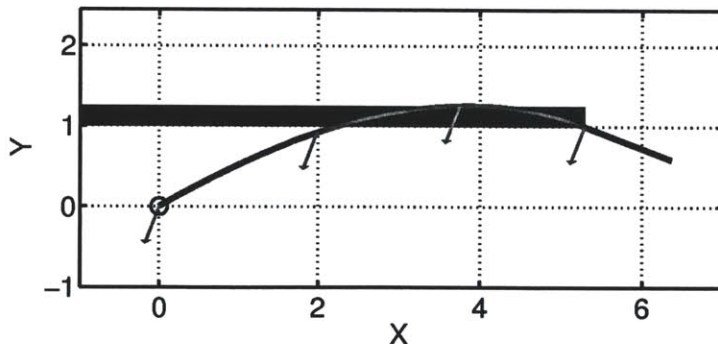


Fig. 3.16: Infeasible passing maneuver  $\varphi = 79.3$  deg,  $\theta = 60$  deg,  $u_2^* = 20.9$  deg.

The infeasibility shown in Fig. 3.16 occurs when the quantity  $\sin(\varphi - \theta)$  has the same sign as  $\sin(u_2^*)$ . A feasibility condition can be computed by setting  $u_2^* = 0$  in (3.96) and solving for the limiting angle  $\theta_{feas}$ , as shown below.

$$\theta_{feas} = -\frac{1}{2}(\varphi - \theta + \sin^{-1}(3\sin(\varphi - \theta)) - \pi \operatorname{sgn}(\varphi - \theta)) \quad (3.101)$$

The feasibility constraint in (3.98) is complemented by the constraints given below. The feasibility region corresponding to these constraints is illustrated in Fig. 3.18.

$$\varphi > \theta : \quad -\frac{\pi}{2} \leq \theta \leq \theta_{feas} \quad (3.102)$$

$$\varphi < \theta : \quad \theta_{feas} \leq \theta \leq \frac{\pi}{2} \quad (3.103)$$

It was shown in Fig. 3.14 that the optimal passing maneuver requires less acceleration than the constant radius passing turn, provided that the optimal passing maneuver is feasible. To compare the acceleration required for optimal passing and optimal non-passing turns, the accelerations were normalized by the distance  $\Delta Y$  and velocity component  $\dot{Y}_o$  and plotted in Fig. 3.17 for several values of the initial heading angle  $\theta$ . It can be seen that the passing maneuver requires less acceleration for small values of the angle  $\varphi - \theta$ , though it depends on the heading angle  $\theta$ . The angles at which the maneuvers in Fig. 3.17 have equal acceleration are given in Table 3.1.

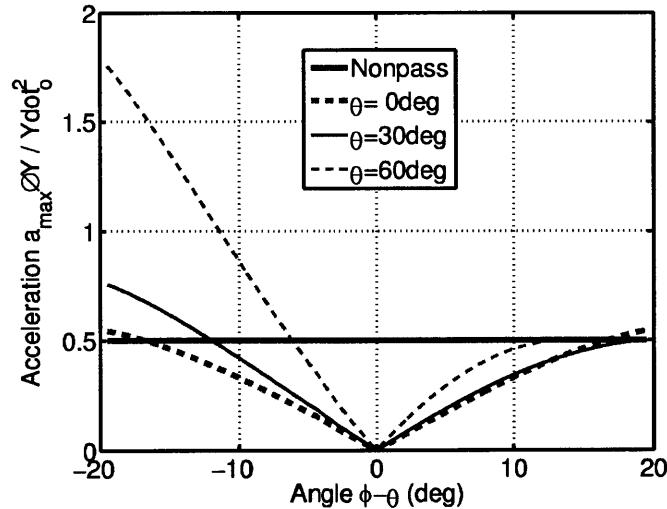


Fig. 3.17: Acceleration of optimal non-passing and passing maneuver for several values of the heading angle  $\theta$ .

$\theta$	Minimum $\varphi-\theta$	Maximum $\varphi-\theta$
0 deg	-16.7 deg	16.7 deg
30 deg	-11.9 deg	19.4 deg
60 deg	-6.15 deg	13.9 deg

Table 3.1: Angles for which optimal passing maneuvers in Fig. 3.17 have identical acceleration as optimal non-passing maneuver.

The computations that generated Fig. 3.17 and Table 3.1 were repeated to compute the set of angles  $\varphi-\theta$  for which the optimal passing maneuver is equivalent to the optimal non-passing maneuver for a range of values of the angle  $\theta$ . This set of angles is plotted in Fig. 3.18 along with the range of angles for which optimal passing is feasible.

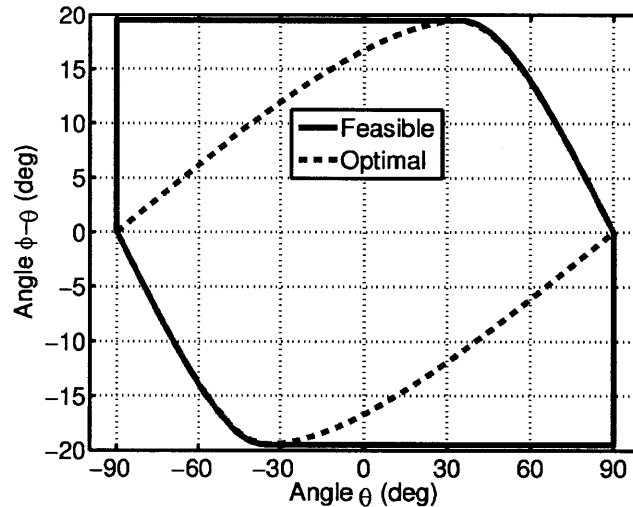


Fig. 3.18: Range of angles  $\varphi-\theta$  for which the optimal passing maneuver is feasible (Feasible) and requires less acceleration than optimal non-passing (Optimal).

### 3.4.3 Discussion

Two optimal avoidance maneuvers were derived in the previous sections. Each maneuver has a control law involving a constant magnitude acceleration applied in a constant direction in the global frame. The optimal non-passing maneuver was shown to require less acceleration than straight-line stopping and constant radius non-passing turns. The optimal passing maneuver was shown to require less acceleration than a constant radius passing turn.

It should be noted that the worst-case acceleration of the geometric maneuvers was within 25% of the optimal maneuvers, and in several cases the accelerations were equal. This implies that the geometric maneuvers may provide a useful suboptimal approximation of the optimal maneuvers.

A condition was derived to compare the acceleration required by the optimal passing maneuver and the optimal non-passing maneuver. This condition depends on the angles  $\theta$  and  $\varphi-\theta$ . It is important to note that the condition does not depend on vehicle speed or the distance to the hazard. An interpretation of this condition is that for a given heading angle  $\theta$ , lines can be projected from extrema of a hazard using the heading  $\theta$  and the corresponding angles  $\varphi-\theta$  from Fig. 3.18, as shown in Fig. 3.19. These lines represent the boundary between initial conditions for which the passing and non-passing maneuvers require less acceleration. A triangle is formed, inside of which the non-passing maneuver requires less acceleration, such as vehicle *A*. On either side of the triangle, a passing maneuver to that side requires less acceleration, such as vehicles *B* and *C*.

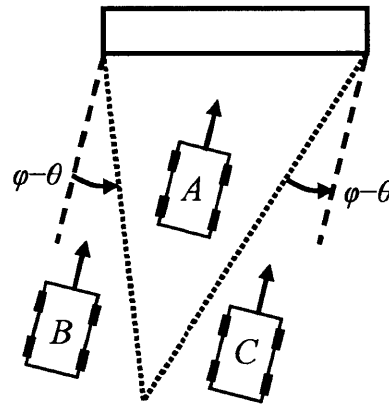


Fig. 3.19: Interpretation of conditions on angle  $\varphi-\theta$  for which optimal passing and optimal non-passing require equal acceleration.

The single hazard avoidance maneuvers considered in this chapter were special cases of the optimal control problem with boundary conditions that caused the optimal control law for  $u_2^*$  to be constant. This allowed the maneuvers to be solved explicitly. The optimal control analysis can be used to solve for other types of optimal maneuvers for the point mass with bounded acceleration magnitude. For example, the optimal passing maneuver can be converted into an optimal lane change by fixing the terminal lateral

velocity  $\dot{X}(T)$  to zero. A minimum time maneuver can be solved as well, using the same Hamiltonian, costate dynamics, and control law with different end conditions. Changing boundary conditions changes the constants in the costate variables, which may cause the control law for  $u_2$  (repeated below) to vary with time. Maneuvers with time varying optimal control laws are an interesting subject for future work.

$$\tan u_2^* = \frac{c_1\tau + c_3}{c_2\tau + c_4} \quad (3.104)$$

### 3.5 Conclusions

In this chapter, optimal maneuvers for avoiding a single hazard were derived for a point mass with bounded acceleration magnitude. The optimal maneuvers were compared to geometric avoidance maneuvers and shown to require up to 25% less acceleration. These single hazard avoidance maneuvers can be applied sequentially to avoid multiple hazards when the hazards are far enough apart. A condition was derived to identify the range of angles  $\theta$  and  $\varphi - \theta$  for which the optimal passing maneuver requires less acceleration than the optimal non-passing maneuver.

The acceleration constraint acting on the point mass is analogous to the tire friction circle constraint, which is important in vehicle dynamics. In the next chapter, an analogy is drawn between the dynamics of a nonlinear bicycle and a point mass, and a connection is made between a friction circle constraint and an acceleration circle constraint.

## **CHAPTER 4: CONTROL OF NONLINEAR BICYCLE**

This chapter presents a trajectory-tracking controller that allows the optimal avoidance trajectories derived in Chapter 3 to be tracked by the nonlinear bicycle model given in Chapter 2. In Section 4.1, a flatness-based trajectory tracking controller is presented for the nonlinear bicycle model that maps the bicycle dynamics into a point mass located at the front center of oscillation with an additional degree of freedom corresponding to forced yaw dynamics. In Section 4.2, the structure and stability of the yaw dynamics are assessed analytically and in simulation. Discussion of the results is given in Section 4.3, followed by conclusions in Section 4.4.

### **4.1 Flatness of nonlinear bicycle model**

As discussed in Chapter 1, there have been several approaches to applying flatness-based control to bicycle dynamics. The position and velocity of the bicycle's rear center of oscillation have been identified as flat outputs in previous work [28, 64, 75, 5]. The body-fixed acceleration of the front center of oscillation has been controlled as well [1], though the position of the front center of oscillation has not been considered as a flat output to the author's knowledge. It will be shown that the position of the front center of oscillation is an advantageous choice of flat output as it can be controlled to track trajectories with finite acceleration, whereas the position of the rear center of oscillation requires an additional degree of smoothness in reference trajectories [28, 64].

For reference, the centers of oscillation for the bicycle model from Chapter 2 with mass  $m$  and yaw inertia  $I_{zz}$  are illustrated in Fig. 4.1. The distance from the c.g. to the front center of oscillation is defined as  $l_{co}$  as shown below.

$$l_{co} = \frac{I_{zz}}{mx_r} \quad (4.1)$$

The front center of oscillation is marked as point  $p$  with vectors for position  $\vec{r}_p$ , velocity  $\vec{v}_p$ , and acceleration  $\vec{a}_p$  given below. The fixed frame position components of point  $p$  are given as  $X_p$  and  $Y_p$ .

$$\vec{r}_p = \vec{r}_c + l_{co}\vec{i}_b = X_p\vec{i} + Y_p\vec{j} \quad (4.2)$$

$$\vec{v}_p = \vec{v}_c + (\dot{\psi}\vec{k}) \times (l_{co}\vec{i}_b) = \dot{X}_p\vec{i} + \dot{Y}_p\vec{j} \quad (4.3)$$

$$\vec{a}_p = \vec{a}_c + (\ddot{\psi}\vec{k}) \times (l_{co}\vec{i}_b) + (\dot{\psi}\vec{k}) \times ((\dot{\psi}\vec{k}) \times (l_{co}\vec{i}_b)) = \ddot{X}_p\vec{i} + \ddot{Y}_p\vec{j} \quad (4.4)$$

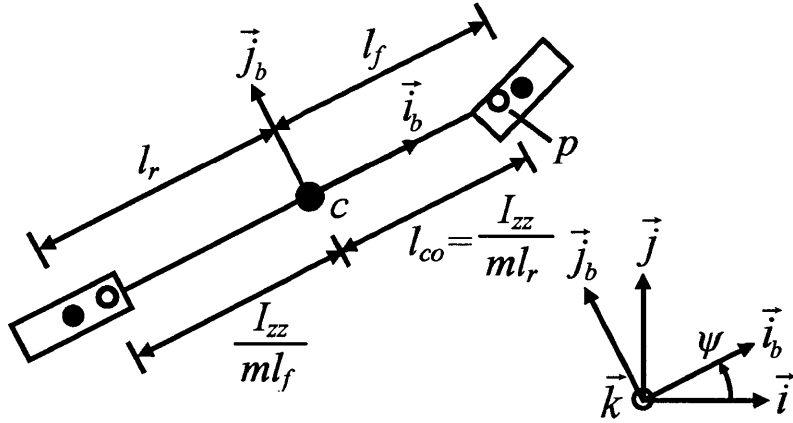


Fig. 4.1: Nonlinear bicycle model with wheel centers marked as solid circles and centers of oscillation as hollow circles. The front center of oscillation is marked as point  $p$ .

The expressions for  $\vec{v}_p$  and  $\vec{a}_p$  are simplified as shown below.

$$\vec{v}_p = \vec{v}_c + l_{co}\dot{\psi}\vec{j}_b \quad (4.5)$$

$$\vec{a}_p = \vec{a}_c - l_{co}\dot{\psi}^2\vec{i}_b + l_{co}\ddot{\psi}\vec{j}_b \quad (4.6)$$

For reference, the dynamics of point  $c$  from (2.17)-(2.18) are repeated below.

$$m\vec{a}_c = (F_{xf} \cos \delta - F_{yf} \sin \delta + F_{xr})\vec{i}_b + (F_{xf} \sin \delta + F_{yf} \cos \delta + F_{yr})\vec{j}_b \quad (4.7)$$

$$I_{zz}\ddot{\psi} = x_f F_{xf} \sin \delta + x_f F_{yf} \cos \delta - x_r F_{yr} \quad (4.8)$$

The dynamics of point  $c$  are used to compute the dynamics of point  $p$  in the body-fixed frame. It can be seen that the rear lateral force  $F_{yr}$  is eliminated from the expression for  $m\vec{a}_p$ , and a term proportional to  $\dot{\psi}^2$  is added.

$$m\vec{a}_p = \left( F_{xf} \cos \delta - F_{yf} \sin \delta + F_{xr} - ml_{co} \dot{\psi}^2 \right) \vec{i}_b + \left( 1 + \frac{l_f}{l_r} \right) \left( F_{xf} \sin \delta + F_{yf} \cos \delta \right) \vec{j}_b \quad (4.9)$$

Since the tire forces  $F_{xf}$ ,  $F_{xr}$ , and  $F_{yf}$  are controllable with wheel torques  $\tau_f$  and  $\tau_r$  and the front steering angle  $\delta$ , the dynamics of point  $p$  are linearizable with the definition of intermediate inputs  $u_{ib}$ ,  $u_{jb}$ , and  $u_3$ :

$$u_{ib} = F_{xf} \cos \delta - F_{yf} \sin \delta + F_{xr} \quad (4.10)$$

$$u_{jb} = F_{xf} \sin \delta + F_{yf} \cos \delta \quad (4.11)$$

$$u_3 = \frac{F_{xr}}{\mu F_{zr}} \quad (4.12)$$

the projection of the fixed frame acceleration components  $\ddot{X}_p$  and  $\ddot{Y}_p$  into the body-fixed frame;

$$m\vec{a}_p = (\ddot{X}_p \cos \psi + \ddot{Y}_p \sin \psi) \vec{i}_b + (-\ddot{X}_p \sin \psi + \ddot{Y}_p \cos \psi) \vec{j}_b \quad (4.13)$$

and dynamic feedback

$$u_{ib} = m(l_{co} \dot{\psi}^2 + u_1(t) \cos \psi + u_2(t) \sin \psi) \quad (4.14)$$

$$u_{jb} = \frac{ml_r}{l_f + l_r} (-u_1(t) \sin \psi + u_2(t) \cos \psi) \quad (4.15)$$

where  $u_1(t)$  and  $u_2(t)$  are functions of time representing the desired fixed frame acceleration. This feedback partitions the bicycle dynamics into a flat subsystem based on the front center of oscillation and a subsystem based on the yaw dynamics as shown below.

$$\ddot{X}_p = u_1(t) \quad (4.16)$$

$$\ddot{Y}_p = u_2(t) \quad (4.17)$$

$$\ddot{\psi} = c_1 \left( -\frac{u_1(t)}{g} \sin \psi + \frac{u_2(t)}{g} \cos \psi - f_{yr}(\alpha_r) \sqrt{1 - u_3^2} \right) \quad (4.18)$$

$$c_1 = \frac{F_{xr}}{ml_{co}} \quad (4.19)$$

where  $g$  is the gravitational acceleration constant.

The flat subsystem depends on inputs  $u_1$  and  $u_2$ , while the yaw dynamics depend on inputs  $u_1$ ,  $u_2$ , and  $u_3$ . A control law for steering angle  $\delta$  and wheel torques  $\tau_f$  and  $\tau_r$  to implement the feedback controller described above is detailed in Appendix X. Note that actuator limits, particularly the limit on the maximum steering angle, limit the range of states for which this control law can be applied. The effect of actuator limits will be studied in simulation in the following sections.

It can be shown that the front friction circle constraint maps to a constraint on the acceleration of the front center of oscillation. First, the front friction circle constraint is expressed in terms of the inputs  $u_{ib}$ ,  $u_{jb}$ , and  $u_3$ .

$$\sqrt{F_{xf}^2 + F_{yf}^2} \leq \mu F_{zf} \rightarrow \sqrt{(u_{ib} - \mu F_{zx} u_3)^2 + u_{jb}^2} \leq \mu F_{zf} \quad (4.20)$$

A control law for  $u_3$  that maps the front friction circle constraint exactly into a constraint on acceleration magnitude is given below. This acceleration constraint matches the constraint on point mass dynamics considered in the previous chapter. This demonstrates the applicability of the point mass model considered in the previous chapter to the nonlinear bicycle model.

$$u_3 = \frac{1}{\mu} \left( \frac{1}{c_1} \dot{\psi}^2 + \frac{l_f}{l_f + l_r} \left( \frac{u_1(t)}{g} \cos \psi + \frac{u_2(t)}{g} \sin \psi \right) \right) \quad (4.21)$$

$$\sqrt{F_{xf}^2 + F_{yf}^2} \leq \mu F_{zf} \rightarrow \sqrt{u_1(t)^2 + u_2(t)^2} \leq \mu g \quad (4.22)$$

It can be seen that the inputs to the flat subsystem can be recovered from the second derivative of the vehicle position, while the flat systems based on the rear center of oscillation require the third derivative of position to recover the inputs [28, 64]. This implies that the flat subsystem described above can track trajectories with fewer smoothness requirements than a system based on the rear center of oscillation. It should be noted, however, that the behavior of the yaw dynamics must be considered when controlling the front center of oscillation. The structure and stability of the yaw dynamics are evaluated in the following section.

## 4.2 Analysis of Yaw Dynamics

In this section, the structure and stability of the bicycle model yaw dynamics are evaluated when subject to the flatness-based controller described in the previous section.

Previous work by Ackermann provided a linear stability analysis of bicycle yaw dynamics when subject to control of the body-fixed acceleration at the front center of oscillation. This analysis indicated that the bicycle yaw dynamics are a stable second-order system with damping inversely proportional to vehicle speed [1]. The applicability of this linear analysis is limited, however, to the range of rear slip angles for which the rear lateral tire force  $F_{yr}(\alpha_r, u_3)$  is approximately linear. The work presented here includes a nonlinear stability analysis that is applicable to a wider range of conditions than the previous work.

#### 4.2.1 Structure of yaw dynamics

The flatness-based controller in the previous section controls two degrees of freedom of the bicycle model, corresponding to the position of the front center of oscillation. The yaw dynamics, given in (4.18), represent an additional degree of freedom of the system. These dynamics depend on the rear lateral tire force  $F_{yr}(\alpha_r, u_3)$  and the inputs  $u_1(t)$  and  $u_2(t)$ .

Several state transformations are introduced below that reveal the structure of the yaw dynamics and enable a nonlinear stability analysis. It is assumed that the flatness-based controller tracks a desired reference trajectory with fixed frame position  $\vec{r}_p(t)$ , velocity  $\vec{v}_p(t)$ , and acceleration  $\vec{a}_p(t)$ . The speed  $v_p(t)$  and heading angle  $\theta_p(t)$  of the reference trajectory are computed from the components of  $\vec{v}_p(t)$  as

$$v_p(t) = \|\vec{v}_p(t)\| = \sqrt{\dot{X}_p(t)^2 + \dot{Y}_p(t)^2} \quad (4.23)$$

$$\theta_p(t) = \tan^{-1}\left(\frac{\dot{Y}_p(t)}{\dot{X}_p(t)}\right) \quad (4.24)$$

and illustrated in Fig. 4.2. The inverse relationship between fixed frame velocity components and  $v_p(t)$  and  $\theta_p(t)$  is given as

$$\dot{X}_p(t) = v_p(t) \cos \theta_p(t) \quad (4.25)$$

$$\dot{Y}_p(t) = v_p(t) \sin \theta_p(t) \quad (4.26)$$

and are differentiated to yield the following:

$$\ddot{X}_p(t) = \dot{v}_p(t) \cos \theta_p(t) - v_p(t) \dot{\theta}_p(t) \sin \theta_p(t) \quad (4.27)$$

$$\ddot{Y}_p(t) = \dot{v}_p(t)\sin\theta_p(t) + v_p(t)\dot{\theta}_p(t)\cos\theta_p(t) \quad (4.28)$$

The slip angle  $\beta_p(\psi, t)$  at the front center of oscillation, shown in Fig. 4.2, is defined as

$$\beta_p(\psi, t) = \theta_p(t) - \psi \quad (4.29)$$

and the longitudinal and lateral path accelerations  $\dot{v}_p(t)$  and  $v_p(t)\dot{\theta}_p(t)$  are non-dimensionalized as:

$$u_v(t) = \frac{\dot{v}_p(t)}{g} \quad (4.30)$$

$$u_\theta(t) = \frac{v_p(t)\dot{\theta}_p(t)}{g} \quad (4.31)$$

With these definitions, the yaw dynamics from (4.18) are re-expressed in terms of the slip angles  $\beta_p$  and  $\alpha_r$ , the input  $u_3$ , and time  $t$  as follows:

$$\ddot{\beta}_p(\beta_p, \alpha_r, u_3, t) = \ddot{\theta}_p(t) - c_1 \left[ u_v(t) \sin \beta_p + u_\theta(t) \cos \beta_p - f_{yr}(\alpha_r) \sqrt{1-u_3^2} \right] \quad (4.32)$$

An expression for the rear slip angle  $\alpha_r$  was given in (2.23). For this system with the differential flatness controller, an equivalent expression for  $\alpha_r$  in terms of  $\psi$ ,  $\dot{\psi}$ , and  $t$  is given as follows:

$$\alpha_r(\psi, \dot{\psi}, t) = \tan^{-1} \left( \frac{v_p(t) \sin \beta_p(\psi, t) - L \dot{\psi}}{v_p(t) \cos \beta_p(\psi, t)} \right) \quad (4.33)$$

$$L = l_{co} + l_r \quad (4.34)$$

where  $L$  is the distance from the rear tire to the front center of oscillation.

To simplify the expression for  $\alpha_r(\psi, \dot{\psi}, t)$ , the angle  $\gamma$  is defined as the difference between the body slip angle and rear tire slip angle as

$$\gamma(\psi, \dot{\psi}, t) = \beta_p(\psi, t) - \alpha_r(\psi, \dot{\psi}, t) \quad (4.35)$$

and illustrated in Fig. 4.2. Some identities for  $\gamma$  are given below in terms of different variables. Note that  $\gamma$  is small when the scaled yaw rate  $L \dot{\psi}$  is small relative to the desired speed  $v_p(t)$ .

$$\gamma(\beta_p, \dot{\psi}, t) = \tan^{-1} \left( \frac{L \dot{\psi} \cos \beta_p}{v_p(t) - L \dot{\psi} \sin \beta_p} \right) \quad (4.36)$$

$$\gamma(\alpha_r, \dot{\psi}, t) = \sin^{-1} \left( \frac{L \dot{\psi} \cos \alpha_r}{v_p(t)} \right) \quad (4.37)$$

$$v_p(t) \cos \gamma(\beta_p, \dot{\psi}, t) = v_r(\beta_p, \dot{\psi}, t) + L \dot{\psi} \sin(\beta_p - \gamma(\beta_p, \dot{\psi}, t)) \quad (4.38)$$

$$v_r(\beta_p, \dot{\psi}, t) \cos \gamma(\beta_p, \dot{\psi}, t) = v_p(t) - L \dot{\psi} \sin \beta_p \quad (4.39)$$

where  $v_r(\beta_p, \dot{\psi}, t)$  is the speed at the rear wheel and is computed as follows:

$$v_r(\beta_p, \dot{\psi}, t) = \sqrt{(v_p(t) \sin \beta_p - L \dot{\psi})^2 + (v_p(t) \cos \beta_p)^2} \quad (4.40)$$

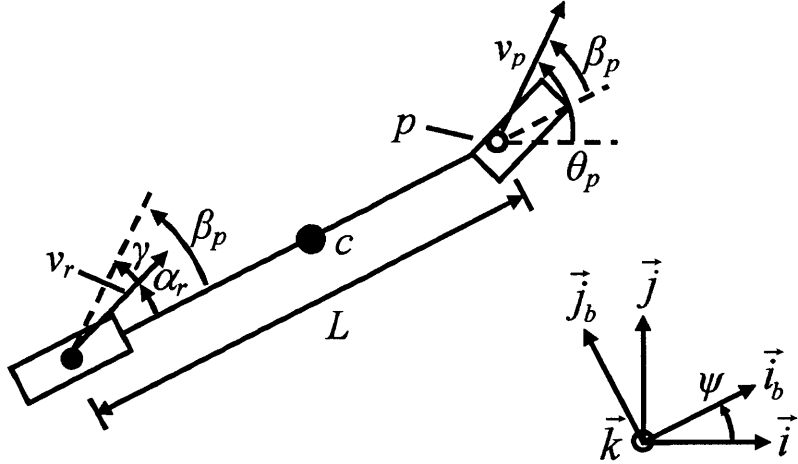


Fig. 4.2: Nonlinear bicycle model with front center of oscillation and rear wheel marked.

The speed  $v_p$ , heading angle  $\theta_p$ , and slip angle  $\beta_p$  at the front center of oscillation are shown. At the rear wheel, the speed  $v_r$  and slip angle  $\alpha_r$  are shown, as well as the angle  $\gamma$ .

Noting that the quantity  $(\dot{\theta}_p(t) - \dot{\beta}_p)$  can be substituted for the yaw rate  $\dot{\psi}$ , the yaw dynamics can be expressed as a second-order system in terms of  $(\beta_p, \dot{\beta}_p)$  as follows:

$$\ddot{\beta}_p(\beta_p, \dot{\beta}_p, u_3, t) = \ddot{\theta}_p(t) - c_1(u_v(t) \sin \beta_p + u_\theta(t) \cos \beta_p) + c_1 f_{yr}(\beta_p - \gamma(\beta_p, \dot{\beta}_p, t)) \sqrt{1 - u_3^2} \quad (4.41)$$

As a second order system of  $(\beta_p, \dot{\beta}_p)$ , terms dependent on  $\beta_p$  are analogous to potential forces, and terms dependent on  $\dot{\beta}_p$  are analogous to damping forces. With the yaw dynamics in this form, the damping term is nested within the nonlinear functions  $f_{yr}(\cdot)$  and  $\gamma(\cdot)$ . A candidate Lyapunov function that is inspired by "energy" of the yaw dynamics is given below.

$$V = \frac{1}{2} \dot{\beta}_p^2 + \int g(\beta_p) d\beta_p \quad (4.42)$$

Alternatively, the yaw dynamics can be expressed in terms of  $(\alpha_r, \dot{\beta}_p)$ . The state transformation from  $(\psi, \dot{\psi})$  to  $(\alpha_r, \dot{\beta}_p)$  is a valid diffeomorphism provided that the following condition is met:

$$\det \begin{bmatrix} \frac{\partial \alpha_r}{\partial \psi} & \frac{\partial \alpha_r}{\partial \dot{\psi}} \\ \frac{\partial \dot{\beta}_p}{\partial \psi} & \frac{\partial \dot{\beta}_p}{\partial \dot{\psi}} \end{bmatrix} = \frac{\partial \alpha_r}{\partial \psi} \frac{\partial \dot{\beta}_p}{\partial \dot{\psi}} - \frac{\partial \alpha_r}{\partial \dot{\psi}} \frac{\partial \dot{\beta}_p}{\partial \psi} \neq 0 \quad (4.43)$$

With the following values for the partial derivatives:

$$\frac{\partial \alpha_r}{\partial \psi} = -\frac{v_p(t) \cos \gamma(\psi, \dot{\psi}, t)}{v_r(\psi, \dot{\psi}, t)} \quad (4.44)$$

$$\frac{\partial \dot{\beta}_p}{\partial \dot{\psi}} = -1 \quad (4.45)$$

$$\frac{\partial \dot{\beta}_p}{\partial \psi} = 0 \quad (4.46)$$

the condition from (4.43) is restated as

$$\frac{v_p(t) \cos \gamma(\psi, \dot{\psi}, t)}{v_r(\psi, \dot{\psi}, t)} \neq 0 \quad (4.47)$$

If  $v_p(t) \neq 0$ , the condition from (4.43) is equivalent to the following:

$$\cos \gamma(\psi, \dot{\psi}, t) \neq 0 \quad (4.48)$$

$$|\sin \gamma(\psi, \dot{\psi}, t)| < 1 \Rightarrow -\pi/2 \leq \gamma(\psi, \dot{\psi}, t) \leq \pi/2 \quad (4.49)$$

$$\left| \frac{L \dot{\psi} \cos \alpha_r(\psi, \dot{\psi}, t)}{v_p(t)} \right| < 1 \quad (4.50)$$

which can be conservatively approximated as

$$\left| \frac{L \dot{\psi}}{v_p(t)} \right| < 1 \Rightarrow |\dot{\psi}| < \frac{v_p(t)}{L} \quad (4.51)$$

Thus the state transformation from  $\psi, \dot{\psi}$  to  $\alpha_r, \dot{\beta}_p$  is a valid diffeomorphism provided that the scaled yaw rate is not too large.

With this state transformation, the quantities  $\gamma$  and  $v_r$  are then expressed in terms of  $\alpha_r$ ,  $\dot{\beta}_p$ , and  $t$  as

$$\gamma(\alpha_r, \dot{\beta}_p, t) = \sin^{-1} \left( \frac{L(\dot{\theta}_p(t) - \dot{\beta}_p) \cos \alpha_r}{v_p(t)} \right) \quad (4.52)$$

$$\beta_p(\alpha_r, \dot{\beta}_p, t) = \alpha_r + \gamma(\alpha_r, \dot{\beta}_p, t) \quad (4.53)$$

$$v_r(\alpha_r, \dot{\beta}_p, t) = v_p(t) \cos \gamma(\alpha_r, \dot{\beta}_p, t) - L(\dot{\theta}_p(t) - \dot{\beta}_p) \sin \alpha_r \quad (4.54)$$

The yaw dynamics  $\ddot{\psi}$  are partitioned into autonomous and non-autonomous terms as

$$\ddot{\psi} = f_1(\alpha_r, u_3) + f_2(\alpha_r, \dot{\beta}_p, t) \quad (4.55)$$

$$f_1(\alpha_r, u_3) = -c_1 f_{yr}(\alpha_r) \sqrt{1 - u_3^2} \quad (4.56)$$

$$f_2(\alpha_r, \dot{\beta}_p, t) = c_1(u_v(t) \sin \beta_p(\alpha_r, \dot{\beta}_p, t) + u_\theta(t) \cos \beta_p(\alpha_r, \dot{\beta}_p, t)) \quad (4.57)$$

The time derivative  $\dot{\gamma}(\alpha_r, \dot{\beta}_p, u_3, t)$  is likewise partitioned into autonomous and non-autonomous terms as

$$\dot{\gamma}(\alpha_r, \dot{\beta}_p, u_3, t) = \frac{f_3(\alpha_r, u_3) + f_4(\alpha_r, \dot{\beta}_p, t)}{v_r(\alpha_r, \dot{\beta}_p, t)} \quad (4.58)$$

$$f_3(\alpha_r, u_3) = L f_1(\alpha_r, u_3) \cos \alpha_r \quad (4.59)$$

$$f_4(\alpha_r, \dot{\beta}_p, t) = L f_2(\alpha_r, \dot{\beta}_p, t) \cos \alpha_r + L(\dot{\beta}_p - \dot{\theta}_p(t)) \dot{\beta}_p \sin \alpha_r - g u_v(t) \sin \gamma(\alpha_r, \dot{\beta}_p, t) \quad (4.60)$$

so that the dynamics of  $\alpha_r$  and  $\dot{\beta}_p$  can be given as

$$\dot{\alpha}_r(\alpha_r, \dot{\beta}_p, u_3, t) = \dot{\beta}_p - \frac{f_3(\alpha_r, u_3) + f_4(\alpha_r, \dot{\beta}_p, t)}{v_r(\alpha_r, \dot{\beta}_p, t)} \quad (4.61)$$

$$\ddot{\beta}_p(\alpha_r, \dot{\beta}_p, u_3, t) = -f_1(\alpha_r, u_3) - f_2(\alpha_r, \dot{\beta}_p, t) + \ddot{\theta}_p(t) \quad (4.62)$$

With this parameterization in terms of  $(\alpha_r, \dot{\beta}_p)$ , the yaw dynamics are similar to a Liénard system in the Liénard plane, described in (4.63) with states  $x$  and  $y$  [34, 16].

$$\begin{bmatrix} \dot{x} \\ \dot{y} \end{bmatrix} = \begin{bmatrix} y - q(x) \\ -p(x) \end{bmatrix} \quad (4.63)$$

Many nonlinear oscillators can be expressed as Liénard systems, including the Van der Pol oscillator. There are also useful theorems and candidate Lyapunov functions that can be applied to analyze the stability of Liénard systems. An additional property of Liénard systems is that they can be expressed as second order systems of the variable  $x$ , as shown below. In this form the system resembles a second-order mechanical system, with  $q'(x)$  as the derivative of  $q(x)$  resembling a damping coefficient, and the function  $p(x)$  resembling a potential force term.

$$\ddot{x} + q'(x)\dot{x} + p(x) = 0 \quad (4.64)$$

A candidate Lyapunov function for the Liénard system from (4.63) is given below [34, 16]. Recalling that the function  $p(x)$  resembles the potential force of the system, it can be seen that the function given below resembles an energy function with terms for kinetic and potential energy.

$$V = \frac{1}{2}y^2 + \int_0^x p(s)ds \quad (4.65)$$

In this section, state transformations from  $(\psi, \dot{\psi})$  to  $(\beta_p, \dot{\beta}_p)$  and  $(\alpha_r, \dot{\beta}_p)$  were introduced to show structure in the yaw dynamics. When expressed in terms of  $(\beta_p, \dot{\beta}_p)$  as in (4.41), the yaw dynamics resemble a second order system with nonlinear potential force and damping terms. When expressed in terms of  $(\alpha_r, \dot{\beta}_p)$  as in (4.61)-(4.62), the yaw dynamics resemble a Liénard system. This insight into the structure of the dynamics inspires several candidate Lyapunov functions, which are used in a stability analysis in the following sections.

#### 4.2.2 Stability of unforced yaw dynamics

In this section, the stability of the yaw dynamics are assessed when tracking a straight-line trajectory at constant speed with a constant  $u_3$  input ( $u_v = u_\theta = \dot{u}_3 = 0$ ) and  $|u_3| < 1$ . The dynamics are simplified according to these forcing conditions, and the location and stability of equilibrium points are found. System stability is evaluated using contraction theory and several Lyapunov functions, and stability claims are verified with simulation results.

With the forcing conditions given above, the yaw dynamics can be expressed in terms of  $(\beta_p, \dot{\beta}_p)$  as

$$\ddot{\beta}_p(\beta_p, \dot{\beta}_p) = c_2 f_{yr}(\beta_p - \gamma(\beta_p, \dot{\beta}_p)) \quad (4.66)$$

with constant  $c_2$  defined as

$$c_2 = c_1 \sqrt{1 - u_3^2} \quad (4.67)$$

and the angle  $\gamma$  and rear speed  $v_r$  computed as:

$$\gamma(\beta_p, \dot{\beta}_p) = \tan^{-1} \left( \frac{-L\dot{\beta}_p \cos \beta_p}{v_p + L\dot{\beta}_p \sin \beta_p} \right) \quad (4.68)$$

$$v_r(\beta_p, \dot{\beta}_p) = \sqrt{(v_p \sin \beta_p + L\dot{\beta}_p)^2 + (v_p \cos \beta_p)^2} \quad (4.69)$$

Likewise, the functions  $f_2$  and  $f_4$  are simplified as

$$f_2 = 0 \quad (4.70)$$

$$f_4(\alpha_r, \dot{\beta}_p) = L\dot{\beta}_p^2 \sin \alpha_r \quad (4.71)$$

so that the dynamics are expressed in terms of  $(\alpha_r, \dot{\beta}_p)$  as:

$$\dot{\alpha}_r(\alpha_r, \dot{\beta}_p) = \dot{\beta}_p + L \frac{c_2 f_{yr}(\alpha_r) \cos \alpha_r - \dot{\beta}_p^2 \sin \alpha_r}{v_r(\alpha_r, \dot{\beta}_p)} \quad (4.72)$$

$$\ddot{\beta}_p(\alpha_r) = c_2 f_{yr}(\alpha_r) \quad (4.73)$$

with the angle  $\gamma$  and rear speed  $v_r$  computed as:

$$\gamma(\alpha_r, \dot{\beta}_p) = \sin^{-1} \left( -\frac{L\dot{\beta}_p \cos \alpha_r}{v_p} \right) \quad (4.74)$$

$$v_r(\alpha_r, \dot{\beta}_p) = v_p \cos \gamma(\alpha_r, \dot{\beta}_p) + L\dot{\beta}_p \sin \alpha_r \quad (4.75)$$

The locations of equilibrium points  $(\beta_o, \dot{\beta}_o)$  and  $(\alpha_o, \dot{\beta}_o)$  are computed in terms of states  $(\beta_p, \dot{\beta}_p)$  using the following conditions:

$$\dot{\beta}_p = 0 \Rightarrow \dot{\beta}_o = 0 \quad (4.76)$$

$$\ddot{\beta}_p(\beta_o, \dot{\beta}_o) = 0 \quad (4.77)$$

With  $\dot{\beta}_o = 0$  and the constraint in (4.49), the equilibrium angle  $\gamma_o$  must also be 0.

With  $\gamma_o=0$  and the conditions in (2.29) and (4.77), the terms  $f_{yr}(\beta_o)$  and  $\sin \beta_o$  must be 0 as

well. Thus the equilibrium points are  $(\beta_o, \dot{\beta}_o) = (0, 0)$  or  $(\pm\pi, 0)$  and  $(\alpha_o, \dot{\beta}_o) = (0, 0)$  or  $(\pm\pi, 0)$ .

The stability of these equilibrium points is evaluated by computing the stability of the linearized dynamics at each point. The linearized dynamics at an equilibrium point in terms of states  $(\beta_p, \dot{\beta}_p)$  are given as

$$\ddot{\beta}_p(\beta_p, \dot{\beta}_p) \approx c_2 f'_{yr}(\beta_o)([1 - \gamma_\beta(\beta_o, 0)](\beta_p - \beta_o) - \gamma_{\dot{\beta}}(\beta_o, 0)\dot{\beta}_p) \quad (4.78)$$

where  $f'_{yr}(x)$  is the derivative of  $f_{yr}(x)$  as

$$f'_{yr}(x) = \frac{df_{yr}}{dx} \quad (4.79)$$

and  $\gamma_\beta(\beta_p, \dot{\beta}_p)$  and  $\gamma_{\dot{\beta}}(\beta_p, \dot{\beta}_p)$  are partial derivatives of the angle  $\gamma$  given as

$$\gamma_\beta(\beta_p, \dot{\beta}_p) = \frac{\partial \gamma(\beta_p, \dot{\beta}_p)}{\partial \beta_p} = \frac{L \dot{\beta}_p \sin(\beta_p - \gamma(\beta_p, \dot{\beta}_p))}{v_r(\beta_p, \dot{\beta}_p)} \quad (4.80)$$

$$\gamma_{\dot{\beta}}(\beta_p, \dot{\beta}_p) = \frac{\partial \gamma(\beta_p, \dot{\beta}_p)}{\partial \dot{\beta}_p} = \frac{-L \cos(\beta_p - \gamma(\beta_p, \dot{\beta}_p))}{v_r(\beta_p, \dot{\beta}_p)} \quad (4.81)$$

so that the linearized dynamics simplify to

$$\ddot{\beta}_p(\beta_p, \dot{\beta}_p, u_3) \approx c_2 f'_{yr}(\beta_o) \frac{L \cos \beta_o}{v_p} \dot{\beta}_p + c_2 f'_{yr}(\beta_o)(\beta_p - \beta_o) \quad (4.82)$$

and are stable when

$$f'_{yr}(\beta_o) \cos \beta_o < 0 \quad (4.83)$$

$$f'_{yr}(\beta_o) < 0 \quad (4.84)$$

Recall the conditions in (2.27) and (2.29) that are consequences of the lateral force always opposing the direction of lateral slip. According to (2.29), it can be seen that  $f_{yr}(\beta_o) = 0$  for both  $\beta_o = 0$  and  $\beta_o = \pm\pi$ . The value of  $f'_{yr}(\beta_o)$  at each equilibrium point is computed with the following limit:

$$f'_{yr}(\beta_o) = \lim_{h \rightarrow 0} \frac{f_{yr}(\beta_o + h) - f_{yr}(\beta_o - h)}{2h} \quad (4.85)$$

For  $0 < h < \pi$ , it can be seen that  $f'_{yr}(0) < 0$ , since  $f_{yr}(h) < 0$  and  $f_{yr}(-h) > 0$  according to (2.27). In a similar manner, it can be shown that  $f'_{yr}(\pm\pi) > 0$ . Thus it can be seen

that  $(\beta_o, \dot{\beta}_o) = (0, 0)$  is the only stable equilibrium point since both equilibrium points satisfy (4.83), but only  $(\beta_o, \dot{\beta}_o) = (0, 0)$  satisfies (4.84).

Now, several candidate Lyapunov functions are considered to evaluate system stability. The first candidate Lyapunov function  $V_1(\alpha_r, \dot{\beta}_p)$  is based on the analogy of the yaw dynamics to a Liénard system. An energy-like candidate Lyapunov function inspired by this analogy is given as follows:

$$V_1(\alpha_r, \dot{\beta}_p) = \frac{1}{2} \dot{\beta}_p^2 - c_2 \int_0^{\alpha_r} f_{yr}(s) ds \quad (4.86)$$

The function  $V_1(\alpha_r, \dot{\beta}_p)$  has extrema when the following conditions are satisfied:

$$\frac{\partial V_1}{\partial \alpha_r} = 0 \quad \Rightarrow \quad \frac{\partial V_1}{\partial \alpha_r} = -c_2 f_{yr}(\alpha_r) = 0 \quad (4.87)$$

$$\frac{\partial V_1}{\partial \dot{\beta}_p} = 0 \quad \Rightarrow \quad \frac{\partial V_1}{\partial \dot{\beta}_p} = \dot{\beta}_p = 0 \quad (4.88)$$

which correspond to the equilibrium points  $(\alpha_o, \dot{\beta}_o) = (0, 0)$  and  $(\pm\pi, 0)$ . These extrema are minima when the following condition is satisfied:

$$\left( \frac{\partial^2 V_1}{\partial \alpha_r^2} \frac{\partial^2 V_1}{\partial \dot{\beta}_p^2} - \left( \frac{\partial^2 V_1}{\partial \alpha_r \partial \dot{\beta}_p} \right)^2 \right) \Bigg|_{(\alpha_r, \dot{\beta}_p) = (\alpha_o, 0)} > 0 \quad (4.89)$$

which reduces to

$$-c_2 f'_{yr}(\alpha_r) > 0 \quad (4.90)$$

which is equivalent to (4.84). Thus  $V_1(\alpha_r, \dot{\beta}_p)$  is locally positive definite at the stable equilibrium point  $(\alpha_o, \dot{\beta}_o) = (0, 0)$ .

The time derivative of  $V_1(\alpha_r, \dot{\beta}_p)$  is computed as follows:

$$\dot{V}_1(\alpha_r, \dot{\beta}_p) = \dot{\beta}_p \ddot{\beta}_p - c_2 f_{yr}(\alpha_r) \dot{\alpha}_r \quad (4.91)$$

$$\dot{V}_1(\alpha_r, \dot{\beta}_p) = c_2 f_{yr}(\alpha_r) \dot{y}(\alpha_r, \dot{\beta}_p) \quad (4.92)$$

$$\dot{V}_1(\alpha_r, \dot{\beta}_p) = \frac{-c_2 L}{v_r(\alpha_r, \dot{\beta}_p)} (c_2 f_{yr}(\alpha_r)^2 \cos \alpha_r - \dot{\beta}_p^2 f_{yr}(\alpha_r) \sin \alpha_r) \quad (4.93)$$

Recalling the condition in (2.27), it can be seen that  $\dot{V}_1(\alpha_r, \dot{\beta}_p) \leq 0$  for  $\cos \alpha_r \geq 0$ , with  $\dot{V}_1(\alpha_r, \dot{\beta}_p) = 0$  only when  $\sin \alpha_r = 0$ . This implies that  $V_1(\alpha_r, \dot{\beta}_p)$  is a Lyapunov function for the system. Asymptotic stability of the equilibrium point at the origin can be shown using  $V_1(\alpha_r, \dot{\beta}_p)$  as well with LaSalle's Theorem [66] which implies that  $\dot{V}_1(\alpha_r, \dot{\beta}_p) \rightarrow 0$  as time approaches  $\infty$ . Since  $\dot{V}_1(\alpha_r, \dot{\beta}_p) = 0$  when  $\sin \alpha_r = 0$ , the largest invariant set for which  $\dot{V}_1(\alpha_r, \dot{\beta}_p) = 0$  satisfies the following

$$\frac{d}{dt} (\sin \alpha_r) \Big|_{\alpha_r = \sin^{-1}(0)} = 0 \quad (4.94)$$

$$(\dot{\alpha}_r \cos \alpha_r) \Big|_{\alpha_r = \sin^{-1}(0)} = 0 \quad (4.95)$$

which is equivalent to

$$\dot{\beta}_p = 0 \quad (4.96)$$

which corresponds to the equilibrium points of the system. For  $\cos \alpha_r \geq 0$ , the largest invariant set for which  $\dot{V}_1(\alpha_r, \dot{\beta}_p) = 0$  is the stable equilibrium point at the origin.

Note also that the magnitude of  $\dot{V}_1(\alpha_r, \dot{\beta}_p)$  is inversely proportional to the rear wheel speed  $v_r(\alpha_r, \dot{\beta}_p)$ . This agrees with previous work stating that the damping of the linearized bicycle yaw dynamics is inversely proportional to vehicle speed [1].

While the first Lyapunov function  $V_1(\alpha_r, \dot{\beta}_p)$  is sufficient to establish asymptotic stability of the equilibrium point at the origin for a wide range of the state space, its derivative is only negative semi-definite, with  $\dot{V}_1(\alpha_r, \dot{\beta}_p) = 0$  for  $\sin \alpha_r = 0$ . An additional Lyapunov function is introduced that can be used to generate a Lyapunov function with a locally negative definite derivative.

The second candidate Lyapunov function  $V_2(\beta_p, \dot{\beta}_p)$  is based on the analogy of the yaw dynamics to a second order mechanical system. An energy-like candidate Lyapunov function inspired by this analogy is given as follows:

$$V_2(\beta_p, \dot{\beta}_p) = \frac{1}{2} \dot{\beta}_p^2 - c_2 \int_0^{\beta_p} f_{yr}(s) ds \quad (4.97)$$

The time derivative of  $V_2(\beta_p, \dot{\beta}_p)$  is computed as follows:

$$\dot{V}_2(\beta_p, \dot{\beta}_p) = \dot{\beta}_p \ddot{\beta}_p - c_2 f_{yr}(\beta_p) \dot{\beta}_p \quad (4.98)$$

$$\dot{V}_2(\beta_p, \dot{\beta}_p) = c_2 \dot{\beta}_p (f_{yr}(\beta_p) - \gamma(\beta_p, \dot{\beta}_p)) - f_{yr}(\beta_p) \quad (4.99)$$

To illustrate the behavior of  $\dot{V}_2(\beta_p, \dot{\beta}_p)$ , the angle  $\beta_2$  is introduced as

$$\beta_2 = \beta_p - \gamma(\beta_p, \dot{\beta}_p)/2 \quad (4.100)$$

and the derivative  $\dot{V}_2(\beta_p, \dot{\beta}_p)$  is expressed in terms of  $(\beta_2, \gamma)$  using (4.74) to replace  $\dot{\beta}_p$  with  $\gamma$  as

$$\dot{V}_2(\beta_2, \gamma) = -\frac{c_2 v_p \sin \gamma}{L \cos(\beta_2 - \gamma/2)} (f_{yr}(\beta_2 - \gamma/2) - f_{yr}(\beta_2 + \gamma/2)) \quad (4.101)$$

and with the first-order central difference approximation of  $f'_{yr}(\beta_2)$  with step size  $\gamma/2$  defined as

$$\hat{f}'_{yr}(\beta_2, \gamma) = \frac{f_{yr}(\beta_2 + \gamma/2) - f_{yr}(\beta_2 - \gamma/2)}{\gamma} \approx f'_{yr}(\beta_2) \quad (4.102)$$

the derivative  $\dot{V}_2(\beta_2, \gamma)$  is re-expressed as follows:

$$\dot{V}_2(\beta_2, \gamma) = \frac{c_2 v_p \gamma \sin \gamma \hat{f}'_{yr}(\beta_2, \gamma)}{L \cos(\beta_2 - \gamma/2)} \quad (4.103)$$

Since the term  $\gamma \sin \gamma$  is non-negative for  $\gamma \in [-\pi, \pi]$ , it can be seen that  $\dot{V}_2(\beta_2, \gamma) \leq 0$  for  $\hat{f}'_{yr}(\beta_2) / \cos \alpha_r < 0$  and that  $\dot{V}_2(\beta_2, \gamma) = 0$  for  $\gamma = 0$  or  $\hat{f}'_{yr}(\beta_2) = 0$ . It was shown previously that the function  $f'_{yr}(\cdot)$  is negative at zero, though it may become positive if the friction forces reach a peak value and exhibit a drop-off from the peak, such as the tire models illustrated in Fig. 2.4. As an example, the range of states for which  $\dot{V}_2(\beta_p, \dot{\beta}_p)$  is negative semi-definite are computed numerically for the model parameters given in Chapter 2 and illustrated in Fig. 4.3.

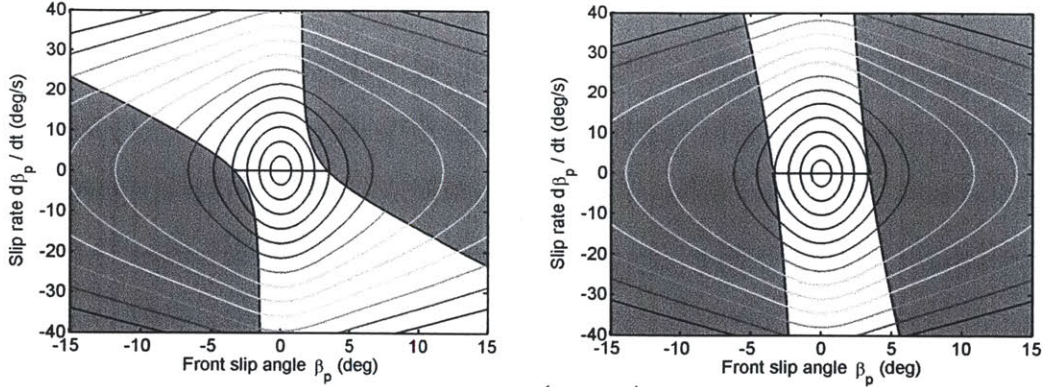


Fig. 4.3. Contours of Lyapunov function  $V_2(\beta_p, \dot{\beta}_p)$  for model parameters in Chapter 2 with speed  $v_p = 5$  m/s in the left subfigure and  $v_p = 35$  m/s in the right subfigure. The contour for  $\dot{V}_2(\beta_p, \dot{\beta}_p) = 0$  is a solid black line, and the area for which  $\dot{V}_2(\beta_p, \dot{\beta}_p) > 0$  is darkened.

Although  $V_1(\alpha_r, \dot{\beta}_p)$  is sufficient to prove asymptotic stability of the equilibrium point at the origin for a large portion of the state space, it is worth noting that the sum of  $\dot{V}_1(\alpha_r, \dot{\beta}_p)$  and  $\dot{V}_2(\beta_p, \dot{\beta}_p)$  is locally negative definite. Since both functions are locally negative semi-definite with  $\dot{V}_1(\alpha_r, \dot{\beta}_p) = 0$  near the origin only when  $\alpha_r = 0$ , the sum  $\dot{V}_1(\alpha_r, \dot{\beta}_p) + \dot{V}_2(\beta_p, \dot{\beta}_p)$  is locally negative definite if  $\dot{V}_2(\beta_p, \dot{\beta}_p)$  is locally negative definite for  $\alpha_r = 0$ . To prove this, the function  $\dot{V}_2(\beta_p, \dot{\beta}_p)$  is transformed into  $\dot{V}_{2\alpha}(\alpha_r, \gamma)$  as

$$\dot{V}_{2\alpha}(\alpha_r, \gamma) = -c_2 \frac{v_p \sin \gamma}{L \cos \alpha_r} (f_{yr}(\alpha_r) - f_{yr}(\alpha_r + \gamma)) \quad (4.104)$$

and is evaluated at  $\alpha_r = 0$  as

$$\dot{V}_{2\alpha}(0, \gamma) = \frac{c_2 v_p}{L} f_{yr}(\gamma) \sin \gamma \quad (4.105)$$

which is negative definite for  $\gamma \neq 0$  (or  $\dot{\beta}_p \neq 0$ ) according to (2.27). Thus, the sum of Lyapunov functions  $\dot{V}_1(\alpha_r, \dot{\beta}_p)$  and  $\dot{V}_2(\beta_p, \dot{\beta}_p)$  is itself a Lyapunov function with a locally negative definite derivative.

This stability analysis has indicated that the nonlinear dynamics are asymptotically stable with respect to the equilibrium point at the origin of state space. This is

demonstrated by simulating the dynamics given in (4.61)-(4.62) with constant speed  $v_p$ , heading  $\theta_p$ , and input  $u_3$ . The results are presented in terms of states  $(\alpha_r, \dot{\beta}_p)$  and Lyapunov function  $V_1(\alpha_r, \dot{\beta}_p)$ . The first straight-line trajectory is simulated at speeds of  $v_p = 5$  and  $35$  m/s with  $u_3=0$ , an initial rear slip angle of  $\alpha_r = -20$  deg, and an initial body slip rate of  $\dot{\beta}_p = 0$ . Snapshots of the vehicle orientation are shown in Fig. 4.4. The simulated time responses of  $\alpha_r$  and  $\dot{\beta}_p$  are shown in Fig. 4.5. A phase plane plot with phase variables  $\alpha_r$  and  $\dot{\beta}_p$  and the value of  $V_1(\alpha_r, \dot{\beta}_p)$  are shown in Fig. 4.6.

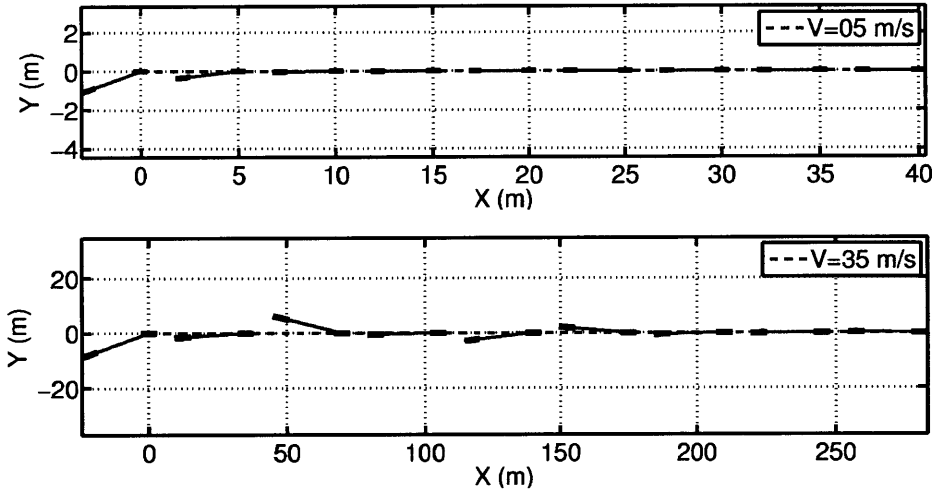


Fig. 4.4. Snapshots at 1 second intervals of vehicle orientation while tracking straight-line trajectories at constant speed. The vehicle size is enlarged and not to scale in the illustration of the 35 m/s trajectory to improve visibility.

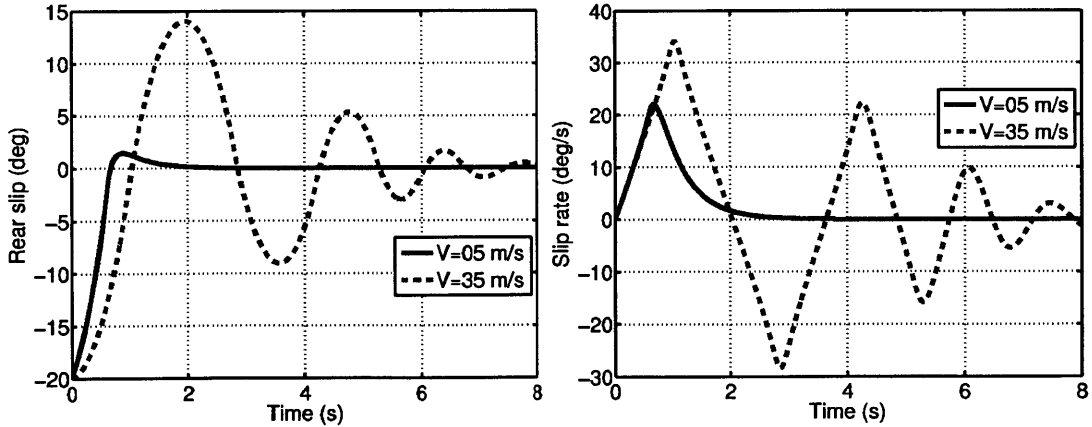


Fig. 4.5. Rear slip angle  $\alpha_r$  and slip rate  $\dot{\beta}_p$  during straight-line trajectory at constant speed with  $u_3=0$ .

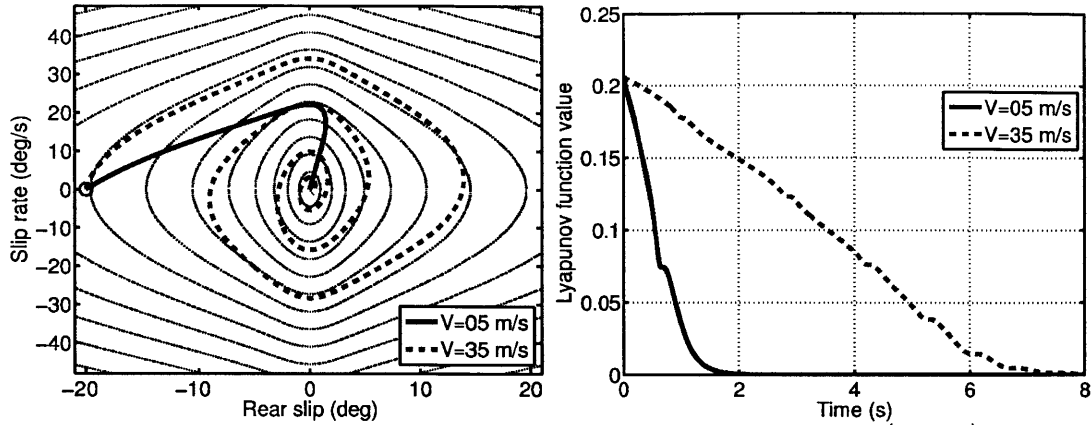


Fig. 4.6. Phase plane plot of yaw dynamics and Lyapunov function  $V_1(\alpha_r, \dot{\beta}_p)$  during straight-line trajectory at constant speed with  $u_3=0$ . In the phase plane plot, contours of the Lyapunov function  $V_1(\alpha_r, \dot{\beta}_p)$  are included in the background.

For both speeds, the slip angle  $\alpha_r$ , slip rate  $\dot{\beta}_p$ , and Lyapunov function value  $V_1(\alpha_r, \dot{\beta}_p)$  converge to zero during the straight-line trajectory. The inverse relationship between damping and speed is evident, as the rate of decrease in the Lyapunov function value is slower for the 35 m/s trajectory than the 5 m/s trajectory. At 5 m/s, the Lyapunov function reaches a value of 0.001 after  $t=1.85$ s, while the 35 m/s trajectory does not reach this energy level until  $t=7.74$ s. The reduced damping at 35 m/s also causes oscillation in the slip angle and yaw rate prior to convergence. It can be seen that the rate of decrease of the Lyapunov function value is approximately linear at each speed. The trajectories can be seen to cross the contours corresponding to decreases in the Lyapunov function value.

A limit on the basin of attraction for the yaw dynamics is imposed by limits on the actuators used to apply the control laws for  $u_1(t)$  and  $u_2(t)$ . The steering angle  $\delta$  and front longitudinal force  $F_{zf}$  used to apply  $u_1(t)$  and  $u_2(t)$  for the simulations shown in Figs. 4.5-4.6 are plotted in Fig. 4.7. The peak steering angle for each trajectory occurs near the initial slip angle of 20 deg, while the peak value of  $F_{zf}$  is approximately  $0.03 F_{zf}$  at 5 m/s and  $0.1 F_{zf}$  at 35 m/s.

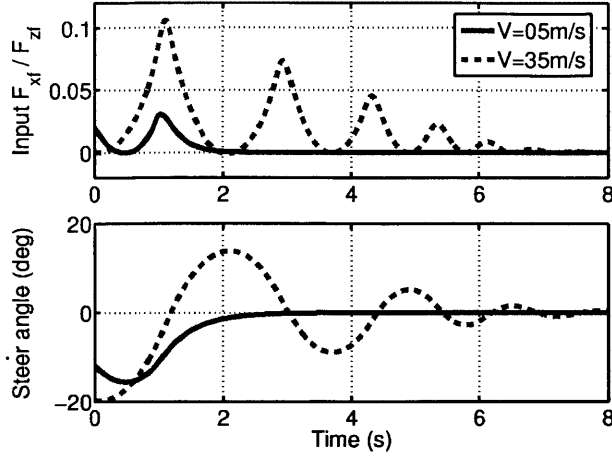


Fig. 4.7. Steering angle and front traction/braking force  $F_{xf}$  inputs while tracking straight-line trajectory at constant speed with  $u_3=0$  when starting from an initial slip angle of 20 deg.

The yaw dynamics are also simulated for this straight-line trajectory with the input  $u_3=0.7$ . Although this trajectory does not require large tire forces at the rear wheel, the input  $u_3$  can still be applied if it is counteracted by an additional force at the front. For example, a rear wheel drive force can be counteracted with front wheel braking. This may correspond to the left-footed braking technique employed by rally racing drivers [73]. The nonzero value of  $u_3$  causes the value of  $c_2$  to be reduced, which effectively reduces the magnitude of the term resembling potential energy  $\left(c_2 \int_0^{\alpha_r} f_{yr}(s)ds\right)$  in the Lyapunov function. Simulated phase plane trajectories and the values of  $V_1(\alpha_r, \dot{\beta}_p)$  are plotted in Fig. 4.8.

By comparing Fig. 4.8 with Fig. 4.6, the effect of reduced potential energy magnitude can be seen in the changed Lyapunov function contours and the reduced initial value of the Lyapunov function from 0.20 to 0.15. The Lyapunov function contours appear "flattened" in the phase space, such that the contour corresponding to 20 deg of rear slip corresponds to a reduced slip rate. Another effect of a nonzero  $u_3$  is that the rate of convergence is decreased, particularly for the 35 m/s trajectory, for which the convergence time of the Lyapunov function value to 0.001 increased from  $t=7.74s$  to  $t=10.6s$ .

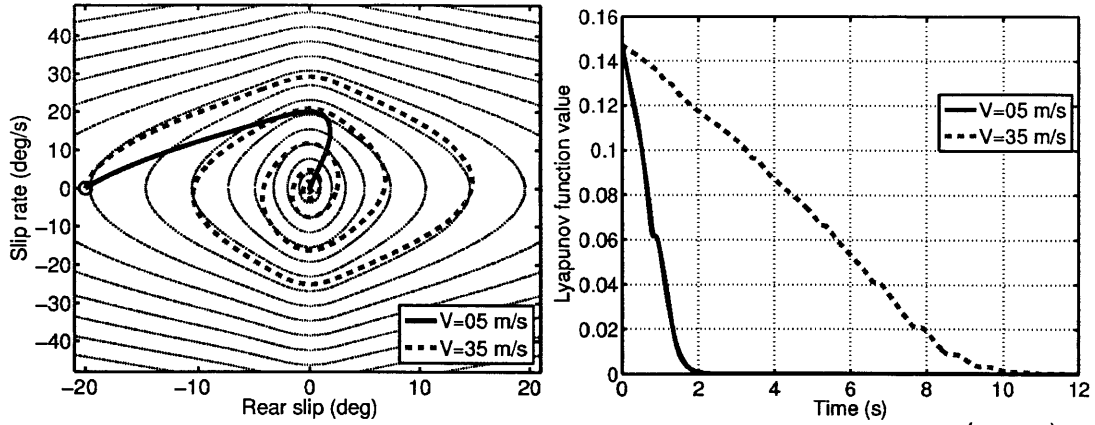


Fig. 4.8. Phase plane plot of yaw dynamics and Lyapunov function value  $V_1(\alpha_r, \dot{\beta}_p)$  during straight-line trajectory at constant speed with  $u_3=0.7$ . In the phase plane plot, contours of the Lyapunov function are included in the background.

#### 4.2.3 Stability of yaw dynamics during turning

In this section, the stability of the yaw dynamics is evaluated during constant radius turn maneuvers at constant speed with a constant  $u_3$  input ( $u_v = \dot{u}_\theta = \dot{u}_3 = 0$ ) and  $|u_3| < 1$ . The dynamics are simplified according to these forcing conditions, and the location and stability of equilibrium points are found. Several Lyapunov functions are considered to evaluate system stability, and stability claims are verified with simulation results.

With the forcing conditions given above, the yaw dynamics can be expressed in terms of  $(\beta_p, \dot{\beta}_p)$  as

$$\ddot{\beta}_p(\beta_p, \dot{\beta}_p) = c_2(-u_{\theta 3} \cos \beta_p + f_{yr}(\beta_p - \gamma(\beta_p, \dot{\beta}_p))) \quad (4.106)$$

with constant  $c_2$  defined previously in (4.67) and  $u_{\theta 3}$  defined as

$$u_{\theta 3} = \frac{u_\theta}{\sqrt{1-u_3^2}} \quad (4.107)$$

and the angle  $\gamma$  and rear speed  $v_r$  computed as:

$$\gamma(\beta_p, \dot{\beta}_p) = \tan^{-1}\left(\frac{-L(\dot{\beta}_p - \dot{\theta}_p)\cos \beta_p}{v_p + L(\dot{\beta}_p - \dot{\theta}_p)\sin \beta_p}\right) \quad (4.108)$$

$$v_r(\beta_p, \dot{\beta}_p) = \sqrt{(v_p \sin \beta_p + L(\dot{\beta}_p - \dot{\theta}_p))^2 + (v_p \cos \beta_p)^2} \quad (4.109)$$

recalling that  $\dot{\theta}_p$  is related to the input  $u_\theta$  as

$$\dot{\theta}_p = \frac{g}{v_p} u_\theta \quad (4.110)$$

Likewise, the functions  $f_2$  and  $f_4$  are simplified as

$$f_2(\alpha_r, \dot{\beta}_p) = c_2 u_{\theta 3} \cos(\alpha_r + \gamma(\alpha_r, \dot{\beta}_p)) \quad (4.111)$$

$$f_4(\alpha_r, \dot{\beta}_p, t) = L f_2(\alpha_r, \dot{\beta}_p) \cos \alpha_r + L(\dot{\beta}_p - \dot{\theta}_p(t)) \dot{\beta}_p \sin \alpha_r \quad (4.112)$$

so that the dynamics are expressed in terms of  $(\alpha_r, \dot{\beta}_p)$  as:

$$\begin{aligned} \dot{\alpha}_r(\alpha_r, \dot{\beta}_p) &= \dot{\beta}_p + \frac{L c_2 \cos \alpha_r}{v_r(\alpha_r, \dot{\beta}_p)} (-u_{\theta 3} \cos(\alpha_r + \gamma(\alpha_r, \dot{\beta}_p)) + f_{yr}(\alpha_r)) \\ &\quad - L \frac{\dot{\beta}_p (\dot{\beta}_p - \dot{\theta}_p) \sin \alpha_r}{v_r(\alpha_r, \dot{\beta}_p)} \end{aligned} \quad (4.113)$$

$$\ddot{\beta}_p(\alpha_r, \dot{\beta}_p) = c_2 (-u_{\theta 3} \cos(\alpha_r + \gamma(\alpha_r, \dot{\beta}_p)) + f_{yr}(\alpha_r)) \quad (4.114)$$

with the angle  $\gamma$  and rear speed  $v_r$  computed as:

$$\gamma(\alpha_r, \dot{\beta}_p) = \sin^{-1} \left( -\frac{L(\dot{\beta}_p - \dot{\theta}_p) \cos \alpha_r}{v_p} \right) \quad (4.115)$$

$$v_r(\alpha_r, \dot{\beta}_p) = v_p \cos \gamma(\alpha_r, \dot{\beta}_p) + L(\dot{\beta}_p - \dot{\theta}_p) \sin \alpha_r \quad (4.116)$$

The locations of equilibrium points  $(\beta_o, \dot{\beta}_o)$  and  $(\alpha_o, \dot{\beta}_o)$  are computed in terms of states  $(\beta_p, \dot{\beta}_p)$  using the following conditions:

$$\dot{\beta}_p = 0 \Rightarrow \dot{\beta}_o = 0 \quad (4.117)$$

$$\ddot{\beta}_p(\beta_o, \dot{\beta}_o) = 0 \quad (4.118)$$

With  $\dot{\beta}_o = 0$ , the equilibrium angle  $\beta_o$  is found as the implicit solution of

$$u_{\theta 3} \cos \beta_o = f_{yr}(\beta_o - \gamma(\beta_o, 0)) \quad (4.119)$$

or equivalently, the equilibrium angle  $\alpha_o$  can be found as the implicit solution of

$$u_{\theta 3} \cos(\alpha_o + \gamma(\alpha_o, 0)) = f_{yr}(\alpha_o) \quad (4.120)$$

Without additional knowledge of the function  $f_{yr}(\cdot)$ , it is difficult to compute the equilibrium values of  $\beta_o$  and  $\alpha_o$  explicitly. The values of  $\alpha_o$  that satisfy (4.120) are computed numerically in terms of the input  $u_{\theta 3}$  for the model parameters given in Chapter 2 and are plotted in Fig. 4.9 for two speeds. For small values of the input  $u_{\theta 3}$  (less than

roughly 0.18), there exists a single equilibrium slip angle  $\alpha_o$ , which has a magnitude less than 2 deg. For larger values of  $u_{\theta 3}$  (between roughly 0.18 and 0.25), there exist multiple values of the equilibrium slip angle  $\alpha_o$ , ranging in magnitude from 1.5 deg to 59 deg. For very large values of  $u_{\theta 3}$  (greater than roughly 0.25), there exists a single equilibrium slip angle  $\alpha_o$ , with magnitude greater than 50 deg.

The curve corresponding to  $u_{\theta 3} = f_{yr}(\alpha_o)$  is plotted in Fig. 4.9 as well. Since the output magnitude of the cosine function is bounded at 1, this curve corresponds to a limiting curve for relationships between  $u_{\theta 3}$  and  $\alpha_o$  based on (4.120). In particular, the value  $f_{yr}(\alpha_o)$  represents the minimum value of  $u_{\theta 3}$  required to reach equilibrium at a given slip angle  $\alpha_o$ , which can be seen in Fig. 4.9.

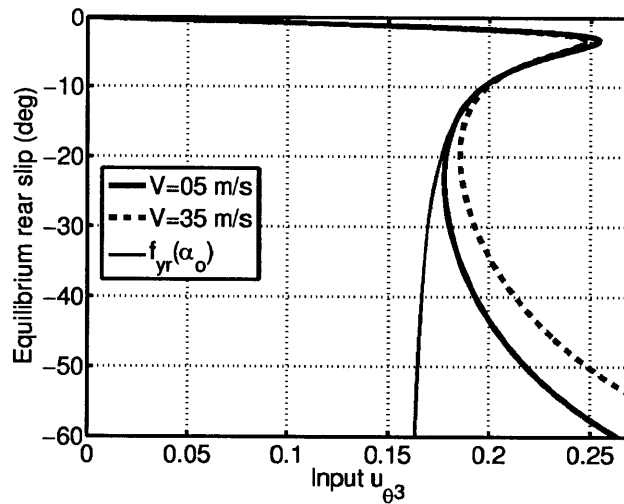


Fig. 4.9. Plots of equilibrium rear slip  $\alpha_o$  for a given value of  $u_{\theta 3}$  computed numerically from (4.120) for  $v_p = 5$  m/s and  $v_p = 35$  m/s. The curve corresponding to  $u_{\theta 3} = f_{yr}(\alpha_o)$  is plotted as well for reference.

The stability of these equilibrium points is evaluated by computing the stability of the linearized dynamics at each point. The linearized dynamics at an equilibrium point in terms of states  $(\beta_p, \dot{\beta}_p)$  are given as

$$\ddot{\beta}_p(\beta_p, \dot{\beta}_p) \approx c_2 f'_{yr}(\beta_o - \gamma(\beta_o, 0))((1 - \gamma_\beta(\beta_o, 0))(\beta_p - \beta_o) - \gamma_{\dot{\beta}}(\beta_o, 0)\dot{\beta}_p) + c_2 u_{\theta 3} \sin \beta_o (\beta_p - \beta_o) \quad (4.121)$$

where  $f'_{yr}(x)$  is the derivative of  $f_{yr}(x)$  as defined in (4.79) and  $\gamma_\beta(\beta_p, \dot{\beta}_p)$  and  $\gamma_{\dot{\beta}}(\beta_p, \dot{\beta}_p)$  are partial derivatives of the angle  $\gamma$  given as follows:

$$\gamma_\beta(\beta_p, \dot{\beta}_p) = \frac{\partial \gamma(\beta_p, \dot{\beta}_p)}{\partial \beta_p} = \frac{L(\dot{\beta}_p - \dot{\theta}_p) \sin(\beta_p - \gamma(\beta_p, \dot{\beta}_p))}{v_r(\beta_p, \dot{\beta}_p)} \quad (4.122)$$

$$\gamma_{\dot{\beta}}(\beta_p, \dot{\beta}_p) = \frac{\partial \gamma(\beta_p, \dot{\beta}_p)}{\partial \dot{\beta}_p} = \frac{-L \cos(\beta_p - \gamma(\beta_p, \dot{\beta}_p))}{v_r(\beta_p, \dot{\beta}_p)} \quad (4.123)$$

For  $\dot{\beta}_o = 0$  and  $\alpha_o = \beta_o - \gamma(\beta_o, 0)$ , the linearized dynamics simplify to

$$\begin{aligned} \ddot{\beta}_p(\beta_p, \dot{\beta}_p) &\approx c_2 f'_{yr}(\alpha_o) \frac{L \cos \alpha_o}{v_r(\beta_o, 0)} \dot{\beta}_p \\ &+ c_2 \left( u_{\theta 3} \sin \beta_o + f'_{yr}(\alpha_o) \left( 1 + \frac{L \dot{\theta}_p \sin \alpha_o}{v_r(\beta_o, 0)} \right) \right) (\beta_p - \beta_o) \end{aligned} \quad (4.124)$$

and are stable when the following conditions are met:

$$f'_{yr}(\alpha_o) \cos \alpha_o < 0 \quad (4.125)$$

$$u_{\theta 3} \sin \beta_o + f'_{yr}(\alpha_o) \left( 1 + \frac{L \dot{\theta}_p \sin \alpha_o}{v_r(\beta_o, 0)} \right) < 0 \quad (4.126)$$

The first stability condition in (4.125) requires that the curve  $f_{yr}(\alpha_r)$  has negative slope at the equilibrium point when  $\cos \alpha_o > 0$  and that the curve has positive slope at the equilibrium point when  $\cos \alpha_o < 0$ . For the tire model parameters given in Chapter Two and illustrated in Fig. 2.4, the function  $f_{yr}(\alpha_r)$  has negative slope near the origin between the extreme values at  $\alpha_r = \pm \alpha_{peak}$ . Likewise, the function  $f_{yr}(\alpha_r)$  has positive slope near  $\alpha_r = \pm \pi$  between the peaks at  $\pi \pm \alpha_{peak}$  and  $-\pi \pm \alpha_{peak}$ . Thus the stability condition in (4.125) implies that the stable equilibrium values of  $\alpha_o$  must lie between the peaks of the tire force curve  $f_{yr}(\alpha_r)$  near  $\alpha_o = 0$  and  $\alpha_o = \pm \pi$ . This is illustrated for the portion of the tire force curve near  $\alpha_o = 0$  in Fig. 4.10. Thus all the equilibrium points in Fig. 4.9 for which  $|\alpha_o| > |\alpha_{peak}|$  are unstable.

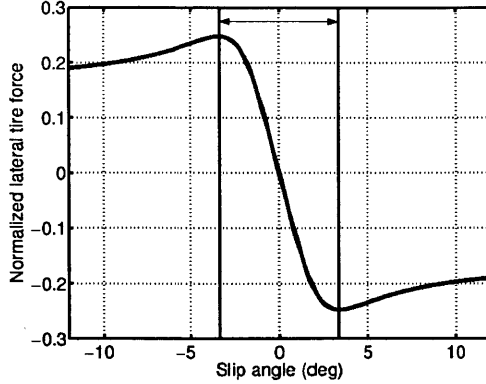


Fig. 4.10. Plot of  $f_{yr}(\alpha_o)$  with area between peaks of curve indicated.

Considering the case of forward travel with  $|\alpha_o| < \pi/2$ , the stability condition in (4.125) implies that stable equilibrium points must satisfy  $|\alpha_o| < |\alpha_{peak}|$ . To guarantee that an equilibrium point exists on this interval, the input  $u_{\theta_3}$  should be constrained to not exceed the peak value of the function  $f_{yr}(\alpha_r)$  as follows:

$$|u_{\theta_3}| < |f_{yr}(\alpha_{peak})| \quad (4.127)$$

With this assumption, the effect of the second stability condition in (4.126) is assessed. While the first stability condition depends solely on the properties of the rear tire model  $f_{yr}(\alpha_r)$  and direction of travel  $\cos \alpha_o$ , the second stability condition depends on the input  $u_{\theta_3}$  as well. A series of identities and algebraic manipulations are used to transform the second stability condition as shown below. Using the identity in (4.54), the stability condition in (4.126) is rewritten as

$$u_{\theta_3} \sin \beta_o \frac{v_r(\beta_o, 0)}{v_p \cos \gamma(\beta_o, 0)} + f'_{yr}(\alpha_o) < 0 \quad (4.128)$$

and simplified using the stability condition in (4.120) as

$$\frac{f_{yr}(\alpha_o)}{\cos \beta_o} \sin \beta_o \frac{v_r(\beta_o, 0)}{v_p \cos \gamma(\beta_o, 0)} + f'_{yr}(\alpha_o) < 0 \quad (4.129)$$

and then simplified further using the following identity:

$$v_p \cos \beta_p = v_r \cos \alpha_r \quad (4.130)$$

$$\frac{f_{yr}(\alpha_o) \sin \beta_o}{\cos \alpha_o \cos \gamma(\beta_o, 0)} + f'_{yr}(\alpha_o) < 0 \quad (4.131)$$

A trigonometric identity is used to simplify the term  $\sin \beta_o / (\cos \alpha_o \cos \gamma)$  as

$$f_{yr}(\alpha_o)(\tan \alpha_o + \tan \gamma_o) + f'_{yr}(\alpha_o) < 0 \quad (4.132)$$

and the expression for  $\tan \gamma$  is substituted from (4.36) as

$$f_{yr}(\alpha_o) \left( \tan \alpha_o + \frac{L\dot{\theta}_p \cos \beta_o}{v_p - L\dot{\theta}_p \sin \beta_o} \right) + f'_{yr}(\alpha_o) < 0 \quad (4.133)$$

and the quantity  $\dot{\theta}_p$  is converted to  $u_{\theta 3}$  as

$$f_{yr}(\alpha_o) \left( \tan \alpha_o + \frac{Lg}{v_p} \frac{u_{\theta 3} \sqrt{1-u_3^2} \cos \beta_o}{v_p - \frac{Lg}{v_p} u_{\theta 3} \sqrt{1-u_3^2} \sin \beta_o} \right) + f'_{yr}(\alpha_o) < 0 \quad (4.134)$$

with the expression simplified using the stability condition in (4.120) as follows:

$$f_{yr}(\alpha_o) \left( \tan \alpha_o + \frac{\frac{f_{yr}(\alpha_o)}{v_p^2}}{\frac{1}{Lg} \frac{1}{\sqrt{1-u_3^2}} - u_{\theta 3} \sin \beta_o} \right) + f'_{yr}(\alpha_o) < 0 \quad (4.135)$$

The terms in (4.135) are rearranged as

$$\frac{1}{\frac{v_p^2}{Lg} \frac{1}{\sqrt{1-u_3^2}} - u_{\theta 3} \sin \beta_o} < \frac{-f'_{yr}(\alpha_o) - f_{yr}(\alpha_o) \tan \alpha_o}{f_{yr}^2(\alpha_o)} \quad (4.136)$$

and inverted as follows:

$$\frac{v_p^2}{Lg} \frac{1}{\sqrt{1-u_3^2}} - u_{\theta 3} \sin \beta_o > \frac{f_{yr}^2(\alpha_o)}{-f'_{yr}(\alpha_o) - f_{yr}(\alpha_o) \tan \alpha_o} \quad (4.137)$$

Using the constraint on  $u_{\theta 3}$  from (4.127), this inequality can be conservatively approximated by the following:

$$\frac{v_p^2}{Lg} \frac{1}{\sqrt{1-u_3^2}} > |f_{yr}(\alpha_{peak})| + \frac{f_{yr}^2(\alpha_o)}{-f'_{yr}(\alpha_o) - f_{yr}(\alpha_o) \tan \alpha_o} \quad (4.138)$$

In this form, the second stability condition in (4.126) has been reformulated and conservatively approximated as a constraint on the minimum speed required for an equilibrium point at a given equilibrium slip angle  $\alpha_o$ . It can be seen that the speed is

nondimensionalized as a Froude number  $Fr = v_p / \sqrt{Lg}$  [48] and scaled by the effect of input  $u_3$ . The minimum nondimensional speed for the model parameters from Chapter 2 is plotted in Fig. 4.11 for the interval  $|\alpha_o| < |\alpha_{peak}|$ .

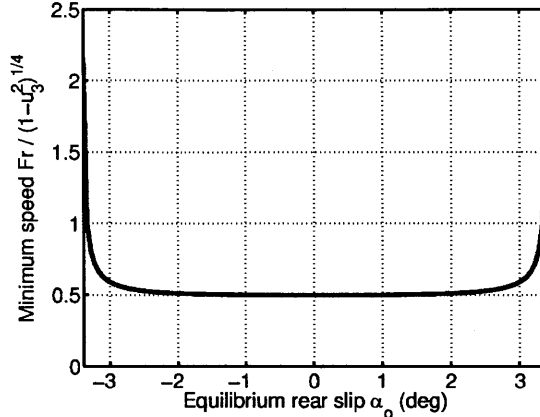


Fig. 4.11. Nondimensional speed  $Fr / (1 - u_3^2)^{1/4}$  that is sufficient to ensure stability of equilibrium rear slip angle  $\alpha_o$  for the tire parameters given in Chapter 2.

Two candidate Lyapunov functions that are similar to the Lyapunov functions in the previous section are considered to evaluate system stability. Although neither function is a Lyapunov function independently, it is conjectured that certain linear combinations of these functions are Lyapunov functions.

The candidate Lyapunov functions in this section are defined with respect to a stable equilibrium point  $(\alpha_o, \dot{\beta}_o)$  with  $\tilde{\alpha} = \alpha_r - \alpha_o$  representing the deviation from the equilibrium rear slip angle. The first candidate Lyapunov function  $V_1(\tilde{\alpha}, \dot{\beta}_p)$  is based on the analogy of the yaw dynamics to a Liénard system. An energy-like candidate Lyapunov function inspired by this analogy is given as

$$V_1(\tilde{\alpha}, \dot{\beta}_p) = \frac{1}{2} \dot{\beta}_p^2 - c_2 \int_{\alpha_o}^{\alpha_o + \tilde{\alpha}} f_{yr}(s) ds + c_2 u_{\theta_3} (\sin \beta_p(\tilde{\alpha}, \dot{\beta}_p) - \sin(\beta_p(\tilde{\alpha}, \dot{\beta}_p) - \tilde{\alpha})) \quad (4.139)$$

where  $\beta_p(\tilde{\alpha}, \dot{\beta}_p)$  and other functions of  $(\tilde{\alpha}, \dot{\beta}_p)$  are adapted from the functions previously given in terms of  $(\alpha_r, \dot{\beta}_p)$ .

The function  $V_1(\tilde{\alpha}, \dot{\beta}_p)$  has critical points when the partial derivatives  $\partial V_1 / \partial \tilde{\alpha}$  and  $\partial V_1 / \partial \dot{\beta}_p$  are zero. These partial derivatives are computed as

$$\frac{\partial V_1}{\partial \tilde{\alpha}} = -\ddot{\beta}_p(\tilde{\alpha}, \dot{\beta}_p) + c_2 u_{\theta 3} (\cos \beta_p(\tilde{\alpha}, \dot{\beta}_p) - \cos(\beta_p(\tilde{\alpha}, \dot{\beta}_p) - \tilde{\alpha})) \frac{\partial \gamma}{\partial \tilde{\alpha}} \quad (4.140)$$

$$\frac{\partial V_1}{\partial \dot{\beta}_p} = \dot{\beta}_p + c_2 u_{\theta 3} (\cos \beta_p(\tilde{\alpha}, \dot{\beta}_p) - \cos(\beta_p(\tilde{\alpha}, \dot{\beta}_p) - \tilde{\alpha})) \frac{\partial \gamma}{\partial \dot{\beta}_p} \quad (4.141)$$

and it can be seen that these partial derivatives are both zero at the equilibrium point  $(\tilde{\alpha}, \dot{\beta}_p) = (0,0)$ . The function  $V_1(\tilde{\alpha}, \dot{\beta}_p)$  is locally positive definite if the following conditions are met at the equilibrium point:

$$\frac{\partial^2 V_1}{\partial \tilde{\alpha}^2} > 0 \quad (4.142)$$

$$\frac{\partial^2 V_1}{\partial \dot{\beta}_p^2} > 0 \quad (4.143)$$

$$\frac{\partial^2 V_1}{\partial \tilde{\alpha}^2} \frac{\partial^2 V_1}{\partial \dot{\beta}_p^2} - \left( \frac{\partial^2 V_1}{\partial \tilde{\alpha} \partial \dot{\beta}_p} \right)^2 > 0 \quad (4.144)$$

It can be shown that the partial derivative  $\partial^2 V_1 / \partial \dot{\beta}_p^2$  has a value of 1 at the equilibrium point  $(\tilde{\alpha}, \dot{\beta}_p) = (0,0)$ . Thus the three conditions for  $V_1(\tilde{\alpha}, \dot{\beta}_p)$  to be locally positive definite given above are equivalent to the condition given below. This condition should be verified numerically for each operating point.

$$\frac{\partial^2 V_1}{\partial \tilde{\alpha}^2} > \left( \frac{\partial^2 V_1}{\partial \tilde{\alpha} \partial \dot{\beta}_p} \right)^2 \quad (4.145)$$

The time derivative of  $V_1(\tilde{\alpha}, \dot{\beta}_p)$  is computed as

$$\begin{aligned} \dot{V}_1(\tilde{\alpha}, \dot{\beta}_p) &= \dot{\beta}_p \ddot{\beta}_p(\tilde{\alpha}, \dot{\beta}_p) - c_2 f_{yr}(\alpha_o + \tilde{\alpha}) \dot{\alpha}_r(\tilde{\alpha}, \dot{\beta}_p) \\ &\quad + c_2 u_{\theta 3} (\dot{\beta}_p \cos \beta_p(\tilde{\alpha}, \dot{\beta}_p) - (\dot{\beta}_p - \dot{\alpha}_r(\tilde{\alpha}, \dot{\beta}_p)) \cos(\beta_p(\tilde{\alpha}, \dot{\beta}_p) - \tilde{\alpha})) \end{aligned} \quad (4.146)$$

and simplified as

$$\dot{V}_1(\tilde{\alpha}, \dot{\beta}_p) = -\dot{\gamma}(\tilde{\alpha}, \dot{\beta}_p) c_2 (u_{\theta 3} \cos(\beta_p(\tilde{\alpha}, \dot{\beta}_p) - \tilde{\alpha}) - f_{yr}(\alpha_o + \tilde{\alpha})) \quad (4.147)$$

$$\dot{V}_1(\tilde{\alpha}, \dot{\beta}_p) = -\frac{L \cos(\alpha_o + \tilde{\alpha})}{v_r(\tilde{\alpha}, \dot{\beta}_p)} (\ddot{\beta}_p(\tilde{\alpha}, \dot{\beta}_p) + 2A_1(\tilde{\alpha}, \dot{\beta}_p)) (\ddot{\beta}_p(\tilde{\alpha}, \dot{\beta}_p) + 2A_2(\tilde{\alpha}, \dot{\beta}_p)) \quad (4.148)$$

where  $A_1(\tilde{\alpha}, \dot{\beta}_p)$  and  $A_2(\tilde{\alpha}, \dot{\beta}_p)$  are given as follows:

$$A_1(\tilde{\alpha}, \dot{\beta}_p) = \frac{1}{2} (\dot{\theta}_p - \dot{\beta}_p) \dot{\beta}_p \tan(\alpha_o + \tilde{\alpha}) \quad (4.149)$$

$$A_2(\tilde{\alpha}, \dot{\beta}_p) = \frac{1}{2} c_2 u_{\theta 3} (\cos \beta_p (\tilde{\alpha}, \dot{\beta}_p) - \cos (\beta_p (\tilde{\alpha}, \dot{\beta}_p) - \tilde{\alpha})) \quad (4.150)$$

By completing the square, the time derivative  $V_1(\tilde{\alpha}, \dot{\beta}_p)$  is expressed as follows:

$$\begin{aligned} \dot{V}_1(\tilde{\alpha}, \dot{\beta}_p) &= -\frac{L \cos(\alpha_o + \tilde{\alpha})}{v_r(\tilde{\alpha}, \dot{\beta}_p)} (\ddot{\beta}_p(\tilde{\alpha}, \dot{\beta}_p) + A_1(\tilde{\alpha}, \dot{\beta}_p) + A_2(\tilde{\alpha}, \dot{\beta}_p))^2 \\ &\quad + \frac{L \cos(\alpha_o + \tilde{\alpha})}{v_r(\tilde{\alpha}, \dot{\beta}_p)} (A_1(\tilde{\alpha}, \dot{\beta}_p) - A_2(\tilde{\alpha}, \dot{\beta}_p))^2 \end{aligned} \quad (4.151)$$

It can be seen that the time derivative of  $V_1(\tilde{\alpha}, \dot{\beta}_p)$  can be expressed as a sum of squares with both positive and negative terms. It is neither guaranteed that  $\dot{V}_1(\tilde{\alpha}, \dot{\beta}_p)$  is negative semi-definite nor that  $V_1(\tilde{\alpha}, \dot{\beta}_p)$  is a Lyapunov function.

Though not locally negative semi-definite with respect to  $(\tilde{\alpha}, \dot{\beta}_p)$ , the function  $\dot{V}_1(\tilde{\alpha}, \dot{\beta}_p)$  is locally negative definite with respect to  $\tilde{\alpha}$  along the axis  $\dot{\beta}_p = 0$  if the following conditions are satisfied:

$$\frac{\partial \dot{V}_1}{\partial \tilde{\alpha}}(0,0) = 0 \quad (4.152)$$

$$\frac{\partial^2 \dot{V}_1}{\partial \tilde{\alpha}^2}(0,0) < 0 \quad (4.153)$$

The first condition on  $\partial \dot{V}_1 / \partial \tilde{\alpha}$  can be easily verified by differentiating (4.148) and evaluating at  $(\tilde{\alpha}, \dot{\beta}_p) = (0,0)$ , since  $\ddot{\beta}_p(0,0) = A_1(0,0) = A_2(0,0) = 0$ . The second condition can be evaluated by first computing the quantity  $\partial^2 \dot{V}_1 / \partial \tilde{\alpha}^2$  at  $(\tilde{\alpha}, \dot{\beta}_p) = (0,0)$  by twice differentiating (4.148) and simplifying to the following:

$$\frac{\partial^2 \dot{V}_1}{\partial \tilde{\alpha}^2}(0,0) = -2 \frac{L \cos(\alpha_o)}{v_r(0,0)} \left( \frac{\partial \ddot{\beta}_p}{\partial \tilde{\alpha}}(0,0) + 2 \frac{\partial A_1}{\partial \tilde{\alpha}}(0,0) \right) \left( \frac{\partial \ddot{\beta}_p}{\partial \tilde{\alpha}}(0,0) + 2 \frac{\partial A_2}{\partial \tilde{\alpha}}(0,0) \right) \quad (4.154)$$

The partial derivative  $\partial \ddot{\beta}_p / \partial \tilde{\alpha}$  is given as

$$\frac{\partial \ddot{\beta}_p}{\partial \tilde{\alpha}}(0,0) = u_{\theta 3} \sin \beta_o \frac{v_r(0,0)}{v_p \cos \gamma(0,0)} + f'_{yr}(\alpha_o) \quad (4.155)$$

and recalling (4.128), it can be seen that for stable equilibrium points

$$\frac{\partial \ddot{\beta}_p}{\partial \tilde{\alpha}}(0,0) < 0 \quad (4.156)$$

The other partial derivatives are given as

$$\frac{\partial A_1}{\partial \tilde{\alpha}}(0,0) = 0 \quad (4.157)$$

$$\frac{\partial A_2}{\partial \tilde{\alpha}}(0,0) = -\frac{1}{2}c_2 u_{\theta 3} \sin \beta_o \quad (4.158)$$

so that for  $\cos \alpha_o / v_r(0,0) > 0$ , the condition that  $\partial^2 \dot{V}_1 / \partial \tilde{\alpha}^2 < 0$  is equivalent to the following:

$$-\frac{\partial \ddot{\beta}_p}{\partial \tilde{\alpha}}(0,0) \left( \frac{\partial \ddot{\beta}_p}{\partial \tilde{\alpha}}(0,0) + 2 \frac{\partial A_2}{\partial \tilde{\alpha}}(0,0) \right) < 0 \quad (4.159)$$

or since  $\partial \ddot{\beta}_p / \partial \tilde{\alpha} < 0$ ,

$$\frac{\partial \ddot{\beta}_p}{\partial \tilde{\alpha}}(0,0) + 2 \frac{\partial A_2}{\partial \tilde{\alpha}}(0,0) < 0 \quad (4.160)$$

When  $\partial A_2 / \partial \tilde{\alpha} \leq 0$ , it can be seen that this condition is satisfied since  $\partial \ddot{\beta}_p / \partial \tilde{\alpha} < 0$ .

When  $\partial A_2 / \partial \tilde{\alpha} > 0$  (or equivalently  $u_{\theta 3} \sin \beta_o < 0$ ), the condition is reduced to

$$f'_{yr}(\alpha_o) + u_{\theta 3} \sin \beta_o \left( \frac{v_r(0,0)}{v_p \cos \gamma(0,0)} - 1 \right) < 0 \quad (4.161)$$

or equivalently using (4.38) as

$$f'_{yr}(\alpha_o) < u_{\theta 3} \sin \beta_o \frac{L \dot{\theta}_p \sin \alpha_o}{v_p \cos \gamma(0,0)} \quad (4.162)$$

and for  $\cos \alpha_o > 0$ , this condition must be satisfied since  $f'_{yr}(\alpha_o)$  is negative according to (4.125) and the right-hand term is positive since  $u_{\theta 3} \sin \beta_o < 0$  and  $\dot{\theta}_p \sin \alpha_o < 0$  (as a consequence of (2.27)). Thus it is verified that  $\dot{V}_1(\tilde{\alpha}, \dot{\beta}_p)$  is locally negative definite with respect to  $\tilde{\alpha}$  along the axis  $\dot{\beta}_p = 0$ .

Though  $V_1(\tilde{\alpha}, \dot{\beta}_p)$  is not a Lyapunov function, conditions were established for which it is locally positive definite, and its derivative was shown to be locally negative definite

with respect to  $\tilde{\alpha}$  along the axis  $\dot{\beta}_p = 0$ . A second candidate Lyapunov function  $V_2(\tilde{\beta}, \dot{\beta}_p)$  is based on the analogy of the yaw dynamics to a second order mechanical system, where  $\tilde{\beta} = \beta_p - \beta_o$  represents the deviation of the front slip angle from the equilibrium value. An energy-like function inspired by this analogy is given as follows:

$$V_2(\tilde{\beta}, \dot{\beta}_p) = \frac{1}{2} \dot{\beta}_p^2 - c_2 \int_{\alpha_o}^{\alpha_o + \tilde{\beta}} f_{yr}(s) ds + c_2 u_{\theta 3} (\sin(\beta_o + \tilde{\beta}) - \sin \beta_o) \quad (4.163)$$

The function  $V_2(\tilde{\beta}, \dot{\beta}_p)$  has extrema when the partial derivatives  $\partial V_2 / \partial \tilde{\beta}$  and  $\partial V_2 / \partial \dot{\beta}_p$  are zero. These partial derivatives are computed as

$$\frac{\partial V_2}{\partial \tilde{\beta}} = c_2 (u_{\theta 3} \cos(\beta_o + \tilde{\beta}) - f_{yr}(\alpha_o + \tilde{\beta})) \quad (4.164)$$

$$\frac{\partial V_2}{\partial \dot{\beta}_p} = \dot{\beta}_p \quad (4.165)$$

and it can be verified that these partial derivatives are zero at the equilibrium point  $(\tilde{\beta}, \dot{\beta}_p) = (0, 0)$ .

The function  $V_2(\tilde{\beta}, \dot{\beta}_p)$  is locally positive definite if the following conditions are satisfied at the equilibrium point  $(\tilde{\beta}, \dot{\beta}_p) = (0, 0)$ :

$$\frac{\partial^2 V_2}{\partial \tilde{\beta}^2} > 0 \quad (4.166)$$

$$\frac{\partial^2 V_2}{\partial \dot{\beta}_p^2} > 0 \quad (4.167)$$

$$\frac{\partial^2 V_2}{\partial \tilde{\beta}^2} \frac{\partial^2 V_2}{\partial \dot{\beta}_p^2} - \left( \frac{\partial^2 V_2}{\partial \tilde{\beta} \partial \dot{\beta}_p} \right)^2 > 0 \quad (4.168)$$

Since  $\partial^2 V_2 / \partial \dot{\beta}_p^2 = 1$  and  $\partial^2 V_2 / \partial \tilde{\beta} \partial \dot{\beta}_p = 0$ , these conditions are equivalent to the first condition in (4.166). An equivalent expression for this condition is given as

$$\frac{\partial^2 V_2}{\partial \tilde{\beta}^2} = -c_2 (u_{\theta 3} \sin(\beta_o) + f'_{yr}(\alpha_o)) > 0 \quad (4.169)$$

and this condition can be conservatively approximated using (4.127) as

$$f'_{yr}(\alpha_o) < -|f_{yr}(\alpha_{peak})| \quad (4.170)$$

which is more conservative than the conditions for stability of an equilibrium point given in (4.128) and illustrated in Fig. 4.11. This condition may limit the range of  $\alpha_o$  for which  $V_2(\tilde{\beta}, \dot{\beta}_p)$  is locally positive definite.

The time derivative of  $V_2(\tilde{\beta}, \dot{\beta}_p)$  is computed as

$$\dot{V}_2(\tilde{\beta}, \dot{\beta}_p) = \dot{\beta}_p \ddot{\beta}_p(\tilde{\beta}, \dot{\beta}_p) - \dot{\beta}_p c_2 f_{yr}(\alpha_o + \tilde{\beta}) + \dot{\beta}_p c_2 u_{\theta 3} \cos(\beta_o + \tilde{\beta}) \quad (4.171)$$

and can be simplified to the following:

$$\dot{V}_2(\tilde{\beta}, \dot{\beta}_p) = \dot{\beta}_p c_2 (f_{yr}(\alpha_r(\tilde{\beta}, \dot{\beta}_p)) - f_{yr}(\alpha_o + \tilde{\beta})) \quad (4.172)$$

In a similar manner to the previous section, the function  $\dot{V}_2(\tilde{\beta}, \dot{\beta}_p)$  is given in terms of  $(\beta_3, \tilde{\gamma})$  where

$$\gamma_o = \gamma(0,0) \quad (4.173)$$

$$\tilde{\gamma}(\tilde{\beta}, \dot{\beta}_p) = \gamma(\tilde{\beta}, \dot{\beta}_p) - \gamma_o \quad (4.174)$$

$$\beta_3(\tilde{\beta}, \dot{\beta}_p) = \alpha_o + \tilde{\beta} - \frac{\tilde{\gamma}(\tilde{\beta}, \dot{\beta}_p)}{2} \quad (4.175)$$

by first expressing  $\dot{\beta}_p$  in terms of  $(\beta_3, \tilde{\gamma})$  as

$$\dot{\beta}_p(\beta_3, \tilde{\gamma}) = \frac{v_p (\sin \gamma_o - \sin \tilde{\gamma})}{L \cos \alpha_r(\beta_3, \tilde{\gamma})} + \dot{\theta}_p \left( 1 - \frac{\cos \alpha_o}{\cos \alpha_r(\beta_3, \tilde{\gamma})} \right) \quad (4.176)$$

and with the first-order central difference approximation of  $f'_{yr}(\beta_3)$  with step size  $\tilde{\gamma}/2$  defined as

$$\hat{f}'_{yr}(\beta_3, \tilde{\gamma}) = \frac{f_{yr}(\beta_3 + \tilde{\gamma}/2) - f_{yr}(\beta_3 - \tilde{\gamma}/2)}{\tilde{\gamma}} \approx f'_{yr}(\beta_3) \quad (4.177)$$

the time derivative  $\dot{V}_2(\beta_3, \tilde{\gamma})$  is expressed as

$$\dot{V}_2(\beta_3, \tilde{\gamma}) = -\dot{\beta}_p(\beta_3, \tilde{\gamma}) c_2 \hat{f}'_{yr}(\beta_3, \tilde{\gamma}) \tilde{\gamma} \quad (4.178)$$

$$\dot{V}_2(\beta_3, \tilde{\gamma}) = c_2 \hat{f}'_{yr}(\beta_3, \tilde{\gamma}) \tilde{\gamma} \left( \frac{v_p (\sin \tilde{\gamma} - \sin \gamma_o)}{L \cos \alpha_r(\beta_3, \tilde{\gamma})} + \dot{\theta}_p \left( \frac{\cos \alpha_o}{\cos \alpha_r(\beta_3, \tilde{\gamma})} - 1 \right) \right) \quad (4.179)$$

With the following trigonometric identity,

$$\sin \gamma - \sin \gamma_o = 2 \sin\left(\frac{\tilde{\gamma}}{2}\right) \cos\left(\frac{\gamma + \gamma_o}{2}\right) \quad (4.180)$$

the time derivative  $\dot{V}_2(\beta_3, \tilde{\gamma})$  is expressed as follows:

$$\begin{aligned} \dot{V}_2(\beta_3, \tilde{\gamma}) &= \frac{4c_2 v_p \hat{f}'_{yr}(\beta_3, \tilde{\gamma})}{L \cos \alpha_r(\beta_3, \tilde{\gamma})} \frac{\tilde{\gamma}}{2} \sin\left(\frac{\tilde{\gamma}}{2}\right) \cos\left(\gamma_o + \frac{\tilde{\gamma}}{2}\right) \\ &\quad + c_2 \dot{\theta}_p \left( \frac{\cos \alpha_o}{\cos \alpha_r(\beta_3, \tilde{\gamma})} - 1 \right) \hat{f}'_{yr}(\beta_3, \tilde{\gamma}) \tilde{\gamma} \end{aligned} \quad (4.181)$$

Note that  $\frac{\tilde{\gamma}}{2} \sin\left(\frac{\tilde{\gamma}}{2}\right) > 0$  for  $\tilde{\gamma} \in [-2\pi, 2\pi]$ . Then for  $\cos \alpha_r > 0$  and  $\cos(\gamma_o + \tilde{\gamma}/2) > 0$ , it can be seen that the first term of  $\dot{V}_2(\beta_3, \tilde{\gamma})$  is negative whenever the term  $\hat{f}'_{yr}(\beta_3, \tilde{\gamma})$  is negative, in a similar manner to the function  $\dot{V}_2(\beta_2, \tilde{\gamma})$  from the previous section. There are no guarantees on the sign of the second term of  $\dot{V}_2(\beta_2, \tilde{\gamma})$ , however, so that  $\dot{V}_2(\beta_2, \tilde{\gamma})$  is not guaranteed to be negative semi-definite. Thus  $V_2(\tilde{\beta}, \dot{\beta}_p)$  is not guaranteed to be a Lyapunov function.

Although  $\dot{V}_2(\beta_2, \tilde{\gamma})$  is not negative semi-definite, it is locally negative definite with respect to  $\dot{\beta}_p$  along the axis  $\tilde{\alpha} = 0$  when parameterized in terms of  $(\tilde{\alpha}, \dot{\beta}_p)$  as

$$\dot{V}_2(\tilde{\alpha}, \dot{\beta}_p) = \dot{\beta}_p c_2 (f_{yr}(\alpha_o + \tilde{\alpha}) - f_{yr}(\alpha_o + \tilde{\alpha} + \gamma(\tilde{\alpha}, \dot{\beta}_p) - \gamma_o)) \quad (4.182)$$

and the following conditions are met:

$$\frac{\partial \dot{V}_2}{\partial \dot{\beta}_p}(0,0) = 0 \quad (4.183)$$

$$\frac{\partial^2 \dot{V}_2}{\partial \dot{\beta}_p^2}(0,0) < 0 \quad (4.184)$$

The first condition on  $\partial \dot{V}_2 / \partial \dot{\beta}_p$  can be easily verified by differentiating (4.182) and evaluating at  $(\tilde{\alpha}, \dot{\beta}_p) = (0,0)$ , since  $\gamma(0,0) = \gamma_o$ . The second condition can be evaluated by first computing the quantity  $\partial^2 \dot{V}_2 / \partial \dot{\beta}_p^2$  at  $(\tilde{\alpha}, \dot{\beta}_p) = (0,0)$  by twice differentiating (4.182) and simplifying to the following:

$$\frac{\partial^2 \dot{V}_2}{\partial \dot{\beta}_p^2}(0,0) = -c_2 f'_{yr}(\alpha_o) \frac{\partial \gamma}{\partial \dot{\beta}_p}(0,0) \quad (4.185)$$

With the partial derivative  $\partial \gamma / \partial \dot{\beta}_p$  given as

$$\frac{\partial \gamma}{\partial \dot{\beta}_p}(0,0) = -\frac{L \cos \alpha_o}{v_p \cos \gamma_o} \quad (4.186)$$

the partial derivative  $\partial^2 \dot{V}_2 / \partial \dot{\beta}_p^2$  is simplified to

$$\frac{\partial^2 \dot{V}_2}{\partial \dot{\beta}_p^2}(0,0) = \frac{c_2 L \cos \alpha_o}{v_p \cos \gamma_o} f'_{yr}(\alpha_o) \quad (4.187)$$

and can be seen to be negative when the equilibrium point at  $(\tilde{\alpha}, \dot{\beta}_p) = (0,0)$  is stable according to (4.125).

Although the derivatives of the functions  $V_1(\tilde{\alpha}, \dot{\beta}_p)$  and  $V_2(\tilde{\alpha}, \dot{\beta}_p)$  are not negative semi-definite, it was shown that  $\dot{V}_1(\tilde{\alpha}, \dot{\beta}_p)$  is locally negative definite along the axis  $\dot{\beta}_p = 0$  and that  $\dot{V}_2(\tilde{\alpha}, \dot{\beta}_p)$  is locally negative definite along the axis  $\tilde{\alpha} = 0$ . This suggests that a linear combination of  $V_1(\tilde{\alpha}, \dot{\beta}_p)$  and  $V_2(\tilde{\alpha}, \dot{\beta}_p)$  may have a locally negative definite derivative and satisfy the requirements of a Lyapunov function. The function  $V_3(\tilde{\alpha}, \dot{\beta}_p)$  is defined as a linear combination of  $V_1(\tilde{\alpha}, \dot{\beta}_p)$  and  $V_2(\tilde{\alpha}, \dot{\beta}_p)$  with coefficient  $\lambda \in [0, 1]$  as follows:

$$V_3(\tilde{\alpha}, \dot{\beta}_p) = (1-\lambda)V_1(\tilde{\alpha}, \dot{\beta}_p) + \lambda V_2(\tilde{\alpha}, \dot{\beta}_p) \quad (4.188)$$

$$\begin{aligned} V_3(\tilde{\alpha}, \dot{\beta}_p) &= \frac{1}{2} \dot{\beta}_p^2 + c_2 u_{\theta 3} \sin \beta_p (\tilde{\alpha}, \dot{\beta}_p) - \lambda c_2 u_{\theta 3} \sin \beta_o \\ &\quad - (1-\lambda) c_2 u_{\theta 3} \sin(\beta_p(\tilde{\alpha}, \dot{\beta}_p) - \tilde{\alpha}) \\ &\quad - (1-\lambda) c_2 \int_{\alpha_o}^{\alpha_o + \tilde{\alpha}} f_{yr}(s) ds \\ &\quad - \lambda c_2 \int_{\alpha_o}^{\alpha_o + \tilde{\alpha} + \gamma(\tilde{\alpha}, \dot{\beta}_p) - \gamma_o} f_{yr}(s) ds \end{aligned} \quad (4.189)$$

The function  $V_3(\tilde{\alpha}, \dot{\beta}_p)$  must satisfy the following conditions to be locally positive definite:

$$\frac{\partial V_3}{\partial \tilde{\alpha}}(0,0) = \frac{\partial V_3}{\partial \dot{\beta}_p}(0,0) = 0 \quad (4.190)$$

$$\frac{\partial^2 V_3}{\partial \tilde{\alpha}^2}(0,0) > 0 \quad (4.191)$$

$$\frac{\partial^2 V_3}{\partial \dot{\beta}_p^2}(0,0) > 0 \quad (4.192)$$

$$\frac{\partial^2 V_3}{\partial \tilde{\alpha}^2}(0,0) \frac{\partial^2 V_3}{\partial \dot{\beta}_p^2}(0,0) - \left( \frac{\partial^2 V_3}{\partial \tilde{\alpha} \partial \dot{\beta}_p}(0,0) \right)^2 > 0 \quad (4.193)$$

The condition in (4.190) is satisfied since both  $V_1(\tilde{\alpha}, \dot{\beta}_p)$  and  $V_2(\tilde{\alpha}, \dot{\beta}_p)$  were shown to satisfy similar conditions. Expressions for the second partial derivatives of  $V_3(\tilde{\alpha}, \dot{\beta}_p)$  are given below and should be evaluated numerically for each operating point to verify that the conditions given above are satisfied.

$$\begin{aligned} \frac{\partial^2 V_3}{\partial \tilde{\alpha}^2}(0,0) &= -c_2 u_{\theta 3} \sin \beta_o \left( \left( 1 + \frac{\partial \gamma}{\partial \tilde{\alpha}} \right)^2 - (1 - \lambda) \left( \frac{\partial \gamma}{\partial \tilde{\alpha}} \right)^2 \right) \\ &\quad - c_2 f'_{yr}(\alpha_o) \left( 1 - \lambda + \lambda \left( 1 + \frac{\partial \gamma}{\partial \tilde{\alpha}} \right)^2 \right) \end{aligned} \quad (4.194)$$

$$\frac{\partial^2 V_3}{\partial \dot{\beta}_p^2}(0,0) = 1 - \lambda c_2 \left( \frac{\partial \gamma}{\partial \dot{\beta}_p} \right)^2 (u_{\theta 3} \sin \beta_o + f'_{yr}(\alpha_o)) \quad (4.195)$$

$$\begin{aligned} \frac{\partial^2 V_3}{\partial \tilde{\alpha} \partial \dot{\beta}_p}(0,0) &= -c_2 \frac{\partial \gamma}{\partial \dot{\beta}_p}(0,0) \left( 1 + \lambda \frac{\partial \gamma}{\partial \tilde{\alpha}} \right) u_{\theta 3} \sin \beta_o \\ &\quad - \lambda c_2 \frac{\partial \gamma}{\partial \dot{\beta}_p}(0,0) \left( 1 + \frac{\partial \gamma}{\partial \tilde{\alpha}} \right) f'_{yr}(\alpha_o) \end{aligned} \quad (4.196)$$

The time derivative of  $V_3(\tilde{\alpha}, \dot{\beta}_p)$  can be computed using (4.148) and (4.182) along with the following:

$$\dot{V}_3(\tilde{\alpha}, \dot{\beta}_p) = (1 - \lambda) \dot{V}_1(\tilde{\alpha}, \dot{\beta}_p) + \lambda \dot{V}_2(\tilde{\alpha}, \dot{\beta}_p) \quad (4.197)$$

The time derivative of  $V_3(\tilde{\alpha}, \dot{\beta}_p)$  is locally negative definite if it satisfies the following conditions:

$$\frac{\partial \dot{V}_3}{\partial \tilde{\alpha}}(0,0) = \frac{\partial \dot{V}_3}{\partial \dot{\beta}_p}(0,0) = 0 \quad (4.198)$$

$$\frac{\partial^2 \dot{V}_3}{\partial \tilde{\alpha}^2}(0,0) < 0 \quad (4.199)$$

$$\frac{\partial^2 \dot{V}_3}{\partial \dot{\beta}_p^2}(0,0) < 0 \quad (4.200)$$

$$\frac{\partial^2 \dot{V}_3}{\partial \tilde{\alpha}^2}(0,0) \frac{\partial^2 \dot{V}_3}{\partial \dot{\beta}_p^2}(0,0) - \left( \frac{\partial^2 \dot{V}_3}{\partial \tilde{\alpha} \partial \dot{\beta}_p}(0,0) \right)^2 > 0 \quad (4.201)$$

The first condition is satisfied since  $\dot{V}_1(\tilde{\alpha}, \dot{\beta}_p)$  and  $\dot{V}_2(\tilde{\alpha}, \dot{\beta}_p)$  satisfy a similar condition. The other conditions can be evaluated using (4.154)-(4.155), (4.157)-(4.158), (4.187), and the following expressions for the partial derivatives:

$$\frac{\partial^2 \dot{V}_1}{\partial \dot{\beta}_p^2}(0,0) = -2 \frac{L \cos(\alpha_o)}{v_r(0,0)} \left( \frac{\partial \ddot{\beta}_p}{\partial \dot{\beta}_p}(0,0) + 2 \frac{\partial A_1}{\partial \dot{\beta}_p}(0,0) \right) \left( \frac{\partial \ddot{\beta}_p}{\partial \dot{\beta}_p}(0,0) + 2 \frac{\partial A_2}{\partial \dot{\beta}_p}(0,0) \right) \quad (4.202)$$

$$\begin{aligned} \frac{\partial^2 \dot{V}_1}{\partial \tilde{\alpha} \partial \dot{\beta}_p}(0,0) &= - \frac{L \cos(\alpha_o)}{v_r(0,0)} \left( \frac{\partial \ddot{\beta}_p}{\partial \tilde{\alpha}}(0,0) + 2 \frac{\partial A_1}{\partial \tilde{\alpha}}(0,0) \right) \left( \frac{\partial \ddot{\beta}_p}{\partial \dot{\beta}_p}(0,0) + 2 \frac{\partial A_2}{\partial \dot{\beta}_p}(0,0) \right) \\ &\quad - \frac{L \cos(\alpha_o)}{v_r(0,0)} \left( \frac{\partial \ddot{\beta}_p}{\partial \dot{\beta}_p}(0,0) + 2 \frac{\partial A_1}{\partial \dot{\beta}_p}(0,0) \right) \left( \frac{\partial \ddot{\beta}_p}{\partial \tilde{\alpha}}(0,0) + 2 \frac{\partial A_2}{\partial \tilde{\alpha}}(0,0) \right) \end{aligned} \quad (4.203)$$

$$\frac{\partial \ddot{\beta}_p}{\partial \dot{\beta}_p}(0,0) = -c_2 u_{\theta 3} \sin \beta_o \frac{L \cos \alpha_o}{v_p \cos \gamma_o} \quad (4.204)$$

$$\frac{\partial A_1}{\partial \dot{\beta}_p}(0,0) = \frac{1}{2} \dot{\theta}_p \tan \alpha_o \quad (4.205)$$

$$\frac{\partial A_2}{\partial \dot{\beta}_p}(0,0) = 0 \quad (4.206)$$

$$\frac{\partial^2 \dot{V}_2}{\partial \tilde{\alpha}^2}(0,0) = 0 \quad (4.207)$$

$$\frac{\partial^2 \dot{V}_2}{\partial \tilde{\alpha} \partial \dot{\beta}_p^2}(0,0) = c_2 f'_{yr}(\alpha_o) \frac{L \dot{\theta}_p \sin \alpha_o}{v_p \cos \gamma_o} \quad (4.208)$$

These conditions can be evaluated numerically at each operating point to determine the range of  $\lambda$  for which  $V_3(\tilde{\alpha}, \dot{\beta}_p)$  is a Lyapunov function. Additionally, the basin of attraction can be estimated by numerically computing the regions of the state space for which  $\dot{V}_3(\tilde{\alpha}, \dot{\beta}_p)$  is negative. Several examples are provided below using the tire parameters given in Chapter 2, along with simulation results to verify the stability claims.

The first example is a moderate acceleration turn  $u_{\theta 3} = 0.1$  at a low speed of  $v_p = 5$  m/s with  $u_3 = 0$ . It can be seen in Fig. 4.9 that this acceleration is low enough that only one equilibrium point exists for rear slip angles  $\alpha_r \in [-\pi/2, \pi/2]$ . At this speed, the equilibrium values of the slip angles are  $\alpha_o = -0.80$  deg,  $\gamma_o = 6.39$  deg, and  $\beta_o = 5.59$  deg. This speed corresponds to a non-dimensional speed of  $Fr = 0.94$ , which can be seen in Fig. 4.11 to be sufficient to guarantee stability of the equilibrium point. Additionally, it can be shown numerically that the function  $V_3(\tilde{\alpha}, \dot{\beta}_p)$  is a Lyapunov function for  $\lambda \in [\lambda_o, 1-\lambda_o]$  with  $\lambda_o = 10^{-4}$ . For a value of  $\lambda = 0.01$ , the contours of  $V_3(\tilde{\alpha}, \dot{\beta}_p)$  and a numerical estimate of the range of states for which  $\dot{V}_3(\tilde{\alpha}, \dot{\beta}_p) \leq 0$  are illustrated in Fig. 4.12.

It can be seen that the nonzero value of  $u_{\theta 3}$  causes asymmetry in the contours of the Lyapunov function  $V_3(\tilde{\alpha}, \dot{\beta}_p)$ . It can also be seen that there is a region near  $\tilde{\alpha} = -90$  deg for which  $\dot{V}_3(\tilde{\alpha}, \dot{\beta}_p) > 0$ . Since no other regions were found in this area of the state space for which  $\dot{V}_3(\tilde{\alpha}, \dot{\beta}_p) > 0$ , this is highly suggestive, though not a rigorous proof, that  $\dot{V}_3(\tilde{\alpha}, \dot{\beta}_p) < 0$  for a large range of the state space for this operating condition, which would imply asymptotic stability of the equilibrium point. As with the controller for straight line driving, the basin of attraction illustrated in Fig. 4.12 is unlikely to be achieved in practice, since actuator constraints limit the range of states for which the tire force controller can be implemented.

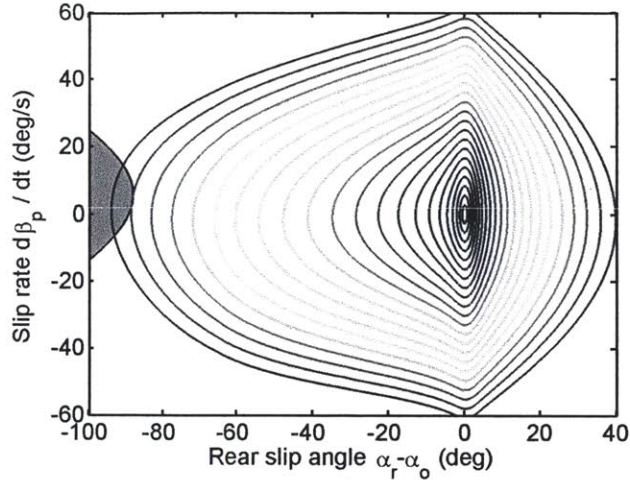


Fig. 4.12. Contours of Lyapunov function  $V_3(\tilde{\alpha}, \dot{\beta}_p)$  are illustrated for  $u_{\theta 3} = 0.1$ ,  $v_p = 5$  m/s, and  $u_3 = 0$ . One region of the state space was found near  $\tilde{\alpha} = -90$  deg for which  $\dot{V}_3(\tilde{\alpha}, \dot{\beta}_p) > 0$ , and this region is darkened.

At a higher speed of  $v_p = 35$  m/s with  $u_{\theta 3} = 0.1$  and  $u_3 = 0$ , the stability analysis is very similar. At this higher speed, the equilibrium slip angles are  $\alpha_o = -0.81$  deg,  $\gamma_o = 0.13$  deg, and  $\beta_o = -0.68$  deg. Again, the acceleration and speed  $Fr = 6.63$  are sufficient for a single stable equilibrium point to exist for rear slip angles  $\alpha_r \in [-\pi/2, \pi/2]$ . It can also be shown numerically that the function  $V_3(\tilde{\alpha}, \dot{\beta}_p)$  is a Lyapunov function for  $\lambda \in [\lambda_o, 1-\lambda_o]$  with  $\lambda_o = 10^{-4}$ . With  $\lambda = 0.01$ , the contours of  $V_3(\tilde{\alpha}, \dot{\beta}_p)$  and range of states for which  $\dot{V}_3(\tilde{\alpha}, \dot{\beta}_p) \leq 0$  are similar to the case with  $v_p = 5$  m/s illustrated in Fig. 4.12.

These stability properties are demonstrated by simulating the dynamics given in (4.61)-(4.62) with these operating conditions. The initial conditions are given as  $\tilde{\alpha}(0) = -20$  deg and  $\dot{\beta}_p(0) = 0$ . The simulated time responses of  $\tilde{\alpha}$  and  $\dot{\beta}_p$  are shown in Fig. 4.14. A phase plane plot with phase variables  $\tilde{\alpha}$  and  $\dot{\beta}_p$  and the Lyapunov function value  $V_3(\tilde{\alpha}, \dot{\beta}_p)$  are shown in Fig. 4.15.

For both speeds, the slip angle  $\tilde{\alpha}$ , slip rate  $\dot{\beta}_p$ , and Lyapunov function value  $V_3(\tilde{\alpha}, \dot{\beta}_p)$  converge to zero. Again, the inverse relationship between damping and speed is evident in the rate of decrease of the Lyapunov function value and the oscillations at

higher speed. Whereas the straight-line trajectories exhibited a roughly linear decrease in the Lyapunov function value, the steady turning trajectories exhibit periods of slow decrease when  $\tilde{\alpha}$  is large followed by periods of rapid decrease when  $\tilde{\alpha}$  approaches the equilibrium value of 0.

It can also be seen that the phase plane trajectories closely follow the contours of the Lyapunov function at high speed. This indicates that the Lyapunov function may be used to predict the behavior of future trajectories, including the peak value of slip.

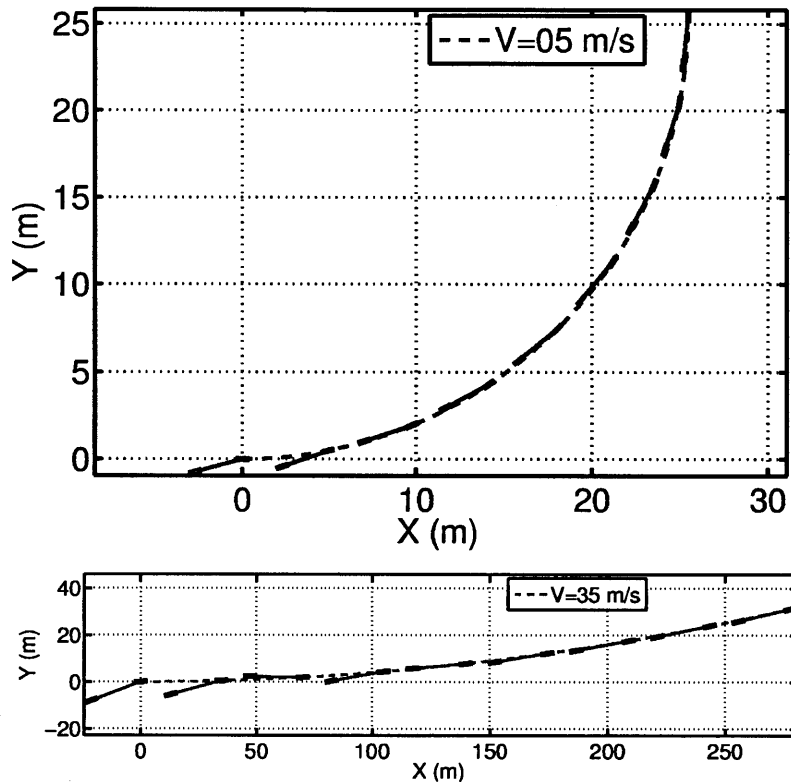


Fig. 4.13. Snapshots at 1 second intervals of vehicle orientation while tracking steady turning trajectories at constant speed with  $u_{\theta_3} = 0.1$  and  $u_3=0$ . The vehicle size is enlarged and not to scale in the illustration of the 35 m/s trajectory to improve visibility.

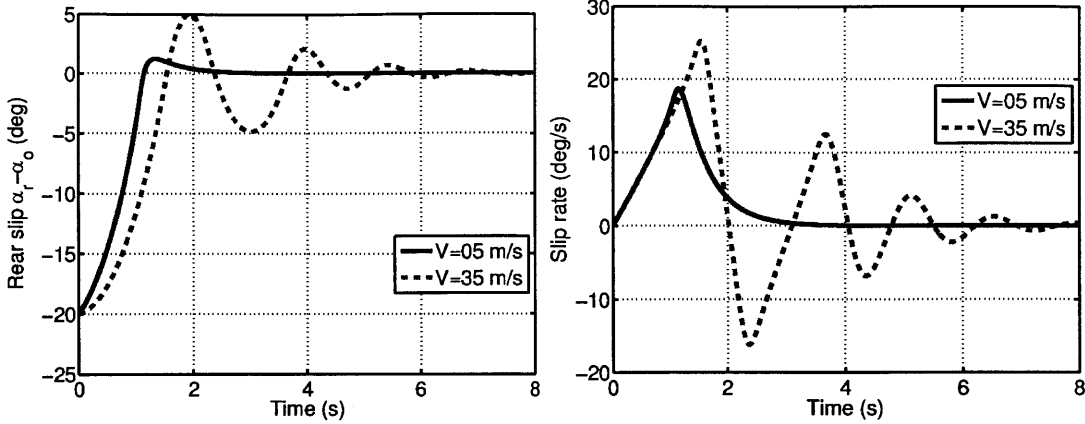


Fig. 4.14. Rear slip angle error  $\tilde{\alpha}$  and slip rate  $\dot{\beta}_p$  during steady turning trajectory at constant speed with  $u_{\theta 3} = 0.1$  and  $u_3 = 0$ .

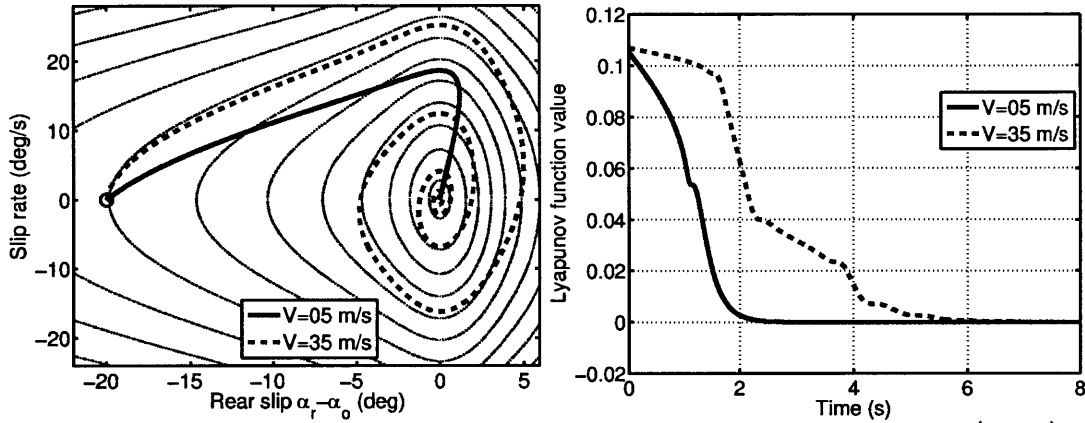


Fig. 4.15. Phase plane plot of yaw dynamics and Lyapunov function value  $V_3(\tilde{\alpha}, \dot{\beta}_p)$  during steady turning trajectory at constant speed with  $u_{\theta 3} = 0.1$  and  $u_3 = 0$ . In the phase plane plot, contours of the Lyapunov function  $V_3(\tilde{\alpha}, \dot{\beta}_p)$  for  $v_p=5\text{ m/s}$  are included in the background.

Since there are no other equilibrium points for  $\alpha_r \in (-\pi/2, \pi/2)$ , the primary limit on the basin of attraction for the yaw dynamics is imposed by limits on the actuators used to apply the control laws for  $u_1$  and  $u_2$ . The steering angle  $\delta$  and front longitudinal force  $F_{xf}$  used to apply  $u_1$  and  $u_2$  for the simulations shown in Figs. 4.14-4.15 are plotted in Fig. 4.16. At 35 m/s, the peak steering angle occurs near the initial slip angle of 20 deg and has an equilibrium steering angle of about 0.5 deg. At 5 m/s, the peak steering angle is near 14 deg, with an equilibrium value of 6.5 deg. The peak value of  $F_{xf}$  is less than 0.06  $F_z$  at each speed.

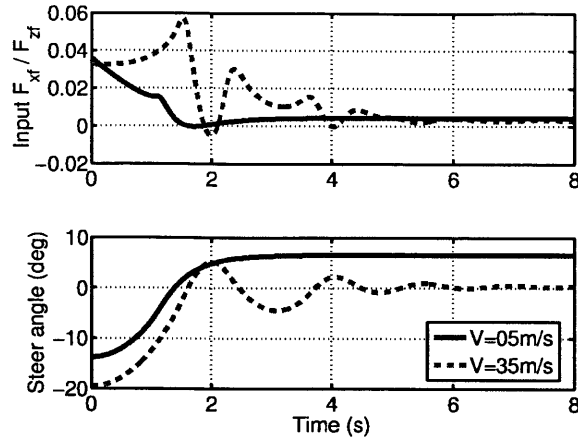


Fig. 4.16. Steering angle and front traction/braking force  $F_{xf}$  inputs while tracking steady turning trajectory at constant speed with  $u_{\theta_3} = 0.1$  and  $u_3 = 0$  and an initial slip angle of  $\tilde{\alpha} = -20$  deg.

For a higher acceleration turn with  $u_{\theta_3} = 0.2$ , multiple equilibrium points can exist for rear slip angles  $\alpha_r \in [-\pi/2, \pi/2]$ . At a speed of  $v_p = 5$  m/s with  $u_3 = 0$ , equilibrium rear slip angles exist at  $\alpha_o = -1.76$  deg,  $-9.40$  deg, and  $-43.3$  deg. The equilibrium point at  $\alpha_r = -1.76$  deg is stable and has corresponding equilibrium slip angles of  $\gamma_o = 12.9$  deg and  $\beta_o = 11.1$  deg. It can be shown numerically that the function  $V_3(\tilde{\alpha}, \dot{\beta}_p)$  is a Lyapunov function for  $\lambda \in [\lambda_o, 1-\lambda_o]$  with  $\lambda_o = 10^{-3}$ . For a value of  $\lambda = 0.01$ , the contours of  $V_3(\tilde{\alpha}, \dot{\beta}_p)$  and a numerical estimate of the range of states for which  $\dot{V}_3(\tilde{\alpha}, \dot{\beta}_p) \leq 0$  are illustrated in Fig. 4.17.

It can be seen that the unstable equilibrium point near  $-7.5$  deg causes a saddle point in the Lyapunov function  $V_3(\tilde{\alpha}, \dot{\beta}_p)$ . It can also be seen that there are two regions for which  $\dot{V}_3(\tilde{\alpha}, \dot{\beta}_p) > 0$ . An estimate of the basin of attraction for this operating point is the contour of  $V_3(\tilde{\alpha}, \dot{\beta}_p)$  that intersects the saddle point and contains the stable equilibrium since no regions for which  $\dot{V}_3(\tilde{\alpha}, \dot{\beta}_p) > 0$  were found in this contour. Again, this is suggestive of the basin of attraction for which the equilibrium point is asymptotically stable, though not a rigorous proof.

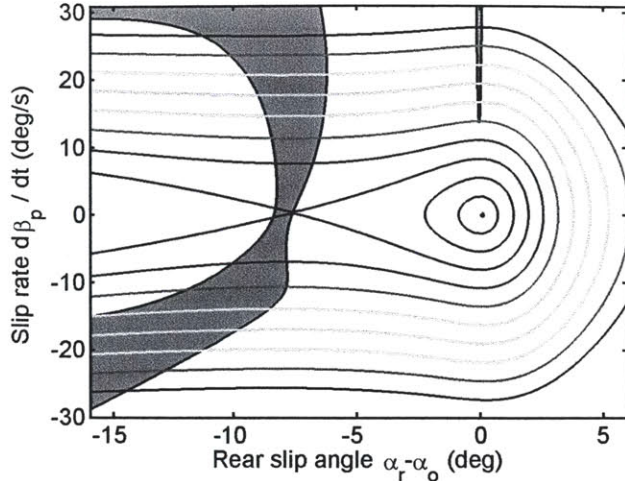


Fig. 4.17. Contours of Lyapunov function  $V_3(\tilde{\alpha}, \dot{\beta}_p)$  are illustrated for  $u_{\theta 3} = 0.2$ ,  $v_p = 5$  m/s, and  $u_3 = 0$ . Two regions of the state space were found for which  $\dot{V}_3(\tilde{\alpha}, \dot{\beta}_p) > 0$ , and these regions are darkened.

At a higher speed of  $v_p = 35$  m/s with  $u_{\theta 3} = 0.2$  and  $u_3 = 0$ , the stability analysis is similar. At this higher speed, the equilibrium slip angles exist at  $\alpha_o = -1.81$  deg,  $-9.74$  deg, and  $-34.3$  deg. The equilibrium at  $\alpha_o = -1.81$  deg is stable and has corresponding equilibrium slip angles of  $\gamma_o = 0.26$  deg, and  $\beta_o = -1.55$  deg. It can be shown numerically that the function  $V_3(\tilde{\alpha}, \dot{\beta}_p)$  is a Lyapunov function for  $\lambda \in [\lambda_o, 1-\lambda_o]$  with  $\lambda_o = 10^{-4}$ . With  $\lambda = 0.01$ , the contours of  $V_3(\tilde{\alpha}, \dot{\beta}_p)$  and range of states for which  $\dot{V}_3(\tilde{\alpha}, \dot{\beta}_p) \leq 0$  are illustrated in Fig. 4.18.

At this speed, one region was identified for which  $\dot{V}_3(\tilde{\alpha}, \dot{\beta}_p) > 0$ . An estimate of the basin of attraction for this operating point is the largest contour of the Lyapunov function  $V_3(\tilde{\alpha}, \dot{\beta}_p)$  inside which  $\dot{V}_3(\tilde{\alpha}, \dot{\beta}_p) \leq 0$ . Again, this is suggestive of the basin of attraction for which the equilibrium point is asymptotically stable, though not a rigorous proof.

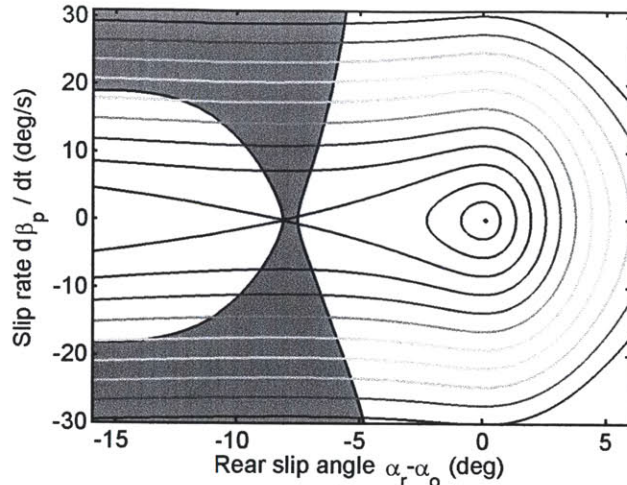


Fig. 4.18. Contours of Lyapunov function  $V_3(\tilde{\alpha}, \dot{\beta}_p)$  are illustrated for  $u_{\theta 3} = 0.2$ ,  $v_p = 35$  m/s, and  $u_3 = 0$ . One region of the state space was found for which  $\dot{V}_3(\tilde{\alpha}, \dot{\beta}_p) > 0$ , and this region is darkened.

These stability properties are demonstrated by simulating the dynamics given in (4.61)-(4.62) with these operating conditions. The initial conditions are given as  $\tilde{\alpha}(0) = -7$  deg and  $-9$  deg and  $\dot{\beta}_p(0) = 0$ . A phase plane plot with phase variables  $\tilde{\alpha}$  and  $\dot{\beta}_p$  and the Lyapunov function value  $V_3(\tilde{\alpha}, \dot{\beta}_p)$  are shown in Fig. 4.19. It can be seen that the trajectories starting from  $\tilde{\alpha} = -7$  deg converge to the stable equilibrium point, while the trajectories starting from  $\tilde{\alpha} = -9$  deg diverge.

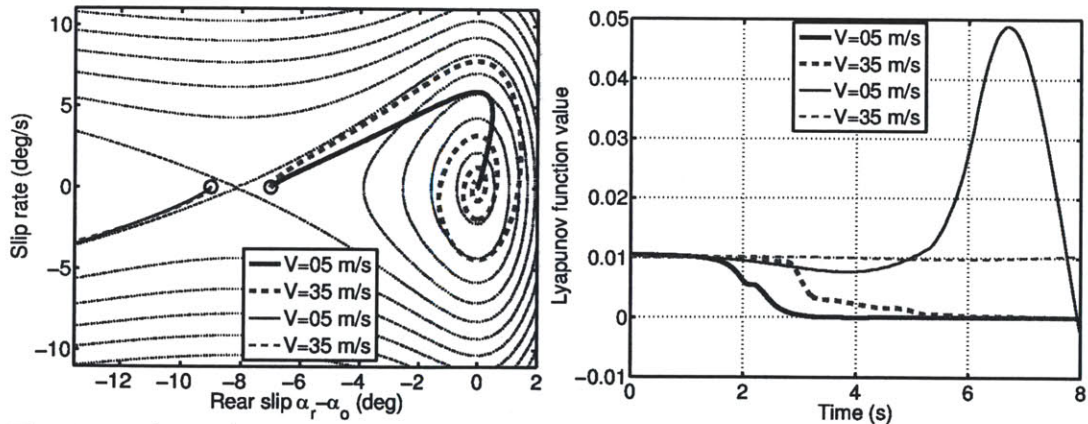


Fig. 4.19. Phase plane plot of yaw dynamics and Lyapunov function value during steady turning trajectory at constant speed with  $u_{\theta}=0.2$  and  $u_3=0$ . In the phase plane plot, contours of the Lyapunov function for  $v_p=5$  m/s are included in the background.

#### 4.2.4 Stability of yaw dynamics during time-varying maneuvers

The stability results of the previous sections may be extended to consider time-varying maneuvers, though a stability proof is not considered here. Instead, simulation results are presented here for a maneuver corresponding to the optimal non-passing turn described in Chapter 3. The combined steering and deceleration trajectory is simulated that consists of a constant value of the global acceleration  $\ddot{x}_p$  applied for a fixed period, followed by a drop of the acceleration to zero. The path and accelerations are shown in Figs. 4.20-4.21.

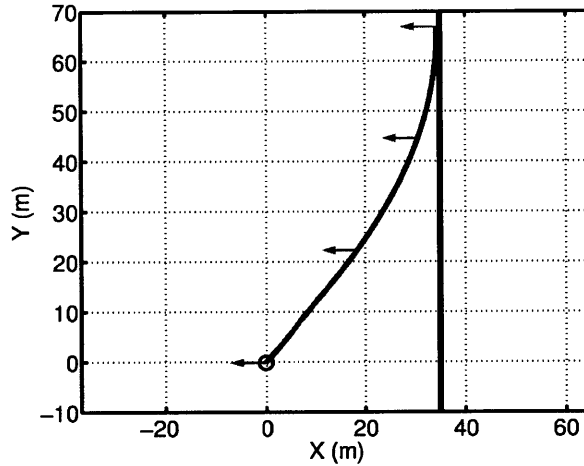


Fig. 4.20. Path taken during optimal non-passing combined braking and turning maneuver.

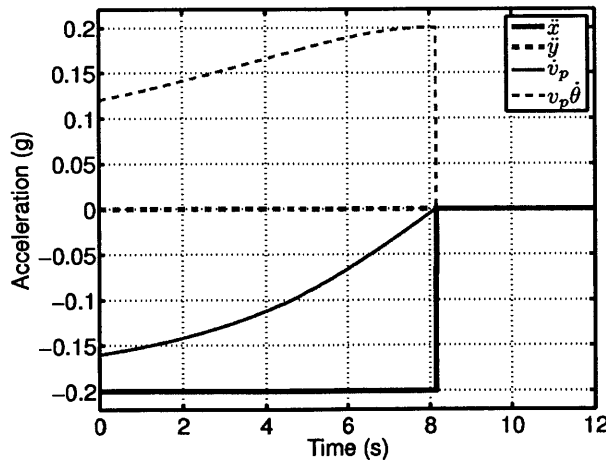


Fig. 4.21. Acceleration of reference path during optimal non-passing combined turning and braking maneuver.

The response of the yaw dynamics are evaluated for an initial speed of 20 m/s and initial yaw angles that deviate 5 deg, 0 deg, and -5 deg from the initial heading of the path. This trajectory is simulated from multiple initial conditions to demonstrate the convergence properties during the time varying maneuver. The response of the yaw dynamics is given in Figs. 4.22. It can be seen that the behavior of the yaw dynamics converge to a single response for these initial conditions. The discontinuity in the desired acceleration caused a jump in the system energy, though the system maintained convergence.

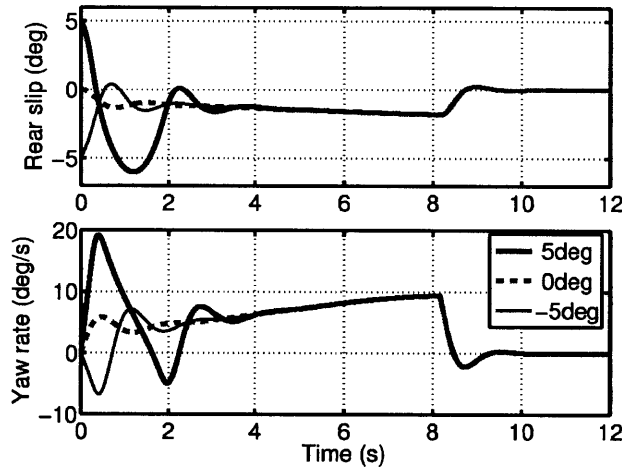


Fig. 4.22. Slip angle and yaw rate response during optimal non-passing combined braking and turning maneuver.

This reference trajectory was also simulated with a high-fidelity vehicle model using the MSC.ADAMS software package, which is a multi-body simulation package commonly used for simulating vehicle dynamics in the automotive industry [10]. The control law for  $u_1$ ,  $u_2$ , and  $u_3$  was implemented using a controller with front steering rate and wheel torques inputs and acceleration feedback. The tire model has a friction coefficient of 0.5. The path, acceleration, and yaw dynamic responses are shown in Fig. 4.23-4.25. It can be seen that the vehicle tracks the desired accelerations with stable yaw dynamics.

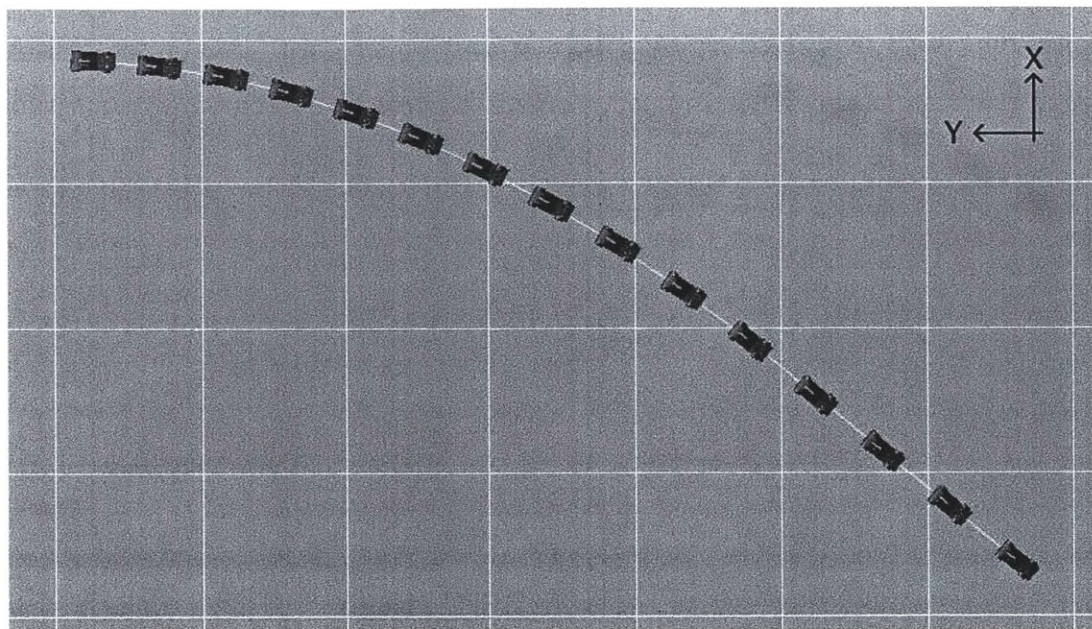


Fig. 4.23. Path taken during optimal non-passing combined braking and turning maneuver with high-fidelity model.

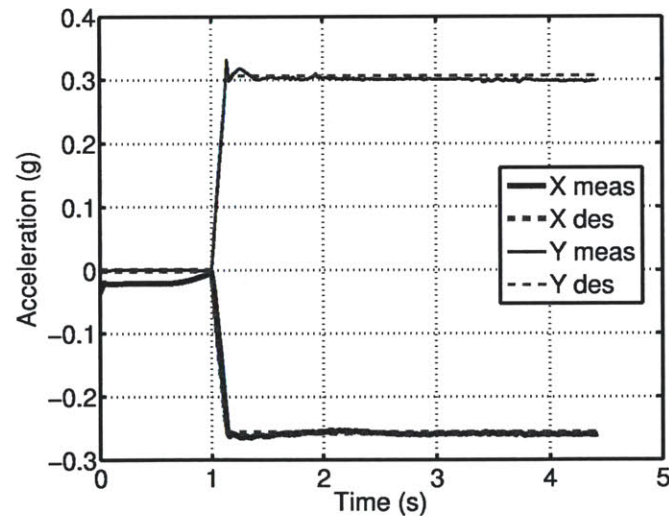


Fig. 4.24. Measured (meas) and desired (des) accelerations during optimal non-passing combined turning and braking maneuver with high-fidelity model.

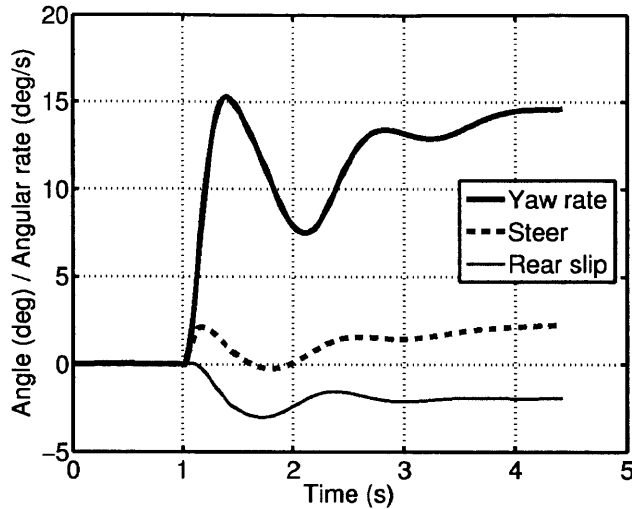


Fig. 4.25. Yaw rate, steer angle, and slip angle response during optimal non-passing combined braking and turning maneuver with high-fidelity model.

#### 4.2.5 Summary

In this section, structure was identified in the yaw dynamics corresponding to a Liénard system. Stability conditions were established for the tracking straight-line and steady turning trajectories based on a Lyapunov stability analysis. Limits on the basin of attraction for these trajectories are imposed by limits on the actuators applying the control laws for  $u_1$  and  $u_2$ , as well as the presence of unstable equilibrium points near the origin. These stability conditions were verified with simulation results. Additionally, the yaw response to a time-varying trajectory based on the optimal non-passing turn from Chapter 3 was simulated, though a general stability proof was not given for time-varying maneuvers.

### 4.3 Discussion

The flatness-based controller presented in Section 4.1 maps the bicycle model into a point mass located at the front center of oscillation with an additional degree of freedom corresponding to the yaw dynamics. Additionally, there is a control law for  $u_3$  that maps the front friction circle constraint into an acceleration circle constraint. This analogy was demonstrated by tracking an optimal non-passing maneuver for the point mass with the bicycle.

Controlling the front center of oscillation provides an advantage over previous work, which used the rear center of oscillation as a flat output and required additional

smoothness of the reference trajectory [28, 64]. This work also provides an improvement over the decoupling controller proposed by Ackermann in that it provides a global trajectory tracking controller rather than controlling the lateral acceleration in a body-fixed frame. Additionally, this work includes a nonlinear analysis of the stability of the yaw dynamics, while Ackerman provided only a linear stability analysis [1].

The flatness-based controller requires an intermediate controller that uses front-wheel steering and traction/braking torques at the front and rear wheels to control the tire forces. Such a controller was implemented using backstepping and acceleration feedback, as described in Appendix X.

Structure in the yaw dynamics was identified that resembles a second order mechanical system when parameterized in terms of the slip angle  $\beta_p$  and slip rate  $\dot{\beta}_p$  and a Liénard system when parameterized in terms of the rear slip angle  $\alpha_r$  and slip rate  $\dot{\beta}_p$ . Candidate Lyapunov functions inspired by this structure in the dynamics were evaluated for straight-line driving and constant radius turns. For straight-line driving, the Lyapunov function based on the Liénard analogy in (4.86) can prove convergence of the yaw dynamics to the stable equilibrium point at the origin of the state space for  $\cos \alpha_r > 0$ . For constant radius turns, a Lyapunov function may be found to guarantee stability when the inputs  $v_p \dot{\theta}_p$  and  $u_3$  are constant and small enough that a stable equilibrium point exists near the origin. The function  $V_3(\tilde{\alpha}, \dot{\beta}_p)$  given in (4.189) can be shown to be a Lyapunov function provided that the conditions given in (4.191)-(4.193) and (4.199)-(4.201) are satisfied for the given value of  $\lambda$ . An approximation of the basin of attraction of the stable equilibrium point can be computed numerically based on the range of states for which the time derivative  $\dot{V}_3(\tilde{\alpha}, \dot{\beta}_p)$  is negative semi-definite. Further study is needed to characterize the behavior of the yaw dynamics while tracking time-varying trajectories.

When the values of  $\dot{v}_p$ ,  $v_p \dot{\theta}_p$ , and  $u_3$  are large enough, an unstable equilibrium point may be created near the origin, or the stable equilibrium point may even be destroyed. The unstable equilibrium points may correspond to high-slip aggressive maneuvers performed by expert drivers, such as drifting or trail-braking [18].

It was noted that the Lyapunov function used to assess the stability of the yaw dynamics resembles an energy function. This suggests that it may be possible to design an energy shaping controller that could change the location and stability properties of equilibrium points. This will be considered in future work.

#### **4.4 Conclusion**

The analysis presented in this chapter allows the trajectory planning problem for a nonlinear bicycle model to be reduced to that of planning for a point mass with an additional degree of freedom. The yaw dynamics were shown to have conditional stability, depending on the magnitude of applied accelerations and rear longitudinal force  $u_3$ . An analysis of the yaw dynamics has also provided insight into the behavior of vehicle dynamics at high slip angles and identified structure in the dynamics that may be exploited for future work in controlling the vehicle during aggressive high-slip maneuvers.

# 5

## CHAPTER 5: VEHICLE CONTROL FOR SAFETY APPLICATION

### **5.1 Introduction**

In this chapter, the contributions of the previous chapters are applied to a driver assistance system for vehicle safety. The system allows drivers full control authority in benign situations, but intervenes when danger is significant. Such a system is termed a semi-autonomous hazard avoidance system. A block diagram of the proposed system is shown in Fig. 5.1.

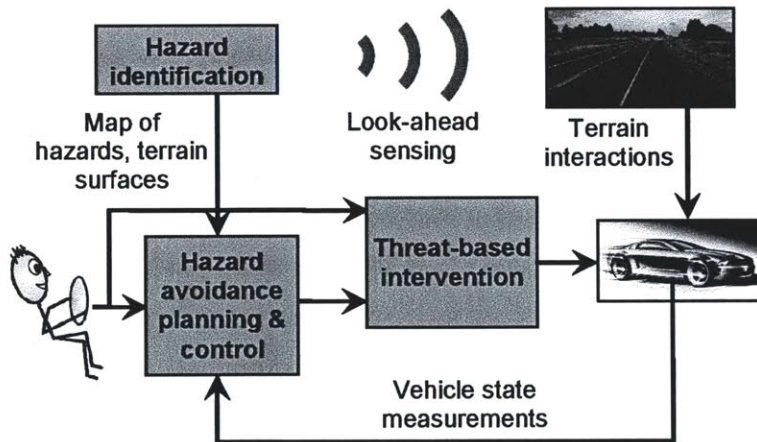


Fig. 5.1: Semi-autonomous hazard avoidance system design.

Here it is assumed that a perception system generates a map of drivable terrain surfaces and hazards around the vehicle. The map is used to plan optimal avoidance trajectories for the bicycle model, as described in Chapter Two. Depending on the nearness to infeasibility of the optimal trajectory, control authority is switched between the driver and a controller for tracking the avoidance trajectory. The control authority switching is designed such that the driver is given full control authority when avoidance can be achieved without approaching the limits of handling, while the hazard avoidance controller is engaged when a limit handling maneuver is required.

The computational demands are high for solving optimal trajectories for the bicycle model numerically. To reduce the computational demands, the results of Chapters Three and Four are used to apply point mass avoidance maneuvers to the bicycle model at the front center of oscillation, which allows the system to be implemented in real-time. This chapter provides details of the subsystems involved as well as simulation and experimental results that demonstrate the performance of the system.

## 5.2 **Semi-autonomous system description**

The semi-autonomous hazard avoidance system consists of subsystems for sensing, planning optimal avoidance trajectories, control authority switching, and vehicle control. Details of these subsystems are provided in the following sections.

### 5.2.1 **Sensing and hazard geometry assumptions and definition**

It is assumed that a map of the environment with hazard locations is available.  $N$  hazards in the environment are represented by polygons  $P_1, P_2, \dots, P_N$ . Each hazard polygon  $P_i$  consists of  $n_i$  nodes  $\mathbf{p}_{ij}, j \in 1-n_i$ . For this work, all hazards are assumed to be fixed, though moving hazards could be considered if the displacement and orientation of each hazard as a function of time was known or could be estimated.

An example map is given in Fig. 5.2, with road edges represented by  $P_1$  and  $P_2$  and a single hazard represented by  $P_3$ . The vehicle geometry is approximated as a circle of radius  $r$  that is centered at point  $c$ . It is assumed that point  $c$  lies on the centerline of the vehicle a distance  $x_c$  from the vehicle c.g., as shown on the right subfigure of Fig. 5.2. The parameters  $x_c$  and  $r$  should be chosen so that the front corners of the vehicle are within the circle. For forward travel, a single circle may suffice for approximating the vehicle shape if the vehicle is not slipping excessively.

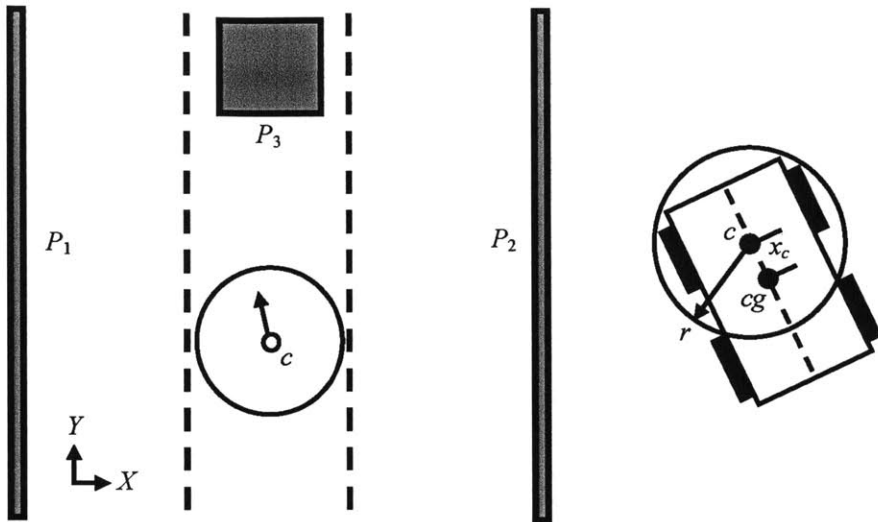


Fig. 5.2: Example hazard avoidance scenario. Road edge hazards are given as polygons,  $P_1$ ,  $P_2$ , and an additional hazard in the road  $P_3$ . The vehicle is approximated by a circle of radius  $r$  at point  $c$ .

If the minimum distance from point  $c$  to the nearest hazard polygon is given by  $h(\mathbf{x})$ , hazard avoidance can be assured by maintaining a clearance of at least  $r$  between point  $c$  and the nearest hazard polygon.

### 5.2.2 Optimal trajectory planning and control

The motion planning subsystem computes optimal avoidance trajectories that minimize nearness to the front friction circle constraint of the bicycle model, as described in Chapter Two. The optimal trajectories are computed numerically in a receding-horizon fashion using model predictive control (MPC). An advantage of MPC is that its computation yields both the optimal motion plan and corresponding control inputs, though the computation is typically demanding. To mitigate computational demands, the results of Chapters Three and Four are applied, as shown below.

The optimal planning problem to be solved is based on equations (26)-(32) in Chapter Two. These equations are discretized and solved over  $p$  time-steps with a discrete time step of  $t_s$ . At time  $t_i$ , the state and input are given by  $\mathbf{x}_i$  and  $\mathbf{u}_i$ . The model  $\dot{\mathbf{x}} = f(\mathbf{x}, \mathbf{u})$  is predicted forward over the  $p$  time-steps using Euler integration as shown below.

$$\mathbf{x}_{i+1} = \mathbf{x}_i + t_s f(\mathbf{x}_i, \mathbf{u}_i) \quad (5.1)$$

A practical challenge for implementing MPC is the computational burden associated with long prediction horizons. The length of the prediction horizon is important, since the effect of hazards beyond the prediction horizon is not considered. If the prediction horizon is shorter than the sensor horizon, some sensory information is not used in the cost or control calculations. An approximation of vehicle behavior from the end of the prediction horizon to the maximum sensor range can be used to exploit this information. When used in an optimal control framework, this approximation is commonly known as the "cost-to-go" [59].

Recalling that the optimization problem attempts to minimize the front friction circle utilization, and that the front friction circle constraint can be mapped to a constraint on the magnitude of the acceleration of the front center of oscillation, it can be seen that the acceleration of an avoidance trajectory can be used as a "cost-to-go." This is done by extending the final predicted state  $\mathbf{x}_p$  an additional  $q$  steps with zero input to account for actuator lag. This corresponds to a zero-order hold on the current steering and braking states. Point mass avoidance trajectories are then computed based on the position and velocity of the front center of percussion, as computed from  $\mathbf{x}_{p+q}$ . As shown in Chapter Four, the front center of percussion has position  $[X_p, Y_p]$  and velocity  $[\dot{X}_p, \dot{Y}_p]$  in a global frame, repeated below.

$$\begin{bmatrix} X_{pm} \\ Y_{pm} \end{bmatrix} = \begin{bmatrix} X \\ Y \end{bmatrix} + \frac{I_{zz}}{mx_r} \begin{bmatrix} \cos \psi \\ \sin \psi \end{bmatrix} \quad (5.2)$$

$$\begin{bmatrix} \dot{X}_p \\ \dot{Y}_p \end{bmatrix} = \begin{bmatrix} \cos \psi & -\sin \psi \\ \sin \psi & \cos \psi \end{bmatrix} \begin{bmatrix} v_x \\ v_y + \frac{I_{zz}}{mx_r} \dot{\psi} \end{bmatrix} \quad (5.3)$$

The cost-to-go is based on an extension of the geometric avoidance maneuvers from Chapter Three to consider a circular vehicle as illustrated in Fig. 5.3. The details of computing the acceleration of these maneuvers for a circular vehicle is given in Appendix A. The optimal point mass maneuvers presented in Section 3.4 were not considered in the cost-to-go for this system for reasons of chronology: these experiments were conducted prior to complete derivation of the optimal point mass maneuvers. Though suboptimal, the acceleration of the geometric maneuvers was shown to be within 25% of

the optimal acceleration for a point vehicle and represents a useful approximation of the optimal acceleration.

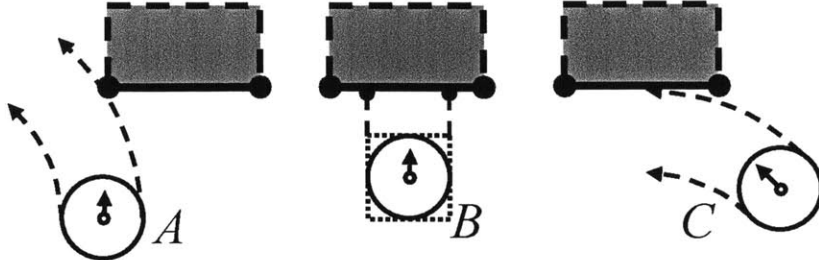


Fig. 5.3: Geometric avoidance maneuvers for circular vehicle. A: Constant radius passing turn. B: Stopping maneuver. C: Constant radius non-passing turn.

The cost-to-go accelerations from Appendix A are given as  $a_1$  for the straight-line stopping maneuver,  $a_2$  for the non-passing turn, and  $a_3$  for the passing turn. Note that the turn accelerations are computed based on whichever turn direction requires less acceleration. No preference is given towards turning left or right other than the required acceleration. The cost function from equation (26) is extended to include the minimum of the cost-to-go accelerations, as shown below. Again no preference is given to a given avoidance maneuver other than the required acceleration.

$$\mathbf{u}^* = \arg \min_{\mathbf{u}} \max \left\{ \max_{i \in A, t} \frac{\sqrt{F_{xf}^2 + F_{yf}^2}}{\mu F_{zf}}, \min \{a_1, a_2, a_3\} \right\} \quad (5.4)$$

### 5.2.3 MPC Implementation details

MPC computation was implemented using the nonlinear optimization package NPSOL. NPSOL uses a sequential quadratic programming algorithm to minimize a smooth nonlinear objective function subject to linear and nonlinear constraints [29]. The solver has the capability to use gradients of the cost and constraint functions to speed convergence. Symbolic derivatives are used in the model prediction, cost function, and constraints of the MPC controller to improve performance.

The prediction horizon length is widely acknowledged to be a critical parameter in the design of model predictive controllers. A long prediction horizon may improve controller stability and performance, though it also increases the computational demand of the controller. Additionally, a challenge of algorithms based on numerical

optimization is avoiding local minima in non-convex problems. The algorithm will converge to a solution that depends on the initial guess of the optimal control vector  $\mathbf{U}^*$ . It has been observed anecdotally in this work that it is more challenging to determine initial guesses that converge to the global minimum for MPC controllers with longer prediction horizons (and hence more control variables) than for controllers with shorter prediction horizons.

An example of this phenomenon is illustrated in Fig. 11. An MPC controller with cost-to-go and a prediction horizon of 1.5 s discretized into 30 timesteps is solved with three different initial guesses of the optimal control vector. These initial guesses result in a stopping maneuver with cost 0.399 and two symmetric passing maneuvers with an initial cost of 0.305.

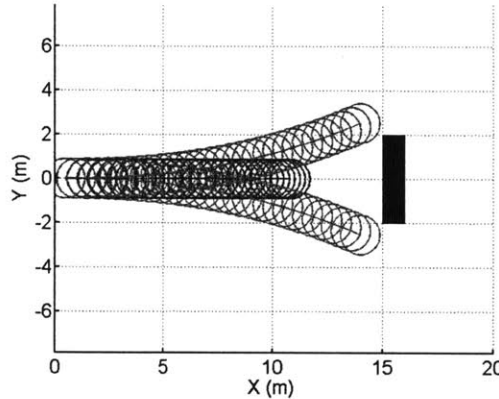


Fig. 5.4: Multiple solutions to MPC control law representing separate local minima.

It has already been noted that the performance of an MPC controller with a long prediction horizon can be approximated by MPC controller with a short prediction horizon and an appropriate cost-to-go, though with the benefit of a reduced computational demand. An additional advantage is the reduced size of the optimization vector, which mitigates the challenge associated with local minima and sensitivity to initial guess of the optimization vector. For these reasons, the MPC controller parameters used in these results are based on a single prediction timestep with the cost-to-go approximating a longer prediction horizon.

### 5.2.4 Cost-based control authority switching

The final aspect of the proposed semi-autonomous hazard avoidance system is control intervention based on the predicted cost  $J^*$ . After the nonlinear MPC controller has computed the predicted cost and input sequence  $\mathbf{u}^*(t)$ , a controller intervention level is determined based on the predicted cost. When the cost is low, the controller intervention is kept low to maximize driver autonomy. As the cost increases above a certain threshold, the system will begin to apply the optimal inputs from  $\mathbf{u}^*$ .

The intervention system reads the driver's current input  $\mathbf{u}_{driver}$ , the MPC input  $\mathbf{u}_{mpc}$ , and the predicted cost  $J^*$ . An intervention gain  $K \in [0,1]$  is computed based on the predicted cost, and is used to determine the applied inputs to the system according to the following equation:

$$\mathbf{u} = K\mathbf{u}_{driver} + (1 - K)\mathbf{u}_{mpc} \quad (5.5)$$

The intervention gain  $K$  may be computed according to a variety of intervention laws, such as a linear function with or without deadband [4]. A switching intervention law with hysteresis is illustrated in Fig. 5.5 and given by the following equation:

$$K(t_i) = \begin{cases} 0 & K(t_{i-1}) = 0, J^*(t_i) \leq \Phi_{on} \\ 1 & K(t_{i-1}) = 0, J^*(t_i) > \Phi_{on} \\ 1 & K(t_{i-1}) = 1, J^*(t_i) \geq \Phi_{off} \\ 0 & K(t_{i-1}) = 1, J^*(t_i) < \Phi_{off} \end{cases} \quad (5.6)$$

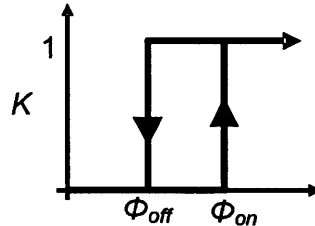


Fig. 5.5: Switching intervention law with hysteresis.

The use of hysteresis in the intervention function prevents small oscillations in the cost function from rapidly switching the intervention gain  $K$ . In practice, this causes the system to wait until cost has reduced below a specific level to return control authority to the driver.

## 5.3 Simulation and Experimental Results

This section presents results of the semi-autonomous hazard avoidance system in simulation and experiments. A description of the experimental setup is provided, followed by results for a stopping maneuver, non-passing turn, and passing turn.

### 5.3.1 Experimental setup

Experimental testing was performed using a 2001 Jaguar S-Type passenger vehicle operated by several human drivers. Driver and actuator steering inputs were coupled via an Active Front Steer (AFS) system [21]. An inertial and GPS navigation system was used to measure vehicle position, sideslip, yaw angle, and yaw rate. Cones were placed in the driving environment to represent hazards, and their location was encoded in the controller as GPS coordinates. A 1 GHz dSPACE™ processor ran controller code and interfaced with steering and braking actuators. With the short prediction horizon and computationally-efficient cost-to-go computation, the controller calculations remained within a 50 ms sampling time. Bicycle model parameters for the test vehicle are given in Table 5.1.

Table 5.1: Model Parameters for simulations and experiments.

Symbol	Description	Value
$m$	Mass	2220 kg
$I_{zz}$	Yaw inertia	3344 kg m <sup>2</sup>
$x_f$	Front axle from c.g.	1.432 m
$x_r$	Rear axle from c.g.	1.472 m
$x_c$	Clearance point	0.10 m
$r$	Clearance radius	0.90 m
$\delta_{max}$	Steering angle limit	10 deg
$u_{brake,max}$	Braking force limit	19600 N
$b_f$	Brake bias	0.507
$C_f$	Front tire cornering stiffness	68 kN/rad
$C_r$	Rear tire cornering stiffness	87 kN/rad

Since magic tire model parameters were unavailable for the experimental vehicle tires and the experiments were conducted on a high-friction surface, the nonlinear tire model from Chapter Two was replaced by a linear tire model. The model is described by the equations below with parameters  $C_f$  and  $C_r$  referred to as the tire cornering stiffnesses and given in Table 5.1. This tire model is suitable for small levels of tire slip and requires only one parameter, reducing the burden of model matching.

$$F_{yf} = -C_f \alpha_f \quad (5.7)$$

$$F_{yr} = -C_r \alpha_r \quad (5.8)$$

It should be noted that the slip angle is undefined at zero speed. As such, all simulations are aborted when the vehicle speed drops below a threshold of 0.5 m/s.

These and some additional parameters for the bicycle model used in this chapter are given in Table 2.1.

The test setup for both the simulations and experiments involved defining a hazard edge in the environment and approaching the edge from a variety of initial conditions. The cost-to-go was computed based on the type of avoidance trajectory that required the minimum level of cost. The preference for different trajectories depends on the hazard location and orientation relative to the vehicle.

A passing maneuver was tested by approaching a hazard face perpendicular to the direction of travel and near the edge, as in Part *A* of Fig. 5.3. A stopping maneuver was tested by approaching a hazard face perpendicular to the direction of travel and far from the edges, as in Part *B* of Fig. 5.3. A non-passing turn was tested by approaching a hazard face with a large skew angle and far from the edges, as in Part *C* of Fig. 5.3.

### 5.3.2 Stopping maneuver

A stopping maneuver was demonstrated by approaching a wide hazard perpendicular to the vehicle direction of travel. Two separate tests were conducted to verify the functionality of the hazard avoidance system. In the first test, a human driver initiated braking to avoid the hazard before the cost exceeded the threshold  $\Phi_{on}$ . This test demonstrates the driver's freedom to operate the vehicle in low-cost situations. In the second test, the human driver approached the hazard without braking so that the vehicle automatically engaged the brakes once the cost exceeds the threshold  $\Phi_{on}$ .

Results from the stopping test without controller intervention are given in Fig. 5.6-5.7. The driver stopped the vehicle before the predicted cost threshold was exceeded.

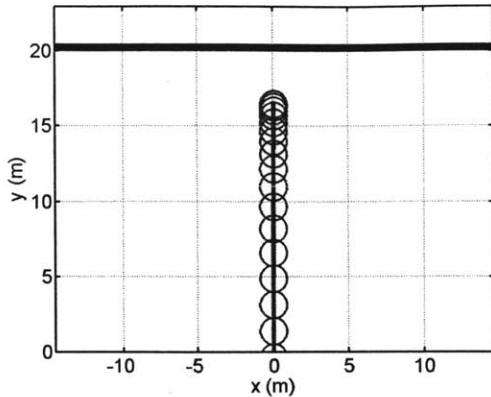


Fig. 5.6: Vehicle path during stopping maneuver initiated by driver without controller intervention. The critical hazard edge is wide and perpendicular to the vehicle direction of travel. The vehicle path is illustrated by the circles plotted at fixed sampling times.

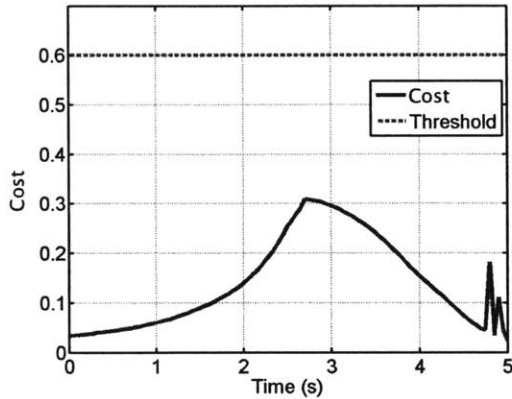


Fig. 5.7: Predicted cost during stopping maneuver initiated by driver without controller intervention. The cost did not exceed the threshold, so the controller did not intervene.

Results of a stopping maneuver with controller intervention are presented below based on simulated and experimental data. Neither the simulated driver nor the human driver in the experiment engaged the brakes and both maintained a constant steering angle. The initial vehicle speed was approximately 8 m/s in both simulation and experiment and the cost threshold was  $\Phi_{on} = 0.3$ . The path, cost, speed, and acceleration from simulation and experiment are presented in Figs. 5.7-5.10. Note that the cost threshold was exceeded at approximately 0.68 s. This is indicated as a solid vertical line labeled "Engage" in Figs. 5.8-5.10.

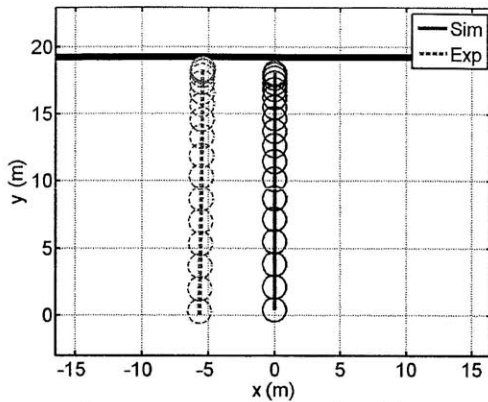


Fig. 5.8: Paths during stopping maneuver at 8 m/s with  $\Phi_{on} = 0.3$ . The critical hazard edge is wide and perpendicular to the vehicle direction of travel. The vehicle path is illustrated by the circles. The simulated path is plotted on the right as solid lines, while the experimental path is plotted on the left as dashed lines.

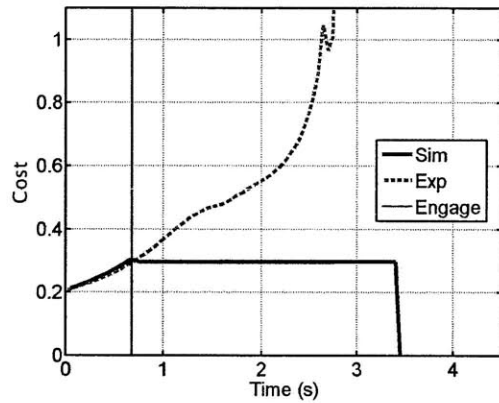


Fig. 5.9: Predicted cost during stopping maneuver at 8 m/s with  $\Phi_{on} = 0.3$ .

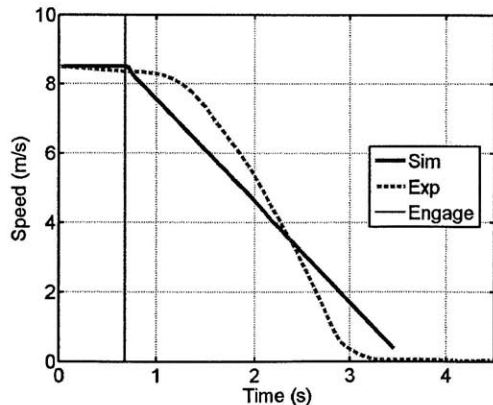


Fig. 5.10: Vehicle speed during stopping maneuver at 8 m/s with  $\Phi_{on} = 0.3$ .

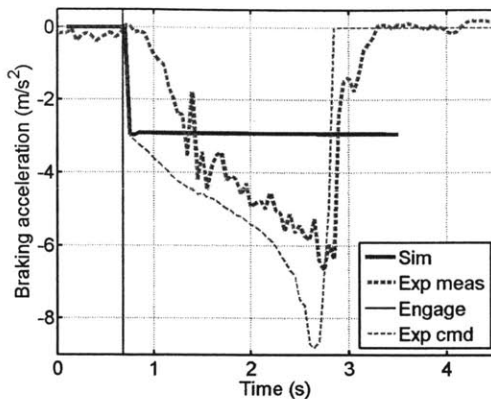


Fig. 5.11: Vehicle braking acceleration during stopping maneuver at 8 m/s with  $\Phi_{on} = 0.3$ .

The simulated acceleration is denoted by "Sim" and the commanded and measured accelerations from the experiment are denoted "Exp cmd" and "Exp meas" respectively.

The simulated vehicle slowed before the hazard edge until the minimum simulation speed of 0.5 m/s was reached. The initial cost was approximately 0.2 and reached the threshold value of  $\Phi_{on} = 0.3$  at approximately 0.68 s. After reaching the predicted cost threshold, the simulated vehicle applied braking quickly and held the predicted cost roughly constant for the duration of the maneuver.

The initial cost and acceleration command for the experimental vehicle matched the simulation data, though a significant lag was observed between the braking command and the measurement of deceleration. This led to an increase in both cost and the braking command magnitude. The vehicle reached the face of the virtual obstacle with a speed of about 1 m/s before stopping 0.2 m past the cones. The controller performance during this test is discussed further in Section 5.4.

### 5.3.3 Passing turn

A passing turn was demonstrated by approaching a hazard corner perpendicular to the hazard face. Similar to the stopping maneuver, tests without controller intervention and with controller intervention are presented.

Results from the passing maneuver without controller intervention are presented in Figs. 5.11-5.12. The initial speed was 12 m/s with threshold  $\Phi_{on} = 0.6$ . The driver initiated a passing maneuver and successfully avoided the obstacle. The cost increased as the driver made the initial turn to the left, then dropped during the transition to between turns, and then increased during the turn to the right.

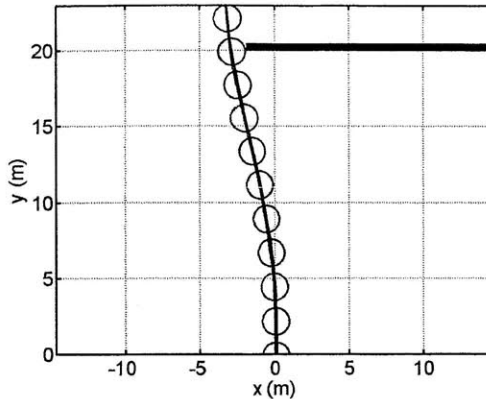


Fig. 5.12: Vehicle path during passing maneuver initiated by driver without controller intervention. The vehicle is near a corner of the hazard and travels perpendicular to the hazard face. The vehicle path is illustrated by the circles.

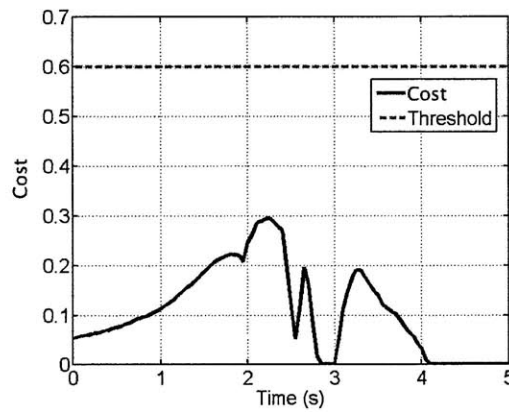


Fig. 5.13: Predicted cost during passing maneuver initiated by driver without intended controller intervention.

Results from the passing maneuver with controller intervention are presented below. Neither the simulated driver nor the human driver engaged the brakes and both maintained a constant steering angle. The vehicle speed began at approximately 13 m/s and the cost threshold was  $\Phi_{on} = 0.3$ . The path, cost, speed, and acceleration are presented in Figs. 5.13-5.16. The time when the cost threshold was crossed is indicated by a solid vertical line labeled "Engage" in Figs. 5.14-5.16.

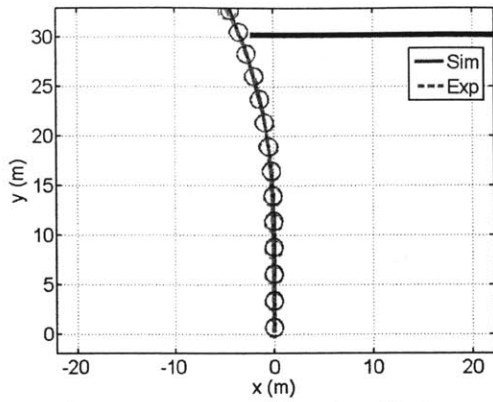


Fig. 5.14: Paths during passing maneuver at 13 m/s with  $\Phi_{on} = 0.3$ . The vehicle is near a corner of the hazard and travels perpendicular to the hazard face. The vehicle path is illustrated by the circles.

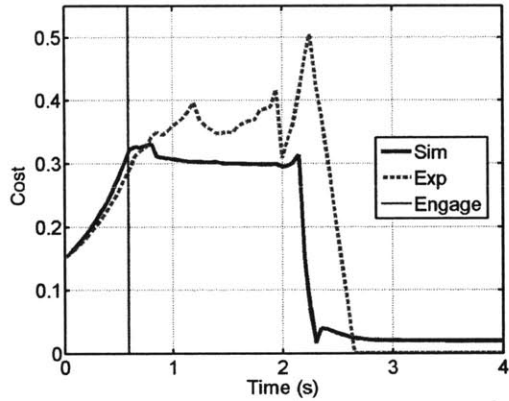


Fig. 5.15: Predicted cost during passing turn at 13 m/s with  $\Phi_{on} = 0.3$ .

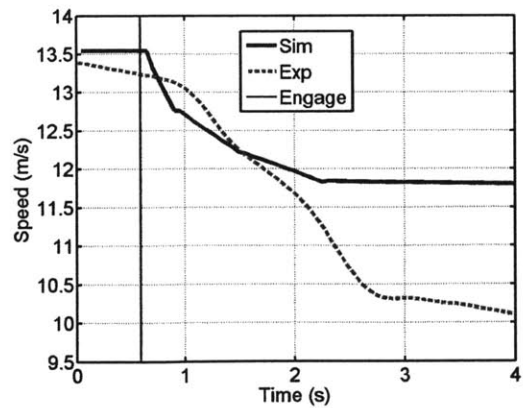


Fig. 5.16: Vehicle speed during passing turn at 13 m/s with  $\Phi_{on} = 0.3$ .

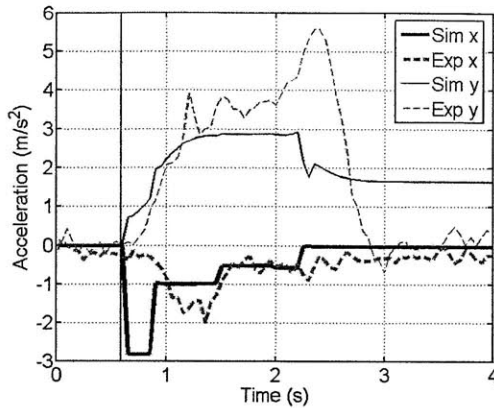


Fig. 5.17: Vehicle acceleration during passing turn at 13 m/s with  $\Phi_{on} = 0.3$ . The longitudinal and lateral directions are denoted by  $x$  and  $y$  respectively.

The initial cost of 0.15 increased to the threshold of  $\Phi_{on} = 0.3$  at approximately 0.59 s. After reaching the threshold, both the simulated and experimental vehicles applied a combination of braking and steering inputs to avoid the hazard. There is a close match between the simulated and experimental vehicle paths shown in Fig. 5.13. The simulated cost reached a peak of 0.33 and remained roughly constant during the maneuver. The experimental cost reached a peak of 0.50. The differences between the simulated and experimental cost are likely to be caused by model parameter mismatch.

### 5.3.4 Non-passing turn

A non-passing maneuver was demonstrated with a single experimental result with controller intervention. This maneuver was tested by defining a very long hazard edge nearly parallel to the vehicle's direction of travel. This scenario corresponds to a lane-keeping task or prevention of road departure. The path and cost of the maneuver are given in Figs. 5.17-5.18. The initial speed of the vehicle was 21 m/s with a threshold of  $\Phi_{on} = 0.3$ . It can be seen that the vehicle successfully avoided the wide hazard.

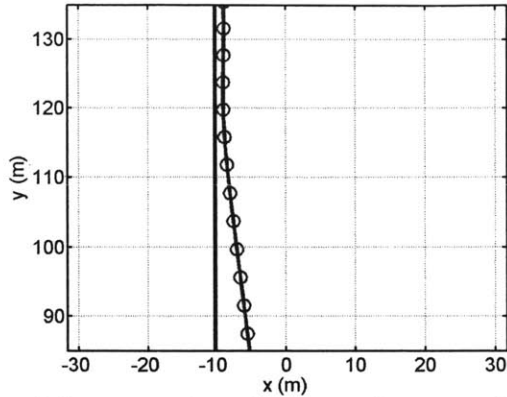


Fig. 5.18: Experimental demonstration of non-passing turn with 1-step prediction and cost-to-go. The critical hazard edge is long and nearly parallel to the vehicle direction of travel. The vehicle path is illustrated by the circles.

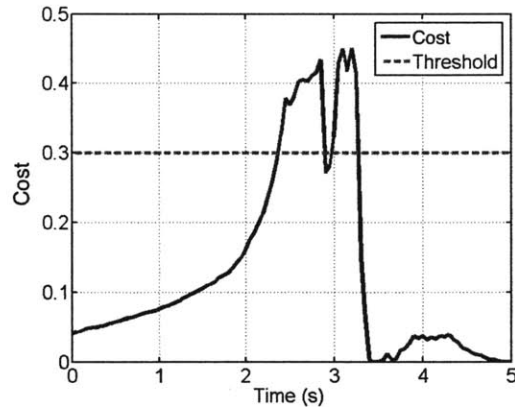


Fig. 5.19: Predicted cost during non-passing turn maneuver initiated by controller intervention.

#### 5.4 Discussion

The semi-autonomous hazard avoidance system was demonstrated experimentally for stopping, passing turn, and non-passing turn maneuvers with and without driver intervention. The use of the short prediction horizon with cost-to-go enabled the nonlinear MPC computation to be completed within 50 ms and the controller to run in real-time. During these tests, there were no instances of computation overrunning the allotted computation time.

The semi-autonomous nature of the system was demonstrated successfully in low-cost situations when the driver took action to avoid the hazard and the system did not

intervene. The intervention behavior of the semi-autonomous system can accommodate varying levels of driver skill by adjusting the threat threshold parameter  $\Phi_{on}$ .

The semi-autonomous nature of the system was also demonstrated successfully in high-cost situations for passing and non-passing turns when the system engaged the steering and braking actuators to successfully avoid the hazard. The vehicle did not stop completely before the hazard face during the stopping test, however. Comparing the simulation results to the experimental results, a significant lag was observed between the commanded and actual braking deceleration. This is likely caused by unmodeled lag in the braking actuator dynamics. It is well known that model mismatch can cause problems for nonlinear model predictive control. Future work with model predictive control for hazard avoidance via braking should consider the effect of braking actuator dynamics on system performance.

## 5.5 Conclusion

A hazard avoidance controller based on a minimum-acceleration model predictive controller was presented and demonstrated in simulations and experiments. An approximation of cost based on computationally efficient analytical calculations of canonical avoidance maneuvers was used as a cost-to-go to reduce computational demand. The system was found to successfully avoid hazards with passing and non-passing turns, though unmodeled lag in braking actuator dynamics caused performance problems in stopping maneuvers. Future work will attempt to address issues of model mismatch.

# 6

## **CHAPTER 6: CONCLUSIONS**

---

### **6.1 Summary**

Hazard avoidance is an important capability for safe operation of robotic vehicles traveling at high speed. There are also applications to driver assistance systems for improving passenger vehicle safety. This thesis presented results related to planning and control of optimal hazard avoidance maneuvers for a bicycle model with wheel slip, given sufficient knowledge of the environment.

The planning problem for optimal hazard avoidance was posed so that dynamic quantities subject to inequality constraints are minimized, while ensuring a minimum clearance from hazards. The constrained quantities to be minimized are chosen based on their impact on feasibility of avoidance, such as the front friction circle constraint for the nonlinear bicycle model. An example optimal avoidance trajectory was computed numerically to illustrate the properties of the optimal avoidance maneuvers generated by this algorithm. The maneuvers tend to avoid the hazard with the minimum required clearance such that the minimized quantities are approximately constant. It was noted that it is computationally demanding to compute these trajectories numerically in real-time.

In an attempt to simplify the computation of optimal avoidance trajectories, analytical solutions to the optimal planning problem were presented for a point mass subject to a constraint on acceleration magnitude. The acceleration magnitude constraint is analogous to a tire friction circle constraint. Pontryagin's minimum principle was applied to two sets of boundary conditions for the point mass, corresponding to optimal passing and non-passing turns. The acceleration of these optimal maneuvers was compared to the acceleration of geometric avoidance maneuvers, namely, straight-line stopping and constant radius passing and non-passing turns. The optimal maneuvers were found to require up to 25% less acceleration than the geometric maneuvers. Conditions were also

found on the position and orientation of hazards relative to the vehicle to show when the optimal passing turn requires less acceleration than the optimal non-passing turn.

The results of the point mass were extended to the nonlinear bicycle with wheel slip by defining a flatness-based trajectory tracking controller using tire force control. This controller decouples the bicycle dynamics into a point mass at the front center of percussion with an additional degree of freedom for yaw dynamics. Structure was identified in the yaw dynamics resembling that of a nonlinear oscillator. This structure was exploited to identify limits on the acceleration of reference trajectories and limits on the longitudinal force applied at the rear wheels for which the yaw dynamics are stable. The controller was simulated to verify the stability properties of the yaw dynamics while tracking reference maneuvers. Noting that the front friction circle constraint can be mapped to a constraint on acceleration magnitude of the front center of oscillation, these results allow the point mass avoidance maneuvers to be applied to the nonlinear bicycle with wheel slip.

These results were applied to a semi-autonomous driver assistance system and demonstrated experimentally. Efficient computation of point mass avoidance maneuvers was used as a cost-to-go to reduce the computational requirements of real-time numerical optimization of avoidance trajectories using model predictive control. The experimental system switched control authority between the driver and an automatic avoidance controller based on the cost of the optimal trajectory. The driver retained control authority in low-cost situations, and the automatic controller was engaged to avoid hazards automatically in high-cost situations.

## 6.2 Future work

There are opportunities for future work related to optimal planning of maneuvers for the point mass with bounded acceleration magnitude. The avoidance scenarios considered in this work involved single stationary hazards. Avoidance maneuvers can be found for multi-hazard scenarios by chaining a sequence of single hazard avoidance maneuvers, provided that the hazards are far enough apart. Optimal maneuvers may also be found for scenarios with closely spaced hazards by applying the optimal control analysis to different sets of boundary conditions. These optimal maneuvers can also be incorporated into other planning methods such as RRT\* [37].

There are also opportunities for future work related to the flatness-based trajectory tracking controller for the bicycle model with wheel slip. The effect of load transfer has been identified by racing professionals as having an impact on vehicle dynamics on surfaces with high friction coefficients. It would be useful to study the effect of load transfer on the trajectory tracking controller and the stability of the yaw dynamics. Additionally, the stability analysis of the yaw dynamics at high slip angles can be used to study the properties of aggressive maneuvers used by professional rally racers, such as trail braking and pendulum turns. The connection with the point mass model may allow efficient planning of these types of aggressive maneuvers.

## **REFERENCES**

---

1. J. Ackermann, "Robust decoupling, ideal steering dynamics and yaw stabilization of 4WS cars," *Automatica*, v. 30, n. 11, pp. 1761-1768, November 1994.
2. "Adaptive Cruise Control and Collision Warning with Brake Support," [http://media.ford.com/images/10031/Adaptive\\_Cruise.pdf](http://media.ford.com/images/10031/Adaptive_Cruise.pdf)
3. A. Alleyne, "Comparison of alternative obstacle avoidance strategies for vehicle control," *Vehicle System Dynamics*, v. 27, n. 5-6, pp. 371-392, June 1997.
4. S. Anderson, S. Peters, T. Pilutti, K. Iagnemma, "An Optimal-Control-Based Framework for Trajectory Planning, Threat Assessment, and Semi-Autonomous Control of Passenger Vehicles in Hazard Avoidance Scenarios," *International Journal of Vehicle Autonomous Systems*, v. 8, n. 2/3/4, pp. 190-216, 2010.
5. S. Antonov, A. Fehn, A. Kugi, "A new flatness-based control of lateral vehicle dynamics," *Vehicle System Dynamics*, v. 46, n. 9, pp. 789-801, 2008.
6. E. Bakker, L. Nyborg, H. B. Pacejka, "Tyre modelling for use in vehicle dynamics studies," *SAE Transactions*, n. 870421, 1987.
7. C.E. Beal, J.C. Gerdes, "A Method for Incorporating Nonlinear Tire Behavior Into Model Predictive Control for Vehicle Stability", *Proc. ASME 2010 Dynamic Systems and Control Conference*, n. DSAC2010-4168, 2010.
8. J.E. Bernard, L. Segel, and R. E. Wild, "Tire Shear Force Generation During Combined Steering and Braking Maneuvers," *SAE Transactions*, 1977, n. 770852, pp. 2953-2969.
9. J. T. Betts, "Survey of numerical methods for trajectory optimization", *Journal of Guidance, Control, and Dynamics*, v. 21, n. 2, pp. 193-207, 1998.
10. M. Blundell, D. Harty, *The Multibody Systems Approach to Vehicle Dynamics*, Elsevier, 2004.
11. C. Brooks, K. Iagnemma, "Visual Detection of Novel Terrain via Two-Class Classification," *Proceedings of the 24th Annual ACM Symposium on Applied Computing 2009*, Honolulu, Hawaii, March 2009.
12. R.G. Brusch, "Bilinear tangent yaw guidance," *Proc. of 1979 AIAA Guidance and Control Conference*, AIAA-1979-1730, pp. 250-264, 1979.
13. A.E. Bryson Jr., Y.C. Ho, *Applied optimal control: optimization, estimation, and control*, Waltham, MA: Blaisdell, 1969.
14. M. Buehler, K. Iagnemma, S. Singh, (eds.), *The 2005 DARPA Grand Challenge: The Great Robot Race*, Springer Tracts in Advanced Robotics (STAR) Series, vol. 36, Springer, Sept., 2007.
15. M. Buehler, K. Iagnemma, S. Singh, (eds.), *The DARPA Urban Challenge: Autonomous Vehicles in City Traffic*, Springer Tracts in Advanced Robotics (STAR) Series, vol. 56, Springer, Dec., 2009.
16. T.A. Burton, "The nonlinear wave equation as a Liénard equation," *Funkcialaj Ekvacioj*, v. 34, pp. 529-545, 1991.
17. C. R. Carlson and J.C. Gerdes, "Optimal rollover prevention with steer by wire and differential braking," *Proceedings of the ASME Dynamic Systems and Control Division - 2003*, pp. 345-354, November 2003.

18. A.J. Eele, A.G. Richards, "Path-Planning with Avoidance Using Nonlinear Branch-and-Bound Optimization," *AIAA Journal of Guidance, Control and Dynamics*, v. 32, n. 2, pp. 384-394, March 2009.
19. G. Engelman, et al., "Threat level identification and quantifying system," U.S. Patent 7,034,668, Apr. 25, 2006.
20. L. Evans, "The dominant role of driver behavior in traffic safety," *American Journal of Public Health*, v. 86, n. 6, pp. 784-786, 1996.
21. P. Falcone, F. Borrelli, J. Asgari, H. E. Tseng, D. Hrovat, "Predictive Active Steering Control for Autonomous Vehicle Systems," *IEEE Trans. Control Systems Technology*, v. 15, n. 3, pp. 566-580, 2007.
22. M. Fliess, J. L. Lévine, P. Martin, P. Rouchon, "Flatness and defect of non-linear systems: introductory theory and examples," *International Journal of Control*, v. 61, n. 6, pp. 1327-1361, 1995.
23. C. Farmer, "Effect of Electronic Stability Control on Automobile Crash Risk," *Traffic Injury Prevention*, v. 5, n. 4, pp. 317-325, 2004.
24. C. M. Farmer, A. K. Lund, "Trends Over Time in the Risk of Driver Death: What If Vehicle Designs Had Not Improved?" *Traffic Injury Prevention*, v. 7, n. 4, pp. 335-342, December 2006.
25. L. Fletcher, S. Teller, E. Olson, D. Moore, Y. Kuwata, J. How, J. Leonard, I. Miller, M. Campbell, D. Huttenlocher, A. Nathan, and F.-R. Kline, "The MIT-Cornell collision and why it happened," *Journal of Field Robotics*, v. 25, n. 10, pp. 775-807, 2008.
26. T. Fraichard, H. Asama, "Inevitable collision states - a step towards safer robots?" *Advanced Robotics*, v. 18, n. 10, pp. 1001-1024, 2004.
27. E. Frazzoli, M. A. Dahleh, E. Feron, "Maneuver-based motion planning for nonlinear systems with symmetries," *IEEE Trans. on Robotics*, v. 21, n. 6, pp. 1077-1091, 2005.
28. S. Fuchshumer, K. Schlacher, T. Rittenschober, "Nonlinear Vehicle Dynamics Control - A Flatness Based Approach," *Proc. of 2005 IEEE Conf. on Decision and Control and 2005 European Control Conference*, pp. 6492-6497, December 2005.
29. P. E. Gill, W. Murray, M. A. Saunders, and M. H. Wright, "User's guide for NPSOL 5.0: a Fortran package for nonlinear programming," Report SOL 86-1, Department of Operations Research, Stanford University, Stanford, CA, 1986.
30. J. Hahn, R. Rajamani, L. Alexander, "GPS-Based Real-Time Identification of Tire-Road Friction Coefficient," *IEEE Transactions on Control Systems Technology*, vol. 10, no. 3, pp. 331-343, May 2002.
31. I. Halatci, C. Brooks, K. Iagnemma, "Visual and Tactile Terrain Classification and Classifier Fusion for Planetary Exploration Rovers," *Robotica*, Vol. 26, No. 6, pp. 767-779, Nov 2008.
32. Y. Hattori, E. Ono, S. Hosoe, "Optimum Vehicle Trajectory Control for Obstacle Avoidance Problem," *IEEE/ASME Trans. on Mechatronics*, v. 11, n. 5, pp. 507-512, Oct. 2006.
33. B. Johansson, M. Gafvert, "Untripped SUV rollover detection and prevention," *Proc. 43rd IEEE Conf. Decision and Control*, 2004, v. 5, pp. 5461-5466, 2004.

34. D.W. Jordan, P. Smith, *Nonlinear ordinary differential equations: an introduction for scientists and engineers*, 4<sup>th</sup> ed., Oxford University Press, Oxford [England], New York, 2007.
35. S. A. Kanarachos, "A new method for computing optimal obstacle avoidance steering manoeuvres of vehicles," *International Journal of Vehicle Autonomous Systems*, v. 7, n. 1/2, pp. 73-95, 2009.
36. Y. Kanayama, Y. Kimura, F. Miyazaki and T. Noguchi, "A stable tracking control method for an autonomous mobile robot," *Proc. 1990 IEEE Intl. Conf. Robotics and Automation*, pp. 384-389, 1990.
37. S. Karaman, E. Frazzoli, "Incremental Sampling-based Algorithms for Optimal Motion Planning," arXiv:1005.0416.
38. O. Khatib, "Real-Time Obstacle Avoidance for Manipulators and Mobile Robots," *The International Journal of Robotics Research*, v. 5, n. 1, pp. 90-98, 1986.
39. S. H. Kim, R. Bhattacharya, "Multi-Layer Approach for Motion Planning in Obstacle Rich Environments," *Proc. AIAA Guidance, Navigation, and Control Conference*, 2007.
40. D.E. Kirk, *Optimal Control Theory - An Introduction*, Prentice Hall, Englewood Cliffs, New Jersey, 1970.
41. K. Kritayakirana, J. C. Gerdes, "Controlling an Autonomous Racing Vehicle: Using Feedforward and Feedback to Control Steering and Speed," *Proc. ASME 2009 Dynamic Systems and Control Conference*, DSAC2009-2572, 2009.
42. K. Kritayakirana, J.C. Gerdes, "Using the Center of Percussion to Generate Feedforward Steering for an Autonomous Race Car", *Proc. of 22<sup>nd</sup> IAVSD Symposium*, 2011, IAVSD, Manchester, United Kingdom.
43. J. C. Latombe, *Robot motion planning*, 1991, Dordrecht: Kluwer Academic, ISBN 0-7923-9129-2.
44. S.M. LaValle, *Planning Algorithms*, Cambridge University Press, 2006, ISBN 0521862051, electronic version <http://planning.cs.uiuc.edu/>.
45. S.M. LaValle, J.J. Kuffner Jr, "Randomized Kinodynamic Planning," *The International Journal of Robotics Research*, v. 20, n. 5, pp. 378-400, 2001.
46. W. Lohmiller, J.J.E. Slotine, "On Contraction Analysis for Non-linear Systems", *Automatica*, v. 34, n. 6, pp. 683-696, 1998.
47. P. Martin, S. Devasia, B. Paden, "A different look at output tracking: control of a VTOL aircraft," *Proc. of 33rd IEEE Conf. on Decision and Control*, v. 3, pp. 2376 -2381, 1994.
48. A. R. McNeill, "Walking and Running", *The Mathematical Gazette*, v. 80, n. 488, pp. 262-266, 1996.
49. W.F. Milliken, D.L. Milliken, *Race car vehicle dynamics*, Warrendale, PA: Society of Automotive Engineers, 1995.
50. R. Murray, M. Rathinam, W. Sluis, "Differential Flatness of Mechanical Control Systems: A Catalog of Prototype Systems," *Proc. ASME Int'l Mechanical Engineering Congress and Exposition*, 1995.
51. National Highway Traffic Safety Administration, *Traffic Safety Facts 2004: A compilation of motor vehicle crash data from the FARS and the GES* (DOT HS

- 809 919), Washington, DC: National Highway Traffic Safety Administration, 2006.
52. A. Ollero, G. Heredia, "Stability analysis of mobile robot path tracking," *Proc. IEEE/RSJ Intl. Conf. on Intelligent Robots and Systems*, v. 3, pp. 461-466, 1995.
  53. E. Ono, S. Hosoe, H.D. Tuan, S. Doi, "Bifurcation in vehicle dynamics and robust front wheel steering control," *IEEE Trans. on Control Systems Technology*, v. 6, n. 3, pp. 412-420, 1998.
  54. H.B. Pacejka, *Tire and Vehicle Dynamics* (2nd ed.), Warrendale, PA: Society of Automotive Engineers, 2006.
  55. H. Peng and M. Tomizuka, "Preview Control for Vehicle Lateral Guidance in Highway Automation," *Journal of Dynamic Systems, Measurement, and Control*, v. 115, pp. 679-686, December 1993.
  56. S.C. Peters and K. Iagnemma, "Mobile robot path tracking of aggressive maneuvers on sloped terrain," *Proc. of 2008 IEEE/RSJ Intl. Conf. on Intelligent Robots and Systems*, 2008.
  57. S. V. Rakovic, F. Blanchini, E. Cruck, M. Morari, "Robust obstacle avoidance for constrained linear discrete time systems: A set-theoretic approach," *Proc. 46th IEEE Conf. on Decision and Control*, 2007, pp. 188-193.
  58. J.H. Reif, "Complexity of the generalized mover's problem", *Proc. of 20th Annual IEEE Symposium on Foundations of Computer Science*, pp. 421–427, San Juan, Puerto Rico, October, 1979.
  59. A. Richards, Y. Kuwata, J. How, "Experimental Demonstrations of Real-Time MILP Control," *Proc. AIAA Guidance, Navigation, and Control Conference and Exhibit*, Aug. 11-14 2003, n. AIAA-2003-5802.
  60. E. Rimon, D.E Koditschek, "Exact robot navigation using artificial potential functions," *IEEE Trans. on Robotics and Automation*, v. 8, n. 5, pp. 501-518, 1992.
  61. E.J. Rossetter, J.C. Gerdes, "Lyapunov Based Performance Guarantees for the Potential Field Lane-keeping Assistance System," *Journal of Dynamic Systems, Measurement, and Control*, v. 128, n. 3, pp. 510-522, 2006.
  62. M. Schorn, U. Stahlin, A. Khanafer, R. Isermann, "Nonlinear trajectory following control for automatic steering of a collision avoiding vehicle," *Proc. of American Control Conference*, June 2006, pp. 5837-5842.
  63. L. Segel, "Theoretical Prediction and Experimental Substantiation of the Response of the Automobile to Steering Control," *Proc. of Automotive Division, Inst. Mech. Engineers*, London, v. 1956, pp. 310-330, 1956-1957.
  64. P. Setlur, J. Wagner, D. Dawson, D. Braganza, "A trajectory tracking steer-by-wire control system for ground vehicles," *IEEE Trans. on Vehicular Technology*, v. 55 n. 1, pp. 76–85, 2006.
  65. Z. Shiller, S. Sundar, "Emergency Lane-Change Maneuvers of Autonomous Vehicles," *Journal of Dynamic Systems, Measurement, and Control*, v. 120, n. 1, pp. 37-44, 1998.
  66. J.J.E. Slotine, W. Li, *Applied Nonlinear Control*, Prentice-Hall, 1991.
  67. M. Spenko, Y. Kuroda, S. Dubowsky, K. Iagnemma, "Hazard Avoidance for High Speed Unmanned Ground Vehicles in Rough Terrain," *Journal of Field Robotics*, v. 23, n. 5, pp. 311-331, May 2006.

68. J.P. Switkes, E.J. Rossetter, I.A. Coe, J.C. Gerdes, "Handwheel Force Feedback for Lanekeeping Assistance: Combined Dynamics and Stability", *Journal of Dynamic Systems, Measurement, and Control*, v. 128, n. 3, pp. 532-542, 2006.
69. O. Takahashi, R. J. Schilling, "Motion planning in a plane using generalized Voronoi diagrams," *IEEE Trans. on Robotics and Automation*, v. 5, n. 2, pp. 143-150, 1989.
70. K.L.R. Talvala, K. Kritayakirana, and J.C. Gerdes, "Pushing the limits: From lanekeeping to autonomous racing", *Annual Reviews in Control*, v. 35, n. 1, pp. 137-148, 2011.
71. S. Thrun, M. Montemerlo, et al., "Stanley: The Robot that Won the DARPA Grand Challenge," *Journal of Field Robotics*, vol. 23, pp. 661-692, August 2006.
72. E. Velenis, E. Frazzoli, P. Tsiotras, "Steady-state cornering equilibria and stabilisation for a vehicle during extreme operating conditions", *International Journal of Vehicle Autonomous Systems*, v. 8, n. 2/3/4, p. 217-241, 2010.
73. E. Velenis, P. Tsiotras, J. Lu, "Modeling Aggressive Maneuvers on Loose Surfaces: The Cases of Trail-Braking and Pendulum-Turn," *Proc. of European Control Conference*, Kos, Greece, July 2-5, 2007.
74. E. Velenis, P. Tsiotras, "Optimal Velocity Profile Generation for Given Acceleration Limits: The Half-Car Model Case," *IEEE International Symposium on Industrial Electronics (ISIE05)*, Dubrovnik, Croatia, June 20-23, 2005.
75. J. Villagra, B. d'Andrea Novel, H. Mounier, M. Pengov, "Flatness-based vehicle steering control strategy with SDRE feedback gains tuned via a sensitivity approach," *IEEE Trans. on Control Systems Technology*, v. 15, n. 3, pp. 554–565, May 2007.
76. C. C. de Wit and O. J. Sordalen, "Exponential stabilization of mobile robots with nonholonomic constraints," *IEEE Trans. Automatic Control*, v. 37, n. 11, pp. 1791-1797, 1992.
77. J. Yi, L. Alvarez, and R. Horowitz, "Adaptive emergency braking control with underestimation of friction coefficient," *IEEE Transactions on Control Systems Technology*, v. 10, n. 3, pp. 381-392, 2002.

# A

## **APPENDIX A: COST-TO-GO FOR NONLINEAR MPC**

This Appendix contains details of the cost-to-go computation for the nonlinear MPC controller used for planning and control in the semi-autonomous vehicle safety system described in Chapter Five. The acceleration of several avoidance trajectories are computed for a point mass located at the front center of percussion of the bicycle model. The cost-to-go is based on the avoidance trajectory with the minimum acceleration. The point mass maneuvers considered are straight-line stopping and constant radius passing and non-passing turns. These maneuvers were considered in Chapter Three, for a point vehicle, and are extended here to a circular vehicle model of radius  $r$ .

### **A.1 Straight-line stopping**

A straight-line stopping maneuver consists of acceleration applied opposite to the vehicle velocity vector, causing the vehicle to stop before reaching the hazard  $P$ , as illustrated in Fig. A.1. The critical edge of  $P$  is specified by nodes  $\mathbf{n}_1$  and  $\mathbf{n}_2$ , tangent unit vector  $\mathbf{e}_1$ , and normal unit vector  $\mathbf{e}_2$ . For this maneuver, the vehicle is approximated as the bounding square surrounding the circle of radius  $r$  centered at point  $[X_{pm}, Y_{pm}]$ . The square is aligned with the velocity unit vector  $\mathbf{e}_4$  with front corner points  $\mathbf{v}_1$  and  $\mathbf{v}_2$ .

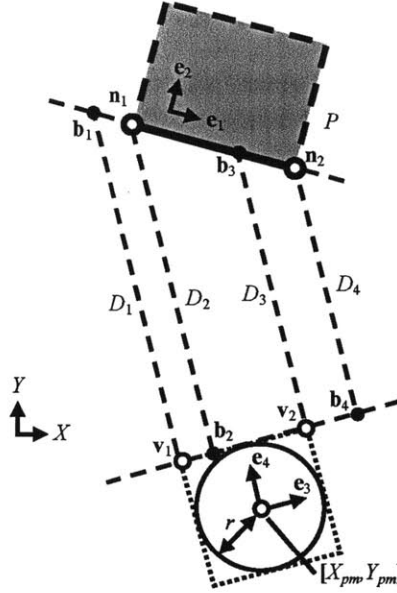


Fig. A.1: Straight-line stopping maneuver. The critical edge of hazard  $P$  is specified by nodes  $\mathbf{n}_1$ ,  $\mathbf{n}_2$ , and the vehicle is approximated by a square oriented with the vehicle velocity vector.

Possible points of collision  $\mathbf{b}_1\text{-}\mathbf{b}_4$  are computed by projecting nodes  $\mathbf{v}_1$ ,  $\mathbf{v}_2$  along the velocity vector onto the hazard edge line and nodes  $\mathbf{n}_1$ ,  $\mathbf{n}_2$  along the velocity vector onto the vehicle edge line. The lines passing through nodes  $\mathbf{n}_1$ ,  $\mathbf{n}_2$  and  $\mathbf{v}_1$ ,  $\mathbf{v}_2$  are given below, where the components of unit vectors  $\mathbf{e}_2$  and  $\mathbf{e}_4$  are  $(e_{2x}, e_{2y})$  and  $(e_{4x}, e_{4y})$  and the coordinates of nodes  $\mathbf{n}_1$  and  $\mathbf{v}_1$  are  $(n_{1x}, n_{1y})$  and  $(v_{1x}, v_{1y})$ .

$$e_{2x}(x - n_{1x}) + e_{2y}(y - n_{1y}) = 0 \quad (209)$$

$$e_{4x}(x - v_{1x}) + e_{4y}(y - v_{1y}) = 0 \quad (210)$$

The projection lines for computing points  $\mathbf{b}_1\text{-}\mathbf{b}_4$  are computed as follows, where  $(x_i, y_i)$  are coordinates of the point to be projected:

$$e_{4y}(x - x_i) - e_{4x}(y - y_i) = 0 \quad (211)$$

The coordinates of a point  $\mathbf{b}_i$  given by  $(b_{ix}, b_{iy})$  are computed by solving linear equations. For example, the coordinates of point  $\mathbf{b}_1$  are computed by solving the following:

$$\begin{bmatrix} e_{2x} & e_{2y} \\ e_{4y} & -e_{4x} \end{bmatrix} \begin{bmatrix} b_{1x} \\ b_{1y} \end{bmatrix} = \begin{bmatrix} e_{2x}n_{1x} + e_{2y}n_{1y} \\ -e_{4x}v_{1y} + e_{4y}v_{1x} \end{bmatrix} \quad (212)$$

Distances  $D_1$ - $D_4$  represent the projected distances of points  $\mathbf{b}_1$ - $\mathbf{b}_4$  and are computed as follows:

$$D_1 = \mathbf{e}_4 \cdot (\mathbf{b}_1 - \mathbf{v}_1) \quad (213)$$

$$D_2 = \mathbf{e}_4 \cdot (\mathbf{n}_1 - \mathbf{b}_2) \quad (214)$$

$$D_3 = \mathbf{e}_4 \cdot (\mathbf{b}_3 - \mathbf{v}_2) \quad (215)$$

$$D_4 = \mathbf{e}_4 \cdot (\mathbf{n}_2 - \mathbf{b}_4) \quad (216)$$

A projected point  $\mathbf{b}_i$  lies outside of its projected line segment, e.g. points  $\mathbf{b}_1$  and  $\mathbf{b}_4$  in Fig. 5, if the following conditions are met:

$$\min\{\mathbf{e}_1 \cdot (\mathbf{b}_i - \mathbf{n}_1) < 0, \mathbf{e}_1 \cdot (\mathbf{n}_2 - \mathbf{b}_i) < 0\} < 0 \quad i \in \{1,3\} \quad (217)$$

$$\min\{\mathbf{e}_3 \cdot (\mathbf{b}_i - \mathbf{v}_1) < 0, \mathbf{e}_3 \cdot (\mathbf{v}_2 - \mathbf{b}_i) < 0\} < 0 \quad i \in \{2,4\} \quad (218)$$

For each projected point  $\mathbf{b}_i$  that lies outside of its projected line segment, the corresponding distance  $D_i$  is set to infinity. The acceleration required by this stopping maneuver is computed as  $a_1$  below, where  $D$  is taken to be the smallest of distances  $D_1$ - $D_4$ . Note that if the vehicle will avoid the obstacle when traveling straight, the stopping distance will be infinity and its stopping acceleration will be zero.

$$a_1 = \frac{\dot{X}_{pm}^2 + \dot{Y}_{pm}^2}{2D} \quad (219)$$

## A.2 Constant radius non-passing turn

A non-passing turn is defined as a constant radius turn in which the vehicle turns to travel parallel to an edge of a hazard  $P$ , as illustrated in Fig. A.2. In contrast, a passing turn is defined as a constant radius turn in which the vehicle turns to pass the critical edge of hazard  $P$  to the left or the right, as described in the subsequent section and illustrated in Fig. A.3. For example, non-passing turns can be used in a lane-keeping task or prevention of road departure.

The critical edge of  $P$  is specified by nodes  $\mathbf{n}_1$  and  $\mathbf{n}_2$ , tangent unit vector  $\mathbf{e}_1$ , and normal unit vector  $\mathbf{e}_2$ . The vehicle is approximated as a circle of radius  $r$  centered at point  $[X_{pm}, Y_{pm}]$  with velocity unit vector  $\mathbf{e}_4$ . The center is projected along unit vector  $\mathbf{e}_3$  to the circumference of the circle to form points  $\mathbf{v}_1$  and  $\mathbf{v}_2$ .

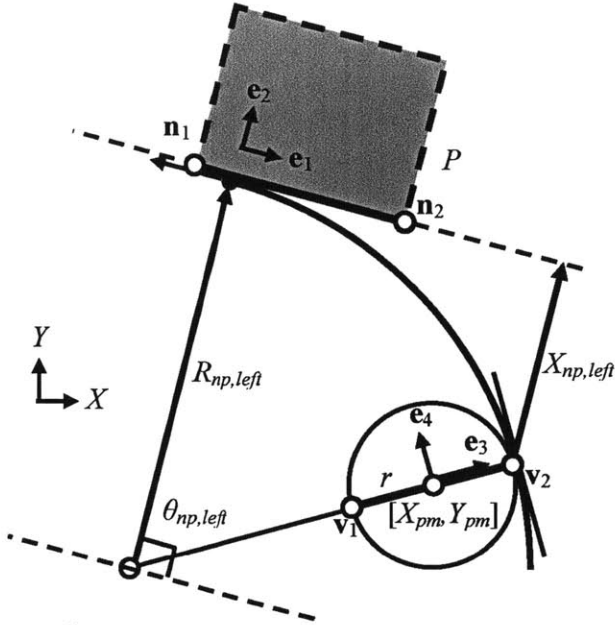


Fig. A.2: Constant radius non-passing turn to the left. The critical edge of hazard  $P$  is specified by nodes  $\mathbf{n}_1$ ,  $\mathbf{n}_2$ , and the vehicle is approximated as a circle of radius  $r$ .

A circle corresponding to a non-passing left turn with radius  $R_{np,left}$  is defined by the following properties:

1. circle passes through point  $\mathbf{v}_2$
2. tangent of circle is parallel to  $\mathbf{e}_4$  at point  $\mathbf{v}_2$
3. circle is tangent to line connecting  $\mathbf{n}_1$  and  $\mathbf{n}_2$
4. center of circle is to left of vehicle

The radius  $R_{np,left}$  is computed as shown below based on intermediate values  $\theta_{np,left}$  and  $X_{np,left}$ .

$$\cos \theta_{np,left} = -\mathbf{e}_1 \cdot \mathbf{e}_4 \quad (220)$$

$$X_{np,left} = (\mathbf{n}_1 - \mathbf{v}_2) \cdot \mathbf{e}_2 \quad (221)$$

$$R_{np,left} = \frac{X_{np,left}}{1 - \cos \theta_{np,left}} \quad (222)$$

A similar circle is found corresponding to a non-passing right turn based on point  $\mathbf{v}_1$  with radius  $R_{np,right}$  and intermediate values  $\theta_{np,right}$  and  $X_{np,right}$ .

$$\cos \theta_{np,right} = \mathbf{e}_1 \cdot \mathbf{e}_4 \quad (223)$$

$$X_{np,right} = (\mathbf{n}_2 - \mathbf{v}_1) \cdot \mathbf{e}_2 \quad (224)$$

$$R_{np,right} = \frac{X_{np,right}}{1 - \cos \theta_{np,right}} \quad (225)$$

The larger of the two radii is termed  $R_{np}$ , and the corresponding turning acceleration  $a_2$  is computed as shown below.

$$a_2 = \frac{\dot{X}_{pm}^2 + \dot{Y}_{pm}^2}{R_{np} - r} \quad (226)$$

### A.3 Constant radius passing turn

A constant radius passing turn consists of acceleration perpendicular to the point mass velocity vector, causing the vehicle to turn and pass one of the nodes of hazard  $P$  as illustrated in Fig. A.3. The critical edge of  $P$  is specified by nodes  $\mathbf{n}_1$  and  $\mathbf{n}_2$ , tangent unit vector  $\mathbf{e}_1$ , and normal unit vector  $\mathbf{e}_2$ . For this maneuver, the vehicle is approximated as a circle of radius  $r$  centered at point  $[X_{pm}, Y_{pm}]$  with velocity unit vector  $\mathbf{e}_4$ . The center is projected along unit vector  $\mathbf{e}_3$  to the circumference of the circle to form points  $\mathbf{v}_1$  and  $\mathbf{v}_2$ .

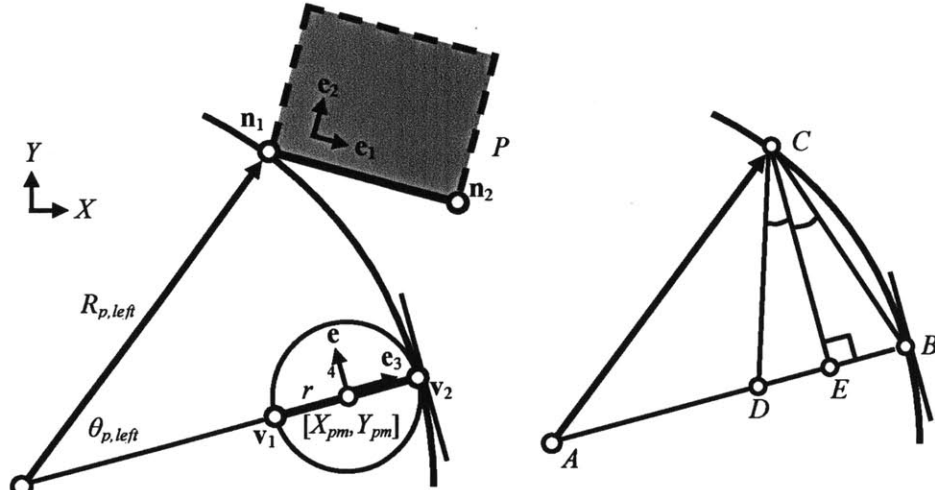


Fig. A.3: Constant radius passing turn to the left. The critical edge of hazard  $P$  is specified by nodes  $\mathbf{n}_1$ ,  $\mathbf{n}_2$ , and the vehicle is approximated as a circle of radius  $r$ . A set of similar triangles are illustrated in the right side of the figure.

A circle corresponding to a left passing turn with radius  $R_{p,left}$  is defined by the following properties:

1. circle passes through point  $\mathbf{v}_2$
2. tangent of circle is parallel to  $\mathbf{e}_4$  at point  $\mathbf{v}_2$

3. circle passes through node  $\mathbf{n}_1$

The turn radius  $R_{p,\text{left}}$  is computed with the aid of the triangles illustrated in the right subfigure of Fig. A.3. Points  $B$  and  $C$  correspond to points  $\mathbf{v}_2$  and  $\mathbf{n}_1$ , respectively. Edge lengths  $\overline{AB}$  and  $\overline{AC}$  are both equal to the radius  $R_{p,\text{left}}$ . Since angles  $\angle ECB$  and  $\angle ECD$  are equal, it can be seen that triangle  $\Delta CDB$  is isosceles. It can further be seen that triangles  $\Delta ABC$  and  $\Delta CDB$  are similar. This similarity implies the following ratio:

$$\frac{\overline{AC}}{\overline{BC}} = \frac{\overline{CB}}{\overline{DB}} \quad (227)$$

Since edge length  $\overline{AC}$  is equal to the unknown radius  $R_{p,\text{left}}$ , this ratio can be used to find an expression for the radius. Intermediate values  $X_{p,\text{left}}$  and  $Y_{p,\text{left}}$  are defined as follows:

$$X_{p,\text{left}} \equiv \overline{CE} = (\mathbf{n}_1 - \mathbf{v}_2) \cdot \mathbf{e}_4 \quad (228)$$

$$Y_{p,\text{left}} \equiv \overline{BE} = (\mathbf{v}_2 - \mathbf{n}_1) \cdot \mathbf{e}_3 \quad (229)$$

Using the following relations, an equation for the radius is found:

$$\overline{DB} = 2\overline{BE} = 2Y_{p,\text{left}} \quad (230)$$

$$\overline{CB} = \sqrt{\overline{BE}^2 + \overline{CE}^2} = \sqrt{X_{p,\text{left}}^2 + Y_{p,\text{left}}^2} \quad (231)$$

$$R_{p,\text{left}} = \frac{\overline{CB}^2}{\overline{DB}} = \frac{X_{p,\text{left}}^2 + Y_{p,\text{left}}^2}{2Y_{p,\text{left}}} \quad (232)$$

The angle  $\theta_{p,\text{left}}$  can be found using the following relations:

$$\angle BCE = \tan^{-1} \frac{Y_{p,\text{left}}}{X_{p,\text{left}}} \quad (233)$$

$$\theta_{p,\text{left}} = \angle CAB = 2\angle BCE \quad (234)$$

A similar circle with radius  $R_{p,\text{right}}$  is found corresponding to a right turn based on points  $\mathbf{v}_1$  and  $\mathbf{n}_2$  using intermediate values  $X_{p,\text{right}}$  and  $Y_{p,\text{right}}$ .

$$X_{p,\text{right}} = (\mathbf{n}_2 - \mathbf{v}_1) \cdot \mathbf{e}_4 \quad (235)$$

$$Y_{p,\text{right}} = (\mathbf{n}_2 - \mathbf{v}_1) \cdot \mathbf{e}_3 \quad (236)$$

$$R_{p,\text{right}} = \frac{X_{p,\text{right}}^2 + Y_{p,\text{right}}^2}{2Y_{p,\text{right}}} \quad (237)$$

$$\theta_{p,right} = 2 \tan^{-1} \frac{Y_{p,right}}{X_{p,right}} \quad (238)$$

The larger of the two radii is termed  $R_p$ , and the corresponding turning acceleration  $a_3$  is computed as shown below.

$$a_3 = \frac{\dot{X}_{pm}^2 + \dot{Y}_{pm}^2}{R_p - r} \quad (239)$$

It should be noted that when starting far from the corner node of a hazard, the circular passing arc may cross the hazard edge in order to intersect the corner node, as shown in Fig. 9. When this occurs, a passing turn in that direction is not feasible. A condition for the feasibility of a passing turn is that the passing turn angle  $\theta_{p,left}, \theta_{p,right}$  is less than the corresponding non-passing turn angle  $\theta_{np,left}, \theta_{np,right}$ . When passing turns are infeasible, an alternative maneuver, such as non-passing turn or stopping maneuver, must be chosen instead.

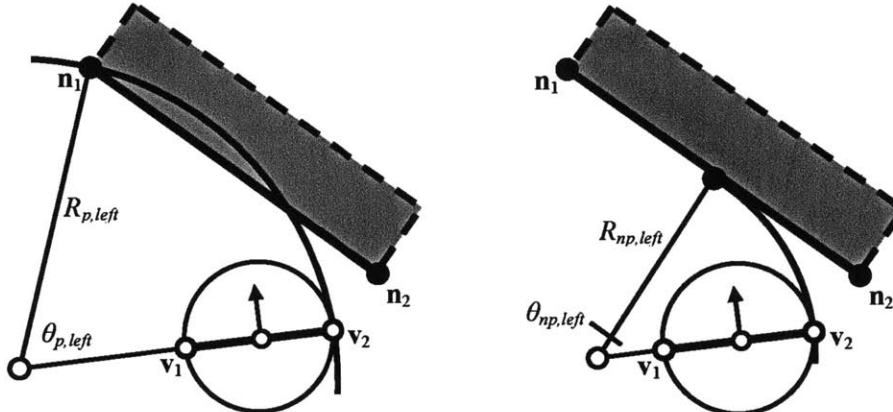


Fig. A.4: Infeasible constant radius passing turn to the left. The vehicle is too far from the corner nodes to pass without a collision. An alternative maneuver must be attempted instead.